

Feature based estimation of myocardial motion from tagged MR images

Citation for published version (APA):

Becciu, A. (2010). *Feature based estimation of myocardial motion from tagged MR images*. [Phd Thesis 1 (Research TU/e / Graduation TU/e), Biomedical Engineering]. Technische Universiteit Eindhoven. <https://doi.org/10.6100/IR692105>

DOI:

[10.6100/IR692105](https://doi.org/10.6100/IR692105)

Document status and date:

Published: 01/01/2010

Document Version:

Publisher's PDF, also known as Version of Record (includes final page, issue and volume numbers)

Please check the document version of this publication:

- A submitted manuscript is the version of the article upon submission and before peer-review. There can be important differences between the submitted version and the official published version of record. People interested in the research are advised to contact the author for the final version of the publication, or visit the DOI to the publisher's website.
- The final author version and the galley proof are versions of the publication after peer review.
- The final published version features the final layout of the paper including the volume, issue and page numbers.

[Link to publication](#)

General rights

Copyright and moral rights for the publications made accessible in the public portal are retained by the authors and/or other copyright owners and it is a condition of accessing publications that users recognise and abide by the legal requirements associated with these rights.

- Users may download and print one copy of any publication from the public portal for the purpose of private study or research.
- You may not further distribute the material or use it for any profit-making activity or commercial gain
- You may freely distribute the URL identifying the publication in the public portal.

If the publication is distributed under the terms of Article 25fa of the Dutch Copyright Act, indicated by the "Taverne" license above, please follow below link for the End User Agreement:

www.tue.nl/taverne

Take down policy

If you believe that this document breaches copyright please contact us at:

openaccess@tue.nl

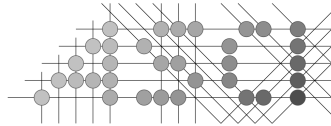
providing details and we will investigate your claim.

Feature based estimation of myocardial motion from
tagged MR images

Colophon

The cover is designed by Douwe Hoendervanger. The front page represents a velocity field of the short axis visualization of the cardiac walls. The back cover shows an image sequence of the heart of the author of this dissertation.

This thesis was typeset by the author using $\text{\LaTeX}2_{\epsilon}$.



Advanced School for Computing and Imaging

This work was carried out in the ASCI graduate school. ASCI dissertation series number 212.



This research was financially supported by the Dutch Technology Foundation STW (project number: ENN.6760).

Financial support for the publication of this thesis was kindly provided by the Advanced School for Computing and Imaging (ASCI), the Stichting voor de Technische Wetenschappen (STW), and the Technische Universiteit Eindhoven.

Printed by Printservice TU/e, Eindhoven, the Netherlands.

A catalogue record is available from the Eindhoven University of Technology Library.

ISBN: 978-90-386-2377-1

© 2010 A. Becciu, Eindhoven, the Netherlands, unless stated otherwise on chapter front pages, all rights are reserved. No part of this publication may be reproduced or transmitted in any form or by any means, electronic or mechanical, including photocopying, recording, or any information storage and retrieval system, without permission in writing from the copyright owner.

Feature based estimation of myocardial motion from tagged MR images

PROEFSCHRIFT

ter verkrijging van de graad van doctor aan de
Technische Universiteit Eindhoven, op gezag van de
rector magnificus, prof.dr.ir. C.J. van Duijn, voor een
commissie aangewezen door het College voor
Promoties in het openbaar te verdedigen
op woensdag 24 november 2010 om 16.00 uur

door

Alessandro Becciu

geboren te Cagliari, Italië

Dit proefschrift is goedgekeurd door de promotor:

prof.dr.ir. B.M. ter Haar Romeny

Copromotor:

dr.ir. H.C. van Assen

Contents

Colophon	ii
Contents	v
1 Introduction	1
1.1 Motivation and goals	2
1.2 The heart anatomy	5
1.3 Cardiac diseases	6
1.4 Cardiac Imaging: Acquisition techniques	7
1.4.1 Computed tomography (CT)	8
1.4.2 Positron Emission Tomography (PET)	8
1.4.3 Single Photon Emission Computed Tomography (SPECT)	9
1.4.4 Echocardiography	9
1.4.5 Magnetic resonance Imaging (MRI)	10
1.5 Methods for cardiac motion estimation: an overview	11
1.5.1 Tag tracking	13
1.5.2 Phase Contrast Methods	14
1.5.3 Optic Flow methods	14
1.5.3.1 Differential Techniques	15
1.5.3.2 Region Based Matching Techniques	20
1.5.3.3 Frequency Based Techniques	20
1.6 Thesis Outline	21
2 Extraction of cardiac motion using scale-space feature points and gauged reconstruction	23
2.1 Introduction	24
2.2 Image data-set and preprocessing approach	25
2.3 Extraction of scale-space critical points	26
2.4 Sparse feature point velocity estimation	28
2.5 Reconstruction of the dense velocity field	29
2.6 Evaluation	31
2.7 Conclusion	33
3 Feature based cardiac motion estimation using covariant derivatives and Helmholtz decomposition	35
3.1 Introduction	36
3.2 Image data set and preprocessing	39
3.3 Extraction of critical points in scale space	40
3.3.1 Critical point position refinement	41
3.4 Calculation of sparse velocity features	42
3.4.1 Scale selection for features at fixed time frames	43
3.5 Vector field decomposition	45

3.5.1	Multi-scale Helmholtz decomposition of the optical flow field	48
3.5.2	Experiments on the decomposition of the vector field . . .	50
3.6	A motivation for using covariant derivatives.	51
3.6.1	Fibred Space and Covariant Derivatives	54
3.6.1.1	Fibred Space	54
3.6.1.2	Covariant Derivatives	54
3.6.1.3	Interpolation between conventional derivatives and covariant derivatives	57
3.7	Feature based optic flow equation with covariant derivatives and Helmholtz decomposition	58
3.8	Experiments	60
3.9	Discussion and Conclusion	64
4	Cardiac motion estimation: analysis of the kinetic Energy	67
4.1	Introduction	68
4.2	Dense Motion Field and Kinetic Energy	69
4.3	Bull's eye plot	71
4.4	Experiments	72
4.5	Discussion	74
5	Motion extraction: further experiments	83
5.1	Introduction	84
5.2	Phantom	84
5.3	Experiment 1: performance of optic flow techniques	86
5.3.1	Results	87
5.4	Experiment 2: cardiac motion estimation from tagged MR images	87
5.5	Discussion and Conclusion	89
5.6	Acknowledgements	91
6	3D winding number: theory and application to medical imaging	93
6.1	Introduction	94
6.2	Theory	95
6.2.1	Preliminaries	95
6.2.2	Winding number in three dimensions	96
6.2.3	Implementation	98
6.2.4	Refinement of critical point positions	99
6.2.5	Classification of critical points	100
6.3	Experiments	101
6.3.1	Follicle detection	102
6.3.2	Neuronal cell counting in cerebellum	104
6.3.3	3D cardiac motion estimation	105
6.3.3.1	Cardiac image data set	106

6.3.3.2	Calculation of velocity at critical points position and application to cardiac MRI sequence	107
6.4	Discussion and Conclusion	109
6.5	Acknowledgements	111
7	A multi-scale feature based optic flow method for 3D cardiac motion estimation	113
7.1	Introduction	114
7.2	Materials	116
7.2.1	Image Structure	116
7.2.2	Dataset	116
7.3	Method	117
7.3.1	Scale Space	117
7.3.2	Critical point detection	119
7.3.3	Sparse Velocities of Feature Points and Dense Flow Field	119
7.3.4	Angular Error	120
7.4	Results	120
7.5	Discussion	122
8	Conclusions and future research	125
8.1	Summary	126
8.2	Remarks and future research	128
A	Appendix to Chapter 3	131
A.1	Covariant derivatives	132
A.1.1	A Tool from Differential Geometry: Connections on the Vector Bundle E	132
A.1.2	Covariant derivatives on the Vector Bundle E induced by gauge fields.	133
A.2	The Euler-Lagrange equations for Tikhonov regularized optic flow reconstruction in covariant derivatives	136
A.2.1	Algorithm: Solving the Euler-Lagrange Equations by Ex- pansion in B-splines	138
	Bibliography	143
	Acknowledgements	159
	Curriculum Vitae	161
	Publications	163

*Your vision will become clear only when you
look into your heart. Who looks outside, dreams.
Who looks inside, awakens.*

Carl Gustav Jung, psychiatrist

1

Introduction

1.1 Motivation and goals

Recent statistics [6] point out that in 2006 over 80000000 of people were affected by one or more types of cardiovascular disease (CVD) in the United States only, causing over 800000 of deaths (34.3% of all deaths for that year). Figure 1.1 illustrates the percentage breakdown of deaths due to cardiopathy. However, the statistics also show that the mortality related to heart illness has diminished with the years (see Figure 1.2). A possible explanation is related to the continuous warnings for a healthy life style and to the improvements of techniques like cardiac imaging, which covers a major role in the early diagnosis of the disease.

One of the major challenges in medical imaging is the automatic estimation of cardiac motion. Assessment of the heart movement and deformation is of crucial importance, since quantitative evaluation of the parameters (i.e. kinetic energy, strain, stress) may reveal information about the health condition of the myocardium [158]. In presence of a disease it would be interesting to measure, for instance, the location and the extent of the affected regions, since this may help physicians to formulate therapy treatments.

Another application would be the quantification of the response of the heart muscle after a therapy treatment, for example after the implantation of stem cells in the diseased cardiac tissue [25, 44, 159]. These cells are found inside different types of tissue and able to differentiate into specialized cell types. These therapies employ stem cells in the replacements during cardiac surgery instead of foreign material, which may provide infection, loss of functional and biological properties.

Over the years we have seen an increase of techniques used to visualize cardiac illness. Coronary angiography, radionuclide imaging and echocardiography have been largely employed to visualize and estimate coronary artery diseases. Echocardiography has been also applied for cardiac motion estimation by tracking myocardial irregularities that appear as speckles [45, 18, 96, 104, 9]. This modality however presents limited spatial resolution and suboptimal image quality. MRI has already a significant history in medical imaging (first MR image appeared in 1973 [102]), but for a long period it has been considered an additional technique used when data provided by other modalities were incomplete or needed confirmation. However, due to the fact that MRI is noninvasive, fast, highly versatile and due to recent strong technical improvements, such as an increase of spatial and temporal resolution, improvement of signal to noise ratio and elimination of motion artifacts, MRI imaging is playing a primary role especially in areas like congenital heart disease, aortic diseases and ventricular function [144, 132]. For these reasons MR images have been chosen in our experiments.

Percentage breakdown of deaths from cardiovascular diseases in United States in 2006

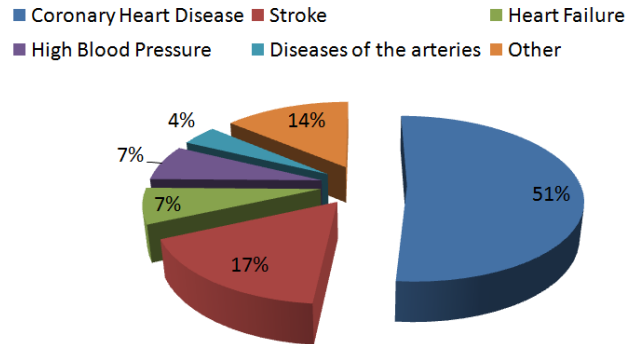


Figure 1.1: Percentage death due to cardiovascular diseases in the United States in 2006. Image adapted from [6].

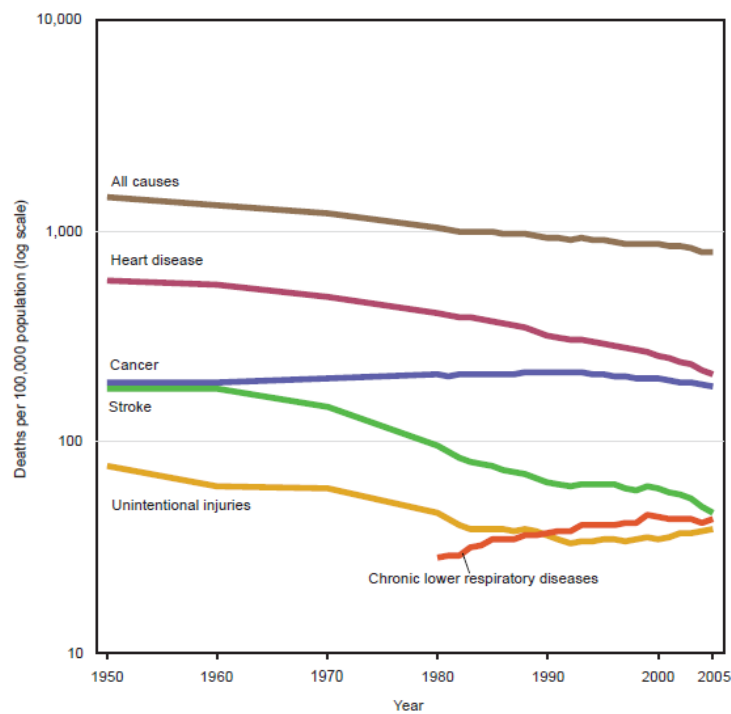


Figure 1.2: Leading cause of death for all ages from 1959 to 2005 in the United States. The estimations are age-adjusted. Image acquired from [61].

In order to highlight heart movement, in the literature we find methods that manipulate MR images imposing artificial patterns (tags) that move along with the cardiac tissue such as (Complementary) SPAtial Modulation of Magnetiza-

tion (SPAMM) [179, 14, 53] or HARmonic Phase (HARP) images [126, 139]. Therefore, several methodologies carry out cardiac motion extraction by estimating the movement of these patterns. Such techniques are mainly based on stripe following and HARP tracking [8, 177, 126, 127], which employ material mesh models and optic flow approaches [68, 147, 163, 59, 21, 22]. It's interesting to mention also a new technique for cardiac motion extraction named SINne wave MODeling (SinMod) [11]. Velocity estimation is based on pixelwise detection of local phase shift and spatial frequency in a bandpass-filtered image.

According to the general computer vision literature, the best performing motion estimation methods are based on differential optic flow approaches [27, 28, 181]. Therefore also in this thesis a differential optic flow technique has been investigated. Most of the differential optic flow techniques are based on the so-called optic flow constraint equation (OFCE) [76]. This equation assumes constancy of the brightness in the image sequence. In tagged MR images, this assumption cannot hold, since tags fade with relaxation time $T1$. In [68] an optic flow methodology was proposed where tag fading was modeled using Bloch equations. This model however requires specific knowledge of $T1$ of the target sequence and such knowledge is not always available. In [163, 59] a multi-scale OFCE was applied directly on HARP images, where the constancy assumption in the brightness was preserved. However the procedure of generating HARP images may remove motion information that compromise the final evaluation. Another issue related to OFCE is the aperture problem, that is, the single equation, having two unknowns, can not be solved uniquely.

In this thesis we try to overcome these problems. We propose a novel variational optic flow methodology based on multi-scale feature points to extract cardiac motion from tagged MR images. For such an approach, feature points used like maxima, minima or saddles do not suffer from fading, since they retain their characteristic even in the presence of brightness changes. Another advantage is that the proposed technique does not suffer from the aperture problem. The method takes also the advantages from the multi-scale framework.

A smoothness term of the proposed optic flow is defined as the sum of contracting/relaxing (rotation-free) and rotating (divergence-free components) contributions, since we noticed that the heart motion can also be described in terms of contractions and rotations. Moreover, the proposed smoothness term takes into account previous knowledge of the vector field. Experiments on phantoms and comparison with similar methodologies that do not take into account prior knowledge of the vector field or vector field decomposition, highlight that the proposed method performs best.

The evaluation of the kinetic energy parameter in a number of volunteers and in a patient with acute myocardial infarction is also addressed in this thesis. In the literature evaluation of total cardiac kinetic energy using a Horn and Schunck

optic flow method [76] has been already investigated by [70, 42]. In this thesis we estimate moreover the kinetic energy of the rotation-free and divergence-free components of the motion field and this provides crucial information of the heart behavior, since it allows to quantify the contribution of the single components to the heart beat. We also evaluate the local kinetic energy and visualize it by means of bull's eye plots [34] and experiments on the patient suggest that regions with a local kinetic energy minimum can be associated to infarcted areas.

In order to evaluate critical points (maxima, minima and saddles), used as feature points for motion extraction, of scalar images in arbitrary number of dimensions, a reformulation of the winding number - a topological number - will be proposed. The case of 3-dimensional images will be extensively discussed and other applications, such as neuron counting in cerebellum images, ovarian follicle counting and tag crossings detection in tagged cardiac MR images, will be investigated.

Finally, a 3-dimensional approach for cardiac motion estimation is proposed. The benefits of the technique, such as the retrieval of the through-plane component of the velocity field, essential for a more reliable motion estimation of the cardiac muscle.

In this chapter, sections 1.2 and 1.3 illustrate the cardiac anatomy and major cardiac diseases. In section 1.4 and 1.5 the most used cardiac imaging modalities and cardiac motion estimation techniques are discussed. The chapter concludes with a paragraph 1.6 where we provide the outline of this thesis.

1.2 The heart anatomy

The heart is a fundamental organ of the human body, big as a fist and located between diaphragm and lungs. It is the most important part of the circulatory system and carries out the function of a pump. To perform this task, the heart is a rhythmically contracting hollow muscle consisting of two pairs of independently contracting chambers. The top consists of the two chambers, called atria, which receive oxygen-depleted blood from the body (right atrium) and oxygenated blood from the lungs (left atrium) and pass it to the larger ventricles. The Left and the Right Ventricle (LV and RV), pump blood into the aorta and the pulmonary artery respectively. The left ventricle pumps the oxygen-enriched blood to the rest of the body to provide all organs and tissue with the necessary energy for life. (Figure 1.3). The left atrium and ventricle are connected by the Mitral Valve, while the right atrium and ventricle are connected by the Tricuspid Valve. The ventricular cycle is divided in two main phases: diastole and systole. Diastole is the expansion (volume increase and

blood filling) of the ventricle while systole is the contraction (volume reduction and blood ejection). During diastole the mitral and tricuspid valve is open and blood flows from the atria into the ventricles. During systole the valve is closed, and blood is pushed through the Aortic Valve (AV) and Pulmonary Valve (PV) into the aorta (systemic circulation) or the pulmonary artery (pulmonary circulation) respectively. A good closure of the valves prevents blood leakage (regurgitation due to valve insufficiency) and backward flow.

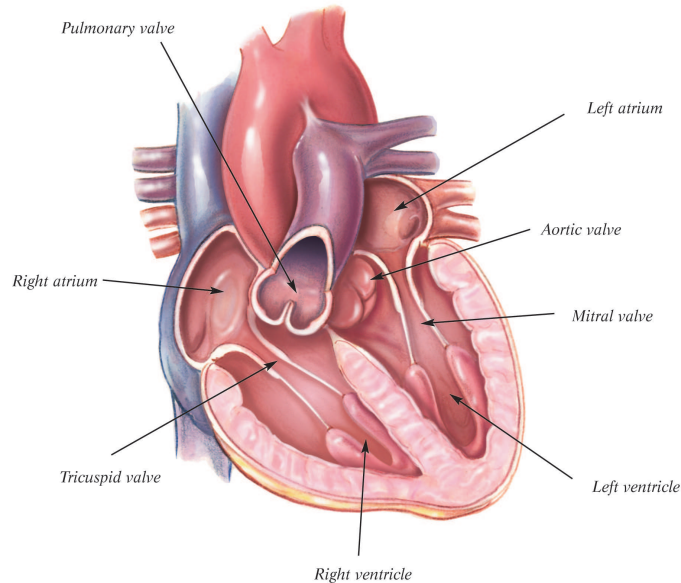


Figure 1.3: Anatomy of the heart muscle. Image used with permission of the Edwards Lifesciences Corporation, Irvine, California [48].

1.3 Cardiac diseases

As already mentioned, cardiac disease is one of the major causes of death in the world [136, 6, 4, 7]. In this section we provide an overview of the main forms of cardiopathy.

Atherosclerosis. Atherosclerosis is a condition caused by depositing of plaques in the arteries. Such plaques consist of fatty material such as cholesterol or other substances such as calcium, which accumulate in the vessel walls provoking a decrease of the vessel's diameter (stenosis). If the plaque is vulnerable, i.e. the cap on lipid pool is thin, the cap may rupture, and leaking lipid (cholesterol) may generate a blood clot. This may occlude vessels further upstream and lead to myocardial infarction

Valvular failure. In this case cardiac valves do not close/open normally causing blood regurgitation or limiting the blood flow. Valvular failure is due to valvular displacement, inflammation of the cardiac valves and valvular stenosis.

Congenital heart disease. Congenital cardiac diseases are the result of defects in the heart structure or vessels in the newborn. One of the most common cardiac congenital defects is hypoplasia, where either the left or the right ventricle does not develop properly. Other defects are related to the abnormal narrowing of vessels or valves, or presence of holes in the septum, the wall tissue that separates the right from the left part of the heart. The abnormal development of vessels such as in the persistent truncus arteriosus is a defect of main concern. In this case the truncus arteriosus never properly divides into pulmonary artery and aorta.

Arrythmia. Arrythmia is an irregular heart beat, causing the heart to pump blood less effectively. The blood is pushed in the four chambers of the heart through a sequence of controlled muscular contractions. Disturbances on the sequence, that is skipping a heart beat or adding an extra beat, generate heart arrythmia. Symptoms are fatigue, fainting, short of breath, chest pains, dizziness.

Hypertension. Such diseases are due to the high blood pressure in the arteries. Chronical conditions of the disease may lead to stroke, heart failure, and arterial aneurysm.

Hypertrophy. Cardiac hypertrophy is an increase of thickness in the myocardium, which results in decrease in size of the chamber of the heart. Hypertension and heart valve stenosis, abnormal narrowing of the valve orifice, are common causes of hypertrophy.

Heart Failure. Heart failure is a progressive disorder defined as inability of the cardiac muscle to provide sufficient blood flow to meet the body's needs. Common causes of heart failure are due to myocardial infarction, (interruption of blood supply to part of the heart, causing heart cells to die), hypertension and valvular heart diseases.

1.4 Cardiac Imaging: Acquisition techniques

Cardiac imaging represents a major area of research in the medical imaging community, since it allows to visualize and investigate the complex behavior of the cardiac muscle. In the following sections the major imaging modalities used in clinical practice will be discussed.

1.4.1 Computed tomography (CT)

Computed tomography is a medical imaging method based on X-ray techniques [65]. Such technique exposes the body of a subject to a high energy ionizing radiation (typically 140 KeV) and the different absorption of radiation in different tissues generates different shadows in the image. Tissues with high atomic weight such as the bones absorb and block the radiation and therefore may appear opaque. Tissues with less atomic weight such as the lungs are instead darker on the image. The pixels are described in terms of radiodensity, the property of relative transparency to the passage of X-rays through a material. The radiodensity is defined in Hounsfield units (HU), and for a certain material X , HU is

$$HU = \frac{\mu_X - \mu_{water}}{\mu_{water} - \mu_{air}} 1000$$

where μ is the linear attenuation coefficient, which describes how easily a material can be penetrated by a beam of light, sound and particles. Bones present $HU = 400$ or more, the water has $HU = 0$, whereas for the air $HU = -1000$. The heart exhibits HU around 0, therefore the CT images of the heart do not present shadows.

In CT scanners software techniques, like multiplanar reconstruction or 3D rendering, build image volumes by "stacking" the slices acquired at different depths one on top of the other. Advantages of using such methodology are the fast image acquisition time, high spatial resolution and nearly isotropic voxel size. Current generation of CT scanners generate images with spatial resolution of $0.4 \times 0.4 \times 0.4 \text{ mm}^3$ and temporal resolution of 80 – 160 ms [37].

1.4.2 Positron Emission Tomography (PET)

PET is a nuclear medicine imaging modality that produces 3-dimensional visualizations of tissue in the body. The methodology employs radionuclides, atoms with nuclei characterized by an excess of energy available to be emitted. The radionuclides, tracers, are incorporated in molecules used by the body such as glucose or in drugs and administered to the patient. After a certain waiting period such molecules concentrate in the region of interest. At this point the patient is placed in the imaging scanner. Radionuclides decay producing positrons, particles with same mass but opposite electric charge with respect to the electron. Positrons interact with nearby electrons producing photons (with 511 KeV each) in opposite directions. Emissions of photons coinciding in time are detected by PET scanners, increasing the radiation information of the region of interest and therefore increasing the resolution (Figure 1.4, row 1, column 2). PET scanners allow to carry out functional measurements: perfusion, oxygenation, protein concentration). However, these methods imply the use of

nuclear radiations and present low spatial resolution [12]. PET images present spatial resolution of $4 - 6 \text{ mm}^3$ and temporal resolution of 1 second [43].

1.4.3 Single Photon Emission Computed Tomography (SPECT)

SPECT is similar to PET, as radioactive tracers and detection of gamma rays are employed. The main difference between the 2 techniques is that SPECT emits gamma photons measured directly, whereas PET emits positrons that, interacting with electrons up to few millimeters away, produce photons emitted in opposite directions. An advantage of the SPECT imaging acquisition methodology is the cost of the complete scanner, much lower than PET scanners. Also such methodology allows performing functional measurements due to molecular concentration around a region of interest. Such a technique, however, implies the use of a nuclear tracer and presents worse spatial and temporal resolution with respect to the PET image acquisition modality (Figure 1.4, row 1, column 3) [12]. Typically images present spatial resolution $1 \times 1 \text{ cm}^2$ and temporal resolution of $4 \times 10^{-2} \text{ s}$.

1.4.4 Echocardiography

Echocardiography is the imaging modality based on ultrasound techniques. In ultrasound scanners a sound wave with frequencies between 2.5 and 5 MHz (the audible range of sound is 20 Hz-20 KHz) is produced by a piezoelectric transducer. The sound is partially reflected in regions where changes in sound velocity in the body occur, such as at blood cell borders or small structures in organs. Parts of the reflected sounds may return to the transducer and are converted into electric signals. These signals are later processed by the ultrasonic scanner and converted into images. Such signals provide information about the position associated to the investigated object. The time delay of the sound to come back to the transducers provides information about the position of the object, namely the more time it needs, the deeper the object is in the body. The amplitude of the reflected signal determines instead the pixel's brightness: the stronger is the signal, the brighter will be the pixel. An example echocardiogram is presented in Figure 1.4, row 2, column 1. Ultrasound modalities are widely applied, since they are relatively inexpensive and portable. Other advantages are the fast acquisition time and high temporal resolution. On the other side such methodologies exert limited spatial resolution and suboptimal image quality [12]. Typically echocardiographic images presents spatial resolution $0.6 \times 0.6 \times 0.6 \text{ mm}^3$ and temporal resolution of $15 - 60 \text{ ms}$ [37].

1.4.5 Magnetic resonance Imaging (MRI)

Magnetic resonance imaging is a noninvasive imaging modality that, due to interaction between radio frequency pulses (short electromagnetic signals used to alter the direction of the magnetic field) with a strong magnetic field and body tissue, provides high quality images of organs inside the body. During the MRI the image acquisition procedure, the body is introduced into a scanner with a high magnetic field, usually 1.5 Tesla in clinical practice (earth's magnetic field strength is only about $5 \cdot 10^{-5}$ Tesla). The body consists mainly of water molecules and each molecule presents two hydrogen nuclei or protons. Under application of a strong magnetic field the magnetic moments of protons align with the direction of the field. The magnetization can be perturbed by imposing a different magnetic field, causing the magnetic moments of protons to alter their alignment relative to the original field and bringing the protons to a higher energy level. Once the new magnetic field is turned off, protons return to their alignment at the original magnetization with a certain relaxation time (so-called T1 and T2). The change in alignment provides a signal detected by the scanner. Different types of tissue (e.g. muscle, fat) present different relaxation times and this is reflected as source of contrast in MR images.

In clinical routine practice cardiac MRI images are acquired in short axis view (SA) and long axis view (LA). SA images are registered at planes perpendicular with respect to the left ventricle axis. The registration is performed at multiple slices from apex to base. Acquisition in the LA modality is instead carried out at planes parallel to the LV axis. See Figure 1.4, row 2, column 2.

A useful way to investigate cardiac mechanical function is through MR Tagging. Tagging is a method for noninvasive assessment of myocardial motion. An artificial brightness pattern, represented as dark stripes, is superimposed on images by spatially modulating magnetization with the aim to improve the visualization of intramyocardial motion [179, 14, 53] (Figure 1.4, row 2, column 3).

MRI image acquisition presents several advantages. The method is noninvasive, presents high spatial resolution, high temporal resolution, intrinsically high blood-myocardium contrast and arbitrary image orientation. On the other side patients are exposed to prolonged examination times. Many MRI acquisitions require breath holding, which may be difficult for patients with a heart condition. Moreover persons with metallic implants may be excluded from MR imaging. Finally, MR images present low through-plane resolution and reproducibility of quantitative results depends on the accuracy of the positioning of the image slices [40, 12]. The MR images used in this thesis present spatial resolution of $1.2 \times 1.2 \text{ mm}^2$ and temporal resolution of $2 \times 10^{-2} - 3 \times 10^{-2} \text{ ms}$.

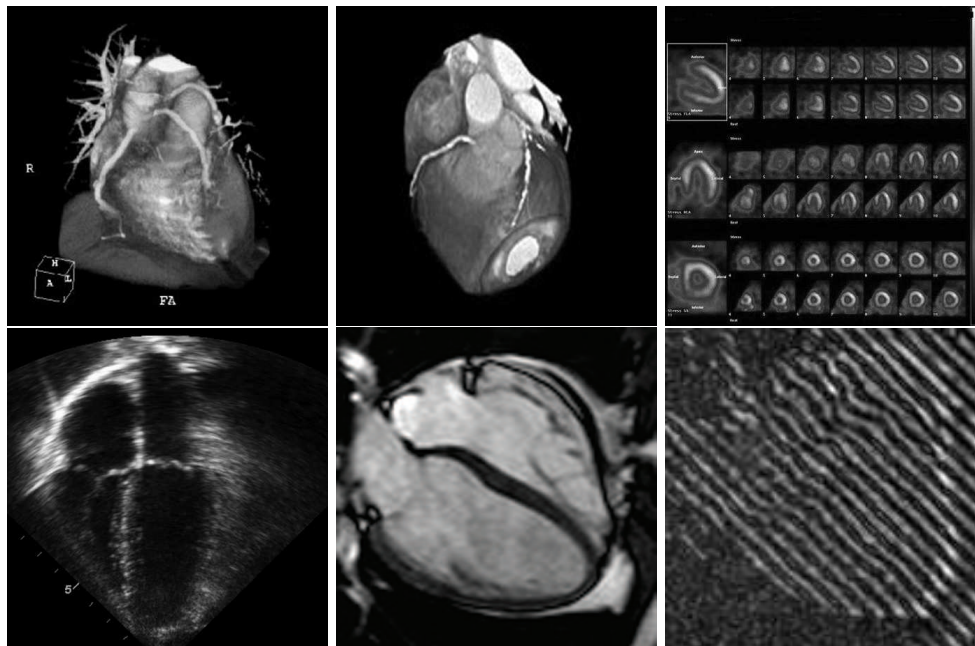


Figure 1.4: Image acquisition modalities. Row 1 column 1. Volume rendered CT angiography of coronary arteries [80]. Row 1, column 2: 3-dimensional PET/CT image [30]. Row 1, column 3. SPECT images [29]. Row 2, column 1: 2-dimensional echocardiogram [31]. Row 2, column 2 and 3: Long axis view of MR and Tagged MR image samples. Courtesy of LUMC, Leiden, Netherlands.

1.5 Methods for cardiac motion estimation: an overview

In everyday world many objects move. Animals distinguish themselves from plants, since they show voluntary movement and use it to communicate, to eat or to avoid to be eaten. Even when the objects around us are stationary, their images on the retina move, since the eyes and head are never entirely still (Figure 1.5). The motion perception represents a fundamental function of the visual system. The brain perceives motion as the result of sequential displacements of static objects in different spatial positions. At the beginning of the nineties Goodale and Milner [67], and previously Ungerleider and Mishkin [157], recognized the so-called *dorsal pathway* (Figure 1.6, left image) as the area of the brain, where the spatial awareness and guidance of actions take place. These conclusions followed the response of lesion studies carried out on the visual cortex of monkeys, which underlined that posterior parietal lesions interfered with the neural mechanism related to spatial perception.

In biological cybernetics, motion perception is expressed through models such as the Reichardt detector [134]. The model, inspired by the visual system of the fly, assumes that correlation of the input signals coming from two separate

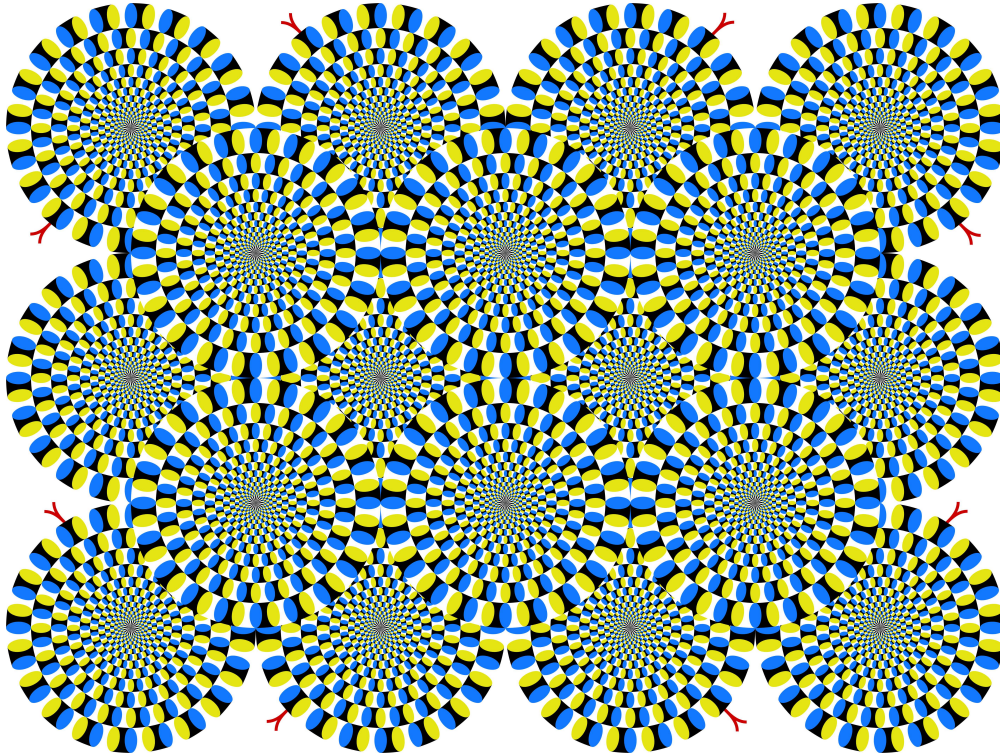


Figure 1.5: Rotating snakes: Optical illusion on motion perception. Permission of image usage given by Prof. Akiyoshi Kitaoka of the Ritsumeikan University, Kyoto, Japan [118].

receptive fields and going to the same ganglion cell may provoke a subsequent action potential. Figure 1.6, right image, provides a scheme of the model. We assume that an object, in this case a circle, moves from position "A" to position "B". In response to light, neuron "A" sends a signal through a device "D" that delays the stimulus to the ganglion cell "G". Neuron "B" sends a signal directly down its axon and it synapses with the ganglion cell "G". The ganglion cell fires in proportion to the amount of the input it receives over the short period of time. Therefore, in case the input signals arrive simultaneously the neuron will produce the maximum response, in case the input signals are not simultaneous, the neuron will provide a weaker response or nothing.

Motion estimation is also a large area of research in medical imaging, since it may underline abnormalities in organs where complex motion is involved. In the following sections we describe the most common techniques used in cardiac motion extraction, providing also an extensive overview of optic flow methodologies.

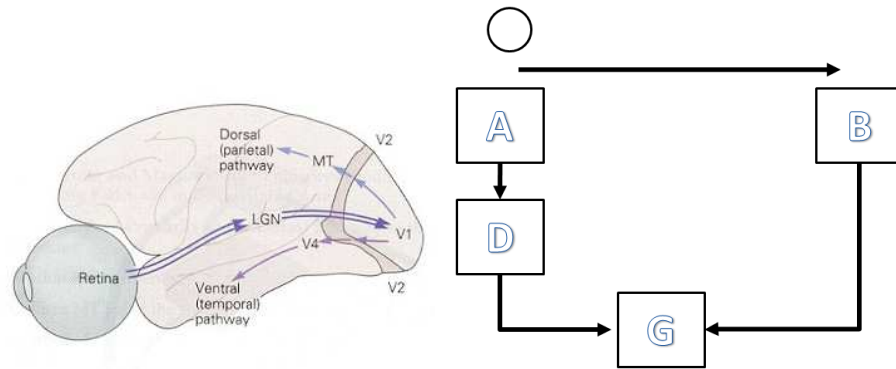


Figure 1.6: Left Image: Ventral and Dorsal Pathway. The ventral pathway is involved in object recognition, whereas the dorsal pathway processes the spatial location [91]. Right image: Scheme of a simple Reichardt's detector.

1.5.1 Tag tracking

This type of approach relies on tracking the deformation of lines generated on MR images [13, 116]. Tagging methodologies are promising, since the tags move along with the tissue, but have also certain limitations, such as:

- difficulty in tracking tags over the complete left ventricle cycle, due to decay of the tagging pattern over time.
- extraction of 3D information only after multiple acquisitions.

There are three main approaches related to tagging techniques:

- tracking intersections of tagged planes [8, 177].
- Tracking whole tag lines [71, 86]
- Tracking tag lines and tag crossings using optic flow methodologies [68, 57, 163, 59, 147, 21, 22]. This argument will be described in section 1.5.3.

Tracking intersections of tagged planes. Here each stripe is modeled as an active contour [93] and all grid intersection points belong to two stripes. In order to extract tag displacements, a minimization of a functional is computed that takes into account the pixel intensity and an internal energy functional that measures the resistance of each contour to bend and estimates the smooth displacements between snakes in successive time points. Other terms may be related to user interaction and guide each contour to the correct intersection point. In order to extract 3 dimensional motion, information related to tag

displacements of each deformed image is incorporated into a volumetric finite element model (FEM) of the endocardial and epicardial contours [177] or in a parametric cardiac kinematic model [8].

Tracking whole tag lines. Also in this case motion estimation is performed by minimizing an energy functional and feeding a kinematic cardiac model to retrieve 3-dimensional cardiac motion [71, 86]. In this approach, however, information of the whole tagging line is tracked. With respect to tracking intersections, this technique has the advantage of being more robust with respect to noise, since it uses more information of the tag line during the tracking procedure and it may provide more information in regions where few intersections occur, such as in the right ventricle, where the cardiac walls are thinner.

1.5.2 Phase Contrast Methods

In this method [109] velocity estimation is performed on the assumption that spins of protons, that move along an external magnetic field gradient, receive a shift in their phase of rotation in comparison to stationary spins. For linear field gradients, the phase shift is proportional to the velocity of the moving spins. The measurement is repeated with an inverted bipolar gradient. The value of the phase difference generated by subtracting these two data sets is used for a voxelwise calculation of velocities. In moving regions and stationary regions the phase change is different, that is the velocity of the protons is different. Moving regions are presented as black or white. Black regions exhibit motion toward the viewer, whereas white regions show motion away from the viewer. Stationary regions are illustrated in gray (Figure 1.7). In such velocity plots, the vector field extracted near the epicardial and endocardial boundaries does not present high accuracy. The reason is that the region of interest, in which the motion estimation is carried out, is large, due to signal-to-noise ratio purposes, and may contain information also of the regions outside the cardiac walls [117, 38, 180, 164, 121, 128].

1.5.3 Optic Flow methods

Optic flow methods measure the apparent motion of moving patterns in an image sequence. In the literature several approaches have been proposed and they can be classified in 3 main classes [20]:

- gradient based (or differential) methods.
- correlation-based (or area) methods.

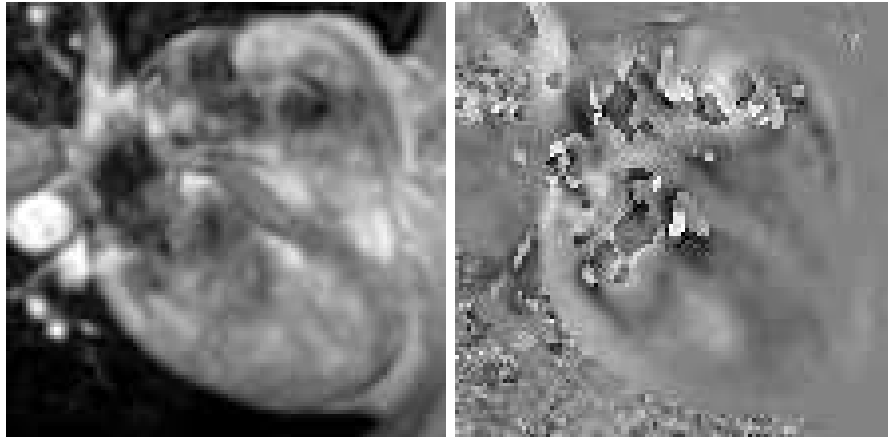


Figure 1.7: Slice from volumetric data obtained using the phase contrast methods. The image on the left displays the image magnitude. Right image is a phase contrast image. Black colors illustrate motion toward the viewer, while white colors show motion away from the viewer. Gray colors represent regions characterized by small movements. Courtesy of LUMC, Leiden, Netherlands

- frequency domain methods.

1.5.3.1 Differential Techniques

Differential techniques compute the velocity from spatiotemporal derivatives of the image intensity or filtered versions of the image. Given an image sequence $f(x, y, t) : \mathbb{R}^2 \times \mathbb{R}^+ \rightarrow \mathbb{R}$, where x , y and t represent the spatial and temporal coordinates respectively, it can be assumed that the pixel brightness does not change over a small displacement

$$f(x + \delta x, y + \delta y, t + \delta t) = f(x, y, t) \quad (1.1)$$

where $\delta x, \delta y, \delta t$ are the small displacements in space and time. Expressing the left hand side part of equation (1.1) in Taylor series, we have

$$f(x + \delta x, y + \delta y, t + \delta t) = f(x, y, t) + \frac{\partial f}{\partial x} \delta x + \frac{\partial f}{\partial y} \delta y + \frac{\partial f}{\partial t} \delta t + \epsilon \quad (1.2)$$

where ϵ contains second and higher order terms in δx , δy and δt . After substituting equation (1.2) in 1.1 and after simplifications, we obtain the so-called Optic Flow Constraint Equation (OFCE) [76]

$$\frac{\partial f}{\partial x} \frac{\delta x}{\delta t} + \frac{\partial f}{\partial y} \frac{\delta y}{\delta t} + \frac{\partial f}{\partial t} = 0 \quad (1.3)$$

where $\frac{\delta x}{\delta t} = u$, $\frac{\delta y}{\delta t} = v$ denote the velocities in x and y direction. Velocities u and v are unknown and, since there is only one equation for two unknowns, a unique solution cannot be found. This leads to the so-called "Aperture Problem", that is, it is only possible to determine the flow component normal to the image edge (Figure 1.8). In order to reduce the symbolic notation, further in this paragraph we use the convention $\frac{\partial f}{\partial x} = f_x$, $\frac{\partial f}{\partial y} = f_y$ and $\frac{\partial f}{\partial t} = f_t$.

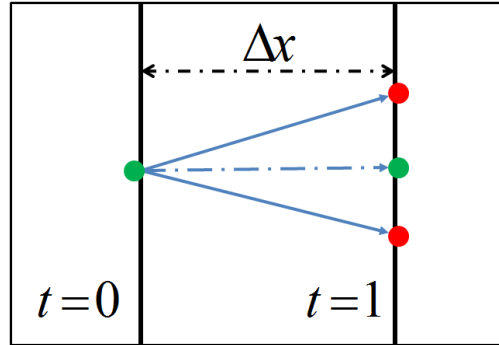


Figure 1.8: Visualisation of the aperture problem. Suppose that the green dot moves to either one of the red dots on the right. The component normal (dashed blue arrow) to the edge (left) of the moving object (black line) is the only motion component retrieved.

Differential techniques can be subdivided in 3 main categories further explained below:

- Variational optic flow techniques.
- Local differential techniques.
- Multi-scale approaches.

According to the literature, differential techniques provide the best performance in terms of error measurements [27, 28, 181], but are also sensitive to noise due to the high order of differentiation.

Variational Optic Flow Techniques. If we combine equation (1.3) (data term) with a homogeneous regularizer (smoothness term), that is, if we impose a global smoothness, we obtain the Horn and Shunck regularized optic flow technique [76]

$$\int_{\Omega \subset \mathbb{R}^2} (f_x u + f_y v + f_t)^2 + \lambda (|\nabla u|^2 + |\nabla v|^2) \mathbf{d}x \mathbf{d}y \quad (1.4)$$

where ∇ represents the gradient and λ is a positive weight which reflects the influence of the smoothness term. Large values of λ lead to a smoother flow

field. In order to extract the velocity components u and v , equation (1.4) is minimized using the Euler-Lagrange formalism. The equations are then solved numerically by iterative solvers. If we take into account the discontinuities in the image, and we model the regularization term such that we smooth isotropically at locations where the magnitude of the spatial image gradient is large, we obtain Alvarez et al. [5].

$$\int_{\Omega \subset \mathbb{R}^2} (f_x u + f_y v + f_t)^2 + \lambda w(|\nabla f|^2)(|\nabla u|^2 + |\nabla v|^2) \mathbf{d}x \mathbf{d}y \quad (1.5)$$

where $w(|\nabla f|^2) = \frac{1}{\sqrt{1 + \frac{|\nabla f|^2}{\epsilon^2}}}$ is a positive weighting function and ϵ^2 is a parameter that controls the penalization of the image gradient magnitude. In 1986 Nagel and Enkelmann [119] proposed an anisotropic image driven regularizer, where the smoothing occurred only along the component orthogonal to the local image gradient, to avoid smoothing across discontinuities in the image data:

$$\int_{\Omega \subset \mathbb{R}^2} (f_x u + f_y v + f_t)^2 + \lambda ((\nabla u)^T D_{NE}(\nabla f) \nabla u + (\nabla v)^T D_{NE}(\nabla f) \nabla v) \mathbf{d}x \mathbf{d}y \quad (1.6)$$

$$\text{where } D_{NE}(\nabla f) = \frac{1}{|\nabla f|^2 + 2\epsilon^2} \begin{bmatrix} f_y^2 + \epsilon^2 & -f_x f_y \\ -f_x f_y & f_x^2 + \epsilon^2 \end{bmatrix}.$$

At the end of the nineties Weickert and Schnoerr applied the penalization directly to the flow field. In [169] they introduced the so-called flow driven isotropic regularization, where, by reducing the smoothness at the edges of the flow, velocity contributions at the edges of the flow field were preserved:

$$\int_{\Omega \subset \mathbb{R}^2} (f_x u + f_y v + f_t)^2 + \lambda \Psi(s^2)(|\nabla u|^2 + |\nabla v|^2) \mathbf{d}x \mathbf{d}y \quad (1.7)$$

where $\Psi(s^2) = \sqrt{s^2 + \epsilon^2}$ represents a positive weighting function, where ϵ^2 is a regularization parameter.

While in (1.7) $\Psi(s^2)$ has been applied on the magnitude of the vector field, in [168] Weickert and Schnoerr propose the so-called flow driven anisotropic regularization, which takes into account also the direction of the velocity vectors, by applying $\Psi(s^2)$ on the tensor $(\nabla u)(\nabla u)^T + (\nabla v)(\nabla v)^T$.

$$\int_{\Omega \subset \mathbb{R}^2} (f_x u + f_y v + f_t)^2 + \lambda \Psi(s^2)((\nabla u)(\nabla u)^T + (\nabla v)(\nabla v)^T) \mathbf{d}x \mathbf{d}y. \quad (1.8)$$

The main advantage of these variational global techniques is that they provide a dense flow field. Variational optic flow techniques have been applied also to cardiac motion retrieval such as in [18, 68].

Local differential techniques: Lucas and Kanade method. The Lucas and Kanade approach is a local differential technique, which solves the aperture problem by assuming the flow field is constant in a small spatial neighborhood $\Omega_1 \subset \mathbb{R}^2$ [111]. Imposing Ω_1 is a window of dimension $m \times m$, velocities u and v satisfy the equation

$$AV = -b \quad (1.9)$$

$$\text{such that } A = \begin{bmatrix} f_{x1} & f_{y1} \\ f_{x2} & f_{y2} \\ \vdots & \vdots \\ f_{xm^2} & f_{ym^2} \end{bmatrix}, V = \begin{bmatrix} \tilde{u} \\ \tilde{v} \end{bmatrix} \text{ and } b = \begin{bmatrix} f_{t1} \\ f_{t2} \\ \vdots \\ f_{tm^2} \end{bmatrix}$$

where $f(x, y, t) : \mathbb{R}^2 \times \mathbb{R}^+ \rightarrow \mathbb{R}$ is an image sequence where x , y and t represent the spatial and temporal coordinates respectively.

The system is over-determined and can, for instance, be solved by least squares methods. A weighting function, such as a Gaussian function, with size $W(i, j)$ with $i, j \in \{1, \dots, m\}$, can be added in order to provide more prominence to the central pixel of the window. According to [20], the Lucas and Kanade approach presents higher robustness in the presence of noise in comparison to the variational approaches, but fails in flat regions, since the spatial gradient vanishes.

An application of the Lucas and Kanade approach to cardiac imaging has been provided by [100].

Multi-scale Methods. The scale space representation L of an image $f(x, y, t)$, with x , y and t spatial and temporal coordinates respectively, is given by the convolution between the input image sequence $f(x, y, t)$ and the spatiotemporal Gaussian kernel

$$\phi(x, y, t, \sigma, \tau) = \frac{1}{2\pi\sigma^2\sqrt{2\pi}\tau^2} e^{-\frac{1}{2}\left(\frac{x^2+y^2}{\sigma^2} + \frac{t^2}{\tau^2}\right)}.$$

Hence

$$L(x, y, t, \sigma, \tau) = f(x, y, t) * \phi(x, y, t, \sigma, \tau). \quad (1.10)$$

where $\sigma > 0$ and $\tau > 0$ denote the isotropic spatial and temporal scales respectively.

A generalization of (1.3) in the multi-scale framework has been proposed by Florack et al. [57] and Niessen et al. [122, 123]. The optic flow scheme makes use of a local polynomial expansion of the flow field (at each point) up to a certain order. For expansion up to the first order, the two components of the velocity

field are $U(x, y, t) = u + u_x x + u_y y + u_t t$ and $V(x, y, t) = v + v_x x + v_y y + v_t t$. Therefore (1.3) becomes

$$AV = -a \quad (1.11)$$

where

$$A = \begin{pmatrix} L_x & L_y & L_{xt}\tau^2 & L_{yt}\tau^2 & L_{xx}\sigma^2 & L_{xy}\sigma^2 & L_{xy}\sigma^2 & L_{yy}\sigma^2 \\ L_{xt} & L_{yt} & L_x + L_{xtt}\tau^2 & L_y + L_{ytt}\tau^2 & L_{xxt}\sigma^2 & L_{xyt}\sigma^2 & L_{xyt}\sigma^2 & L_{yyt}\sigma^2 \\ L_{xx} & L_{xy} & L_{xxt}\tau^2 & L_{xyt}\tau^2 & L_x + L_{xxx}\sigma^2 & L_y + L_{xxy}\sigma^2 & L_{xxy}\sigma^2 & L_{xyy}\sigma^2 \\ L_{xy} & L_{yy} & L_{xyt}\tau^2 & L_{yyt}\tau^2 & L_{xxy}\sigma^2 & L_{xyy}\sigma^2 & L_x\sigma^2 + L_{xxy}\sigma^2 & L_y\sigma^2 + L_{yyy}\sigma^2 \end{pmatrix}$$

$$V = (u, v, u_t, v_t, u_x, v_x, u_y, v_y)^T, a = (L_t, L_{tt}, L_{xt}, L_{yt})^T.$$

The system presents 4 equations and 8 unknowns and can be solved by adding 4 extra equations, as is done in [57, 122] by incorporating an extra constraint, such as normal flow.

Recently the multi-scale optic flow equation has been extended to applications on cardiac phase images extracted from tagged MRI [163, 59]. In this case the aperture problem was solved by applying (1.11) to two orthogonal measurements of the same moving tissue. Namely (1.11) has been applied to a sequence representing the tissue with vertical MR tags and to a sequence representing the tissue with horizontal MR tags, previously transformed into phase images.

This boils down to the following system of equations

$$BV = -b \quad (1.12)$$

where $B = \begin{bmatrix} A_{ht} \\ A_{vt} \end{bmatrix}$ and $b = \begin{bmatrix} a_{ht} \\ a_{vt} \end{bmatrix}$, where the acronyms ht and vt refer to the sequence with horizontal and vertical tags. This system presents 8 equations and 8 unknowns and can be solved uniquely.

A particular subclass of the multi-scale optic flow techniques are the *variational multi-scale feature point based methodologies*. In such approaches the motion field is measured by minimizing an energy functional, where the data term consists of velocity vectors extracted from a sparse set of so-called anchor points [165, 84, 55, 21, 22]. Anchor points are singular points of Gaussian scale space, such as extrema and saddles, for which the gradient vanishes. Critical

points move through critical paths and the creation or annihilation of the point generates so-called top points [131, 17, 85, 82]. Cardiac motion estimation based on multi-scale feature points is also one of the key subjects of this thesis. This methodology will be extensively explored in the remaining chapters of this manuscript.

1.5.3.2 Region Based Matching Techniques

Another class of optic flow techniques is region matching. The velocity is defined as the shift $d = (d_x, d_y)$ between regions of subsequent images that minimize a distance measure in order to find the best match. A commonly used distance measure is the sum of squared differences (SSD). Given an input image sequence $f(x, y, t)$, SSD is calculated as

$$SSD(x, y, d_x, d_y) = \sum_{j=-n}^n \sum_{i=-n}^n W(i, j) \times [f(x + i, y + j) - f(x + d_x + i, y + d_y + j)]^2 \quad (1.13)$$

where W is a 2-D window function and $d = (d_x, d_y)$ indicates the displacement vector in integer values. In [142, 143] Singh investigates SSD values computed from three adjacent band-pass filtered images in order to average temporal error in the SSD. Then, a Laplacian pyramid is employed to give a more symmetric distribution of the displacement estimated with the SSD. The estimates are finally plugged into a covariance matrix, whose eigenvalues produce a measure of confidence about the estimations. These approaches provide robustness with respect to numerical differentiation, noise and small number of frames, but show also less accurate velocity estimation in comparison with differential techniques, due to a weak ability of SSD to estimate subpixel displacements [20]. In cardiac motion estimation region matching techniques are especially used for ultrasound speckle tracking [24, 105].

1.5.3.3 Frequency Based Techniques

In frequency based techniques, velocity extraction is carried out in the Fourier domain. The Fourier transform of a uniformly translating 2-D pattern $f(x, y, t)$ is:

$$\hat{f}(\mathbf{k}, \omega) = \hat{f}_0(\mathbf{k})\delta(\omega + \mathbf{v}^T \mathbf{k}) \quad (1.14)$$

where $\hat{f}_0(\mathbf{k})$ is the Fourier transform of $f(x, y, 0)$, $\delta(k)$ is a Dirac delta function, ω is the temporal frequency, $\mathbf{k} = (k_x, k_y)$ is the spatial frequency and $\mathbf{v} = (\hat{u}, \hat{v})$ are the components of the velocity in the frequency domain. Equation (1.14)

does not vanish in the so-called *motion plane* [129]. This plane passes through the origin of the frequency domain and therefore

$$\omega + \mathbf{v}^T \mathbf{k} = 0. \quad (1.15)$$

Equation (1.15) represents the (OFCE) in the Fourier domain. In order to find a solution Heeger [75] expresses the expected velocity components in terms of energy, using Gabor filters. Then he applies a least square fit to minimize the difference between the predicted and measured motion energies.

Frequency-based methods are in general more robust to noise with respect to differential methods. Frequency techniques, however, are sensitive to temporal aliasing and present high computational cost since they involve a large number of filters. An example of cardiac motion estimation using frequency based techniques has been discussed in [32].

1.6 Thesis Outline

The outline of this thesis is as follows.

Chapter 2 discusses a new scale space feature based optic flow method with a regularization term described in terms of the so-called covariant derivatives. This regularization term takes into account prior notion of the velocity field, which is employed to influence the final motion field reconstruction. Experiments on an artificial phantom for which the ground truth is known and comparison with similar techniques, where prior knowledge of the vector field was not used, emphasize the high improvements in the accuracy of the reconstructed vector field provided by the new method.

Chapter 3 extensively illustrates the framework behind the new regularizer based on covariant derivatives. The chapter tackles also another issue: the heart movement can be described in terms of contractions and rotations. Therefore, the regularizer is also combined with the so-called Helmholtz decomposition. This is a decomposition of a vector field in its divergence-free and rotation-free components. Following this assumption, the vector field extraction will be carried out by first reconstructing the dense divergence-free and rotation-free parts from the extraction in a sparse set of points separately, and then combining the two components into the final vector field. This has the advantage to allow a separate tuning in reconstructing the two components. Experiments and comparisons with methods where the decomposition is not employed will show an increase in performance for the newly proposed approach.

In chapter 4 the new optic flow methodology will be applied on datasets of a group of volunteers and a patient. Helmholtz decomposition gives informa-

tion of the rotating and contracting contributions to the cardiac motion in each phase of the cardiac cycle. Quantification of such contributions will be expressed in parameters such as kinetic energy. Local measurements suggest that regions with a "sudden" local kinetic energy minimum can be related to infarcted area. Therefore such measurements may be crucial additions to the toolbox of physicians in their usual practice.

Chapter 5 provides a comparison of the performance of the proposed optic flow method and the performance of other widely used cardiac motion estimation methods in the literature such as [76, 111, 163]. Assessment on a phantom with a known ground truth shows that the proposed optic flow algorithm provides the most accurate velocity field estimations.

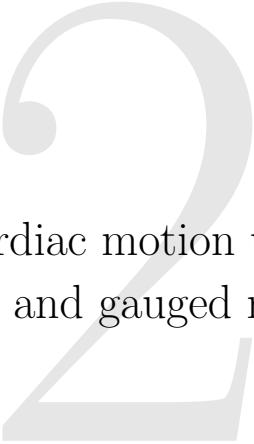
In chapter 6 a reformulation of the so-called winding number - a topological number - for 3-dimensional critical point extraction will be proposed. In this approach the simplification of the mathematics and the implementation involved with respect to previous work [150] will be presented. Tests on a variety of applications such as ovarian follicle and neuronal cell counting, and 3-dimensional cardiac motion estimation of a tagged MRI sequence have been provided.

Chapter 7 illustrates the application on 3-dimensional tagged MRI of a scale space feature optic flow method with regularized standard derivatives. This approach successfully estimates expansions, contractions, twistings and through plane velocity components of the cardiac motion. These velocity fields provide more information on heart behaviour in comparison to motion fields extracted by 2-dimensional approaches, since in this latest case the through-plane component is not estimated.

In chapter 8 the work concludes with a discussion of future directions opened by the proposed methods.

*I can calculate the motion of heavenly bodies, but
not the madness of people.*

Isaac Newton



Extraction of cardiac motion using scale-space feature points and gauged reconstruction

This chapter is based on:

Becciu, A., Assen, H.C. van, Florack, L.M.J., Janssen, B.J, Haar Romenij, B.M. ter. Cardiac motion estimation using multi-scale feature points. In *Computational Biomechanics for Medicine III : Proceedings of the MICCAI Workshop*. Midas Journal, Vol. 13(229), pp. 5-14, 2008.

Becciu, A., Janssen, B.J, Assen, H.C. van, Florack, L.M.J., Roode, V.J., Haar Romenij, B.M. ter. Extraction of cardiac motion using scale-space feature points and gauged reconstruction. In *International Conference on Computer Analysis of Images and Patterns (CAIP)*. Lecture Notes in Computer Science, Vol. 5702, pp. 598-605, 2009.

Abstract

Motion estimation is an important topic in medical image analysis. The investigation and quantification of, e.g., the cardiac movement is important for assessment of cardiac abnormalities and to get an indication of response to therapy. In this chapter we present a new aperture problem-free method to track cardiac motion from 2-dimensional MR tagged images and corresponding sine-phase images. Tracking is achieved by following the movement of scale-space critical points such as maxima, minima and saddles. Reconstruction of the dense velocity field is carried out by minimizing an energy functional with a regularization term influenced by covariant derivatives.

As MR tags deform along with the tissue, a combination of MR tagged images and sine-phase images was employed to produce a regular grid from which the scale-space critical points were retrieved. Experiments were carried out on real image data, and on artificial phantom data from which the ground truth is known. A comparison between our new method and a similar technique based on homogeneous diffusion regularization and standard derivatives shows a notable increase in performance. Qualitative and quantitative evaluation emphasize the reliability of the dense motion field allowing further analysis of deformation and torsion of the cardiac wall.

2.1 Introduction

Among the available techniques, optic flow of tagged MR acquisitions is a non-invasive method that can be employed to retrieve cardiac movement. Optic flow provides information about the displacement field between two consecutive frames, that is, it measures the apparent motion of moving patterns in image sequences. In several optic flow methods it is assumed that brightness does not change along the displacement field and the motion is estimated by solving the so-called Optic Flow Constraint Equation (OFCE):

$$L_x u + L_y v + L_t = 0 \quad (2.1)$$

where $L(x, y, t) : \mathbb{R}^3 \rightarrow \mathbb{R}$ is an image sequence, L_x, L_y, L_t are the spatiotemporal derivatives, $u(x, y, t), v(x, y, t) : \mathbb{R}^3 \rightarrow \mathbb{R}$ are unknown and to be established, sought velocity vectors and x, y and t are the spatial and temporal coordinates respectively. Equation (2.1) is ill-posed since its solution is not unique, due to the two unknown velocities u and v . This has been referred to as the "aperture problem". In order to overcome the problem, Horn and Schunck [76] introduced a gradient constraint in the global smoothness term, finding the solution by minimizing an energy functional. Lately results were impressively improved by Bruhn et al. [28], who combined the robustness of local methods with the full density of global techniques using a multigrid approach.

Motion estimation has also been performed by means of feature tracking. Thyriou [154] investigated a technique where the brightness is preserved and the features are driven to the most likely positions by forces. Cheng and Li [36] explored optic flow methods where features are extracted taking into account scatter of brightness, edge acquisition and features orientation. A multi-scale approach to equation (2.1) has been first proposed by Florack et al. [57] and an extension to the technique and an application to cardiac MR images has been investigated by Van Assen et al. and Florack and Van Assen [163, 59]. In this chapter we estimate the 2-dimensional cardiac wall motion by employing an optic flow method based on features points such as maxima, minima and saddles. The features have been calculated in the robust scale-space framework, which is inspired by findings from the human visual system. Moreover, our technique does not suffer from the aperture problem and is also not dependent on the constant brightness assumption, since we assume that critical points retrieved at tag crossings, such as from the grid pattern described in section 2.2, still remain critical points after a displacement, even in the presence of fading. Therefore, the algorithm can be robustly applied on image sequences, such as the tagged MR images, where the intensity constancy is not preserved. The reconstruction of the velocity field has been carried out by variational methods and the regularization component is described in terms of covariant derivatives influenced by vector fields acquired previously. In this work we add vector field information from previous frames, which allows a better velocity field reconstruction with respect to the one provided by similar techniques which employ standard derivatives. Tests have been carried out on phantom image sequences with a known ground truth and real images from a volunteer. The outcomes emphasize the reliability of the vector field. In section 2.2 the image data-set and the preprocessing approach used in the experiments is presented. In section 2.3 the multi-scale framework and the topological number, introduced as a convenient technique for extracting multi-scale features, are explored. In section 2.4 and 2.5, we present the calculation of a sparse velocity vector field and the dense flow's reconstruction technique. Finally, in section 2.6 and 2.7 the evaluation, the results and the future directions are discussed.

2.2 Image data-set and preprocessing approach

Tagging is a method for noninvasive assessment of myocardial motion. An artificial brightness pattern, represented as dark stripes, is superimposed on images by spatially modulating magnetization with the aim to improve the visualization and quantification of intramyocardial motion [179] (Figure 2.1 column 1). In 1999 Osman et al. [126] introduced the so-called HARMONIC Phase (HARP) technique which overcomes the fading problem by taking into account the spatial information from the inverse Fourier transform of the filtered images. Our experiments have been carried out by employing a similar technique based on

Gabor filters [64]. After acquisition of two tagged image series with mutually perpendicular tag lines (Figure 2.1 column 1), the first harmonic peak has been retained using a band-pass filter in the Fourier domain and the inverse Fourier transform has been applied to the resulting image spectrum. The filtered images present a saw tooth pattern, whose phase varies from 0 to 2π . In the experiments a sine function has been applied to the phase images to avoid spatial discontinuities due to the saw tooth pattern (Figure 2.1 column 2). A combination of sine phase frames generate a grid from which the critical feature points (maxima, minima, saddles) have been extracted (Figure 2.1 column 3).

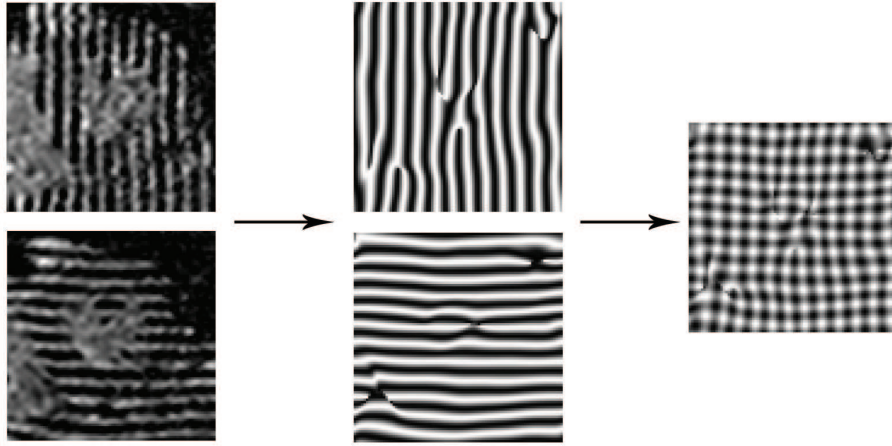


Figure 2.1: Column 1: Short axis view of a volunteer’s left ventricle. Column 2. The tagged MR images have been filtered in the Fourier domain. Successively inverse Fourier transform and sine function have been applied. Column 3. Image obtained by combination of sine-phase images. The image provides a new pattern from which the feature points have been retrieved.

2.3 Extraction of scale-space critical points

In the real world, objects are processed by the visual system at different scale levels. Given a static 2-dimensional image $f(x, y) \in \mathbb{L}_2(\mathbb{R}^2)$, its scale space representation $L(x, y; s) \in \mathbb{L}_2(\mathbb{R}^2 \times \mathbb{R}^+)$ is generated by the spatial convolution with a Gaussian kernel $\phi(x, y; s) = \frac{1}{4\pi s} \exp(-\frac{x^2+y^2}{4s})$ such that

$$L(x, y; s) = (f * \phi)(x, y; s) \tag{2.2}$$

where x and y are the spatial coordinates, and $s \in \mathbb{R}^+$ denotes the scale. Equation (2.2) generates a family of blurred versions of the image, where the

degree of blurring is determined by the scale [94, 151, 54].

Singularities (critical points) induced by the MR tagging pattern are interesting candidates for structural descriptions. Detection and classification of critical points can be performed in an efficient way by the computation of the so-called topological number [146, 89, 90]. We examine a point P in image L and its neighborhood N_P . Suppose that N_P does not have any other critical points with exception of the point P itself, and suppose ∂N_P is the boundary of N_P , which is a $D - 1$ dimensional oriented closed hypersurface. Since there are no critical points at ∂N_P , the normalized gradient of the image L on ∂N_P is defined component-wise as: $\xi_i = \frac{L_i}{\sqrt{L_i L_j}}$ with $L_i = \partial_i L$ and $i = (1, \dots, D)$ (summation convention applies. Here we have $D = 2$). For a non-singular point we may define the $D - 1$ dimensional form

$$\Phi = \xi_{i_1} \mathbf{d}\xi_{i_2} \wedge \dots \wedge \xi_{i_D} \varepsilon^{i_1, \dots, i_D} \quad (2.3)$$

where the symbol \wedge represents the wedge product and $\varepsilon^{i_1, \dots, i_D}$ is the permutation tensor of order D such that

$$\varepsilon^{i_1, \dots, i_l \dots i_k, \dots, i_D} = \begin{cases} +1 & \text{if } i_1, \dots, i_l \dots i_k, \dots, i_D \text{ is an even permutation} \\ -1 & \text{if } i_1, \dots, i_l \dots i_k, \dots, i_D \text{ is an odd permutation} \\ 0 & \text{if any two labels are the same.} \end{cases}$$

In 3D the permutation tensor is

$$\varepsilon^{i_1, i_2, i_3} = \begin{cases} +1 & \text{if } \{i_1, i_2, i_3\}, \{i_3, i_1, i_2\}, \{i_2, i_3, i_1\} \\ -1 & \text{if } \{i_1, i_3, i_2\}, \{i_3, i_2, i_1\}, \{i_2, i_1, i_3\} \\ 0 & \text{otherwise: } i_1 = i_2 \text{ or } i_2 = i_3 \text{ or } i_3 = i_1. \end{cases}$$

Making the substitution of ξ_i in Φ we obtain:

$$\Phi = \frac{L_{i_1} \mathbf{d}L_{i_2} \wedge \dots \wedge L_{i_D} \varepsilon^{i_1, \dots, i_D}}{(L_j L_j)^{D/2}} \quad (2.4)$$

The topological number can then be defined as

$$\nu_{\partial N_P} = \frac{1}{A_D} \oint_{\mathbf{x} \in \partial N_P} \Phi(\mathbf{x}) \quad (2.5)$$

where A_D represents the area enclosed by ∂N_P . In 2-dimensional images the topological point is referred as the *winding number* and represents the integrated change of angle of the gradient vector when traversing any closed curve in a plane around a point. In two dimensions, equation (2.3) and (2.5) can be represented in a convenient way using complex numbers. Given the complex couple of coordinates $z = x + iy$ and the complex conjugate $\bar{z} = x - iy$, the gradient vector field of the image $L(z, \bar{z})$ can be expressed as $W = (L_x + iL_y)/2 \equiv \partial_{\bar{z}}L(z; \bar{z})$. Hence, expression (2.3) can be written as

$$\begin{aligned} \Phi &= \xi_x \mathbf{d}\xi_y - \xi_y \mathbf{d}\xi_x = \frac{L_x \mathbf{d}L_y - L_y \mathbf{d}L_x}{L_x L_x + L_y L_y} = \\ \text{Im} \frac{L_x - iL_y \mathbf{d}(L_x + iL_y)}{L_x L_x + L_y L_y} &= \text{Im} \left(\frac{\mathbf{d}W}{W} \right) = \text{Im}(\mathbf{d} \ln W) \end{aligned} \quad (2.6)$$

where $\ln W = \ln |W| + i \arg W$. Φ can, therefore, be read as the angle change of the gradient field.

The winding number is always an integer multiple of 2π and its value provides information of the detected critical point. The winding number is zero for regular points, it is $+2\pi$ for extrema, and -2π for saddle points, -4π (and higher) for monkey saddles (and more complex saddles). Finally, winding numbers superimpose; when more singular points are inside the closed path, they add to a new number. In chapter 6 we discuss theory and applications for the 3-dimensional winding number.

2.4 Sparse feature point velocity estimation

MR tags have the property to move along with the moving tissue, critical points are located on and between the tag's crossings and therefore also move along with tissue. At a critical point's position the image gradient vanishes. Tag fading, which is a typical artifact in MR images, leaves this property intact, hence critical points satisfy equation (2.7) over time

$$\nabla L(x(t), y(t), t) = 0 \quad (2.7)$$

where ∇ represents the spatial gradient and $L(x(t), y(t), t)$ denotes intensity at position x, y and time t . If we differentiate equation (2.7) with respect to time t and apply the chain rule for implicit functions, we obtain

$$\frac{d}{dt} [\nabla L(x(t), y(t), t)] = \begin{bmatrix} L_{xx}u_i + L_{xy}v_i + L_{xt} \\ L_{yx}u_i + L_{yy}v_i + L_{yt} \end{bmatrix} = 0 \quad (2.8)$$

where $\frac{d}{dt}$ is the total time derivative, and where we have dropped space-time arguments on the right hand side in favor of readability. Equation (2.8) can

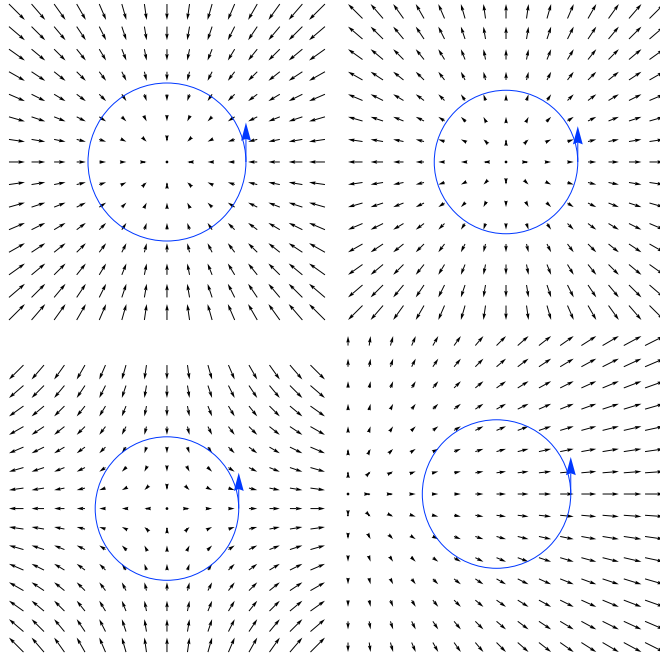


Figure 2.2: Gradient vector fields and winding number (ν) path. Row 1: left image, maximum ($\nu = 2\pi$), right image, minimum ($\nu = 2\pi$). Row 2: left image, saddle ($\nu = -2\pi$), right image, regular point ($\nu = 0$). Plots adopted from [151].

also be written as:

$$\begin{bmatrix} u_i \\ v_i \end{bmatrix} = -HL^{-1} \frac{\partial \nabla L^T}{\partial t} \quad (2.9)$$

where H represents the Hessian matrix of $L(x(t), y(t), t)$ and T indicates transpose. Equation (2.9) provides the velocity field at critical point positions. The scalars u_i , v_i represent the horizontal and vertical components of a sparse velocity vector at position x_i and y_i , with $i = 1 \dots N$ where N denotes the amount of critical points.

2.5 Reconstruction of the dense velocity field

We aim to reconstruct a dense motion field that provides the most accurate approximation of the true velocity field making use of sparse velocities calculated by equation (2.9). In literature, examples of velocity field reconstruction as well as image reconstruction techniques based on features can be found in [55, 84, 85, 106]. Given the horizontal and vertical components of the true dense velocity field u_{tf} and v_{tf} , we extract a set of velocity features at scale s_i , such that $u_i = (\phi_i, u_{tf})$ and $v_i = (\phi_i, v_{tf})$, where $(\cdot, \cdot)_{\mathbb{L}_2}$ denotes the \mathbb{L}_2 in-

ner product, ϕ_i is the Gaussian kernel $\phi_i(x_i, y_i; s_i) = \frac{1}{4\pi s} \exp(-\frac{(x-x_i)^2+(y-y_i)^2}{4s})$. We look for the scalar functions U and V such that $(\phi_i, U)_{\mathbb{L}_2} \approx (\phi_i, u_{tf})_{\mathbb{L}_2}$ and $(\phi_i, V)_{\mathbb{L}_2} \approx (\phi_i, v_{tf})_{\mathbb{L}_2}$, and minimize the energy functional

$$E(U, V) = \sum_{i=1}^N \alpha_i ((\phi_i, U)_{\mathbb{L}_2} - u_i)^2 + \alpha_i ((\phi_i, V)_{\mathbb{L}_2} - v_i)^2 + \frac{\lambda}{2} \int_{\mathbb{R}^2} \|\nabla U\|^2 + \|\nabla V\|^2 dx dy \quad (2.10)$$

where $\alpha_i \in \mathbb{R}^+$ is a weighting factor for each feature and the parameter $\lambda \in \mathbb{R}^+$ controls the quality of the approximation. As λ increases, the smoothness degree in the vector field increases, reducing the influence of the sparse velocity vectors. The minimization of equation (2.10) is carried out by solving the corresponding Euler-Lagrange equations [49]. In equation (2.10) we have chosen a weighting factor $\alpha_i \in \mathbb{R}^+$, such that, $\alpha_i(c_i, \beta) = 1 - \exp(\frac{-\beta}{(c_i-1)^2})$. The justification for α_i is as follows: the weighting factor α ranges from 0 to 1 and depends on an arbitrary parameter $\beta \in \mathbb{R}^+$ and on c_i , the condition number of the Hessian matrix in equation (2.9). The condition number of a matrix M is defined as $c(M) = \|M^{-1}\| \cdot \|M\|$ [125]. Its value varies from 1 to infinity and gives an indication of the sensitivity of a matrix to numerical operations. In case of a high condition number, the solution of equation (2.9) is less accurate and the retrieved velocities are weighted by a small α .

In the next step the velocity field reconstruction is influenced by a certain vector field $h \in \mathbb{R}^2$, called gauge field, with components $h = \{U_h, V_h\}$, called gauge functions. In equation (2.10) the gradient of the regularization term is replaced by the so-called covariant derivatives. In this work the covariant derivatives of scalar functions U and V biased by scalar functions U_h and V_h are defined as

$$\begin{aligned} D^{U_h} U &= \partial_{x^i} U - \frac{\partial_{x^i} U_h}{U_h} U \\ D^{V_h} V &= \partial_{x^i} V - \frac{\partial_{x^i} V_h}{V_h} V \end{aligned} \quad (2.11)$$

where ∂_{x^i} indicates the derivative operator with respect to coordinates $\{x^1, x^2\} = \{x, y\}$. Equation (2.10) can now be written in terms of covariant derivatives, hence

$$E(U, V) = \sum_{i=1}^N \alpha_i ((\phi_i, U)_{\mathbb{L}_2} - u_i)^2 + \alpha_i ((\phi_i, V)_{\mathbb{L}_2} - v_i)^2 + \frac{\lambda}{2} \int_{\mathbb{R}^2} \|D^{U_h} U\|^2 + \|D^{V_h} V\|^2 dx dy. \quad (2.12)$$

In equation (2.10) the regularization term selects U and V from all possible approximations to the solution such that they are as smooth as possible (gradient

is minimized). In the regularization term of equation (2.12), scalar functions U_h and V_h are used to tune the covariant derivatives, therefore deviations from U_h and V_h are penalized. This means, that in case the vector field h is similar to what we are expecting, the regularization term will take into account this information, and therefore this may positively influence the reconstruction of U and V . A detailed description of the method for image reconstruction is given in [83].

In the evaluation, we first compute the motion field using equation (2.10) and we use the vector field at frame j as the vector field h . The vector field h is then applied to equation (2.12), with the aim to influence the reconstruction of vector field at frame $j + 1$. In the same way, the vector field at frame $j + 1$ computed by equation (2.12) is used as vector field h and provides the information to construct the velocity field at frame $j + 2$. The process is performed for all frames in the sequence.

2.6 Evaluation

We compare the performance of our optic flow algorithm with the reconstruction technique based on covariant derivatives as described in section 2.5 with a similar method based on conventional derivatives. The accuracy of the retrieved vector fields has been assessed by analyzing a contracting and expanding artificial phantom of 19 frames and resolution of 99×99 pixels. The artificial phantom presents a pattern similar to Figure 2.1 column 3 and deforms according to the analytic function $a(x, y, t) = \left\{ \frac{(x-l)(m-2n \cdot t)}{(l+(m-n \cdot t)t)}, \frac{(y-l)(m-2n \cdot t)}{(l+(m-n \cdot t)t)} \right\}$, which provides also the vector field's ground truth. The variables x, y, t represent the spatial and temporal coordinates, whereas l, m, n are constant parameters set to 50, 5, and 0.25 respectively. The retrieved vector field and the true vector field of frame 6 are displayed in Figure 2.3, column 1 and 2 respectively. In the tests we have employed feature points such as maxima, minima and saddles at 4 spatial scales $\sigma = \{1, 1.3, 1.6, 2.\}$ and time scale 1. In order to reduce the influence of velocity outliers during the reconstruction process, sparse velocity vectors extracted using equation (2.9) have been weighted by employing the weighting function $\alpha(c, \beta)$ dependent on the condition number c and parameter β , which we set to 50. Figure 2.4, column 1 and 2 illustrate the effects of the weighting function on frame 5 of the real sequence. Moreover, the smoothing parameter λ has been optimized for equation (2.10) and (2.12). Best performance has been achieved with $\lambda = 10^{-2}$ and $\lambda = 10^{-0.5}$ respectively. In order to avoid outlier vectors at the boundaries, the two reconstruction methods have been assessed from frame 5 to frame 9, and 10 pixels distant from the boundaries. The test evaluation has been conducted by comparing the extracted flow field with the corresponding ground truth, whereas the accuracy in the results

has been described in terms of the so-called *Angular Error* [20]. The outcomes, illustrated in Table 2.1, emphasize an increase in performance for our optic flow algorithm with reconstruction technique based on covariant derivatives. Moreover, once we reconstruct the vector field for all image sequences using equation (2.12), we can employ this new motion field as gauge fields and apply equation (2.12) again. Outcomes of this process have shown further improvements in the accuracy for our tests. This procedure can be carried out iteratively.

We have also applied our optic flow method on a real sequence of 11 tagged MR images with a resolution of 86×86 pixels, which depicts the left ventricle of a volunteer in the phase of contraction. The filtered vector fields on sine HARP frame 5, 6, 7, and 8 are displayed in Figure 2.5. The plots are color encoded, where the color gives information of the vector direction.

Feature	Maxima		Minima		Saddles	
	AAE	Std	AAE	Std	AAE	Std
Conventional Derivatives	2.35°	1.72°	3.15°	1.47°	1.54°	2.06°
Covariant Derivatives	1.90°	2.11°	1.55°	1.00°	1.34°	1.12°
Covariant Derivatives 1 Iterations	1.88°	1.07°	1.53°	1.00°	1.33°	1.12°

Table 2.1: Performance of the vector field reconstruction methods based on conventional derivatives and covariant derivatives. The methods have been tested on an artificial contracting phantom using maxima, minima and saddles as feature points at spatial scales $\sigma = \{1, 1.3, 1.6, 2.\}$ and time scale 1. The accuracy of the method has been described in terms of average angular error (AAE) and standard deviation (Std) both expressed in degrees. Best performance has been achieved by the employment of covariant derivatives after 1 iteration with $AAE = \{1.88^\circ, 1.53^\circ, 1.33^\circ\}$ for maxima, minima and saddles respectively. The error measurements are averaged over the investigated 4 frames.

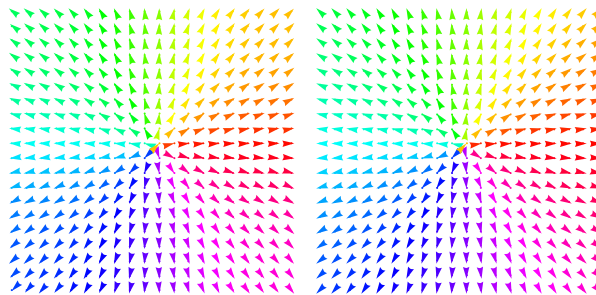


Figure 2.3: Vector Fields. Plots depict the vector field of frame 6 extracted from our artificial phantom (left) and the respective ground truth (right).

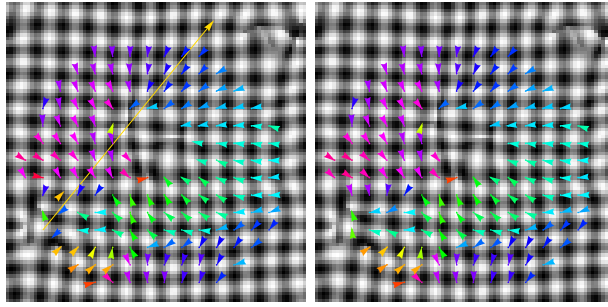


Figure 2.4: Motion field of frame 5 retrieved from real data before and after the weighting procedure, where outliers have been penalized using the outcome coming from the condition number of the Hessian matrix of equation 2.9.

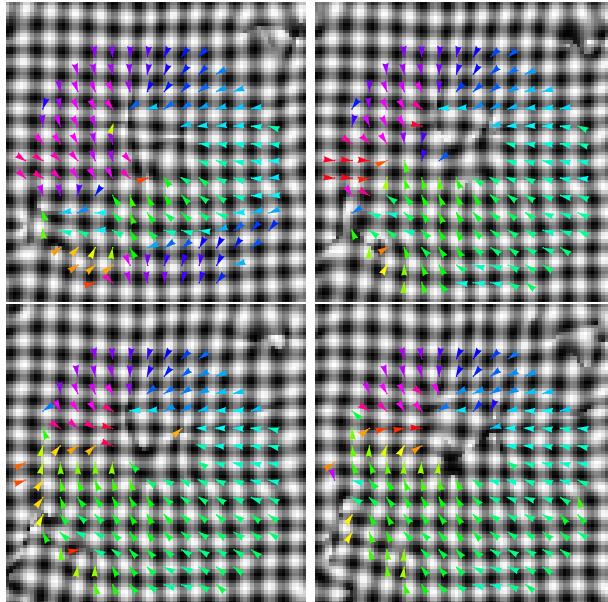


Figure 2.5: Motion fields of frames 5, 6, 7 and 8, extracted from sequence of sine HARP images of real data. The direction of the velocity vectors is color-encoded, that is, regions in the motion field with the same color show vectors that are pointing in the same direction.

2.7 Conclusion

We analyze cardiac motion by employing a new optic flow feature based method with regularization term described by covariant derivatives influenced by a gauge field. We have tested the technique on an artificial contracting and expanding phantom of which we know the ground truth, using maxima, minima and saddles as feature points. Outcomes of the comparison with a similar approach, based on conventional derivatives, emphasize high improvements in

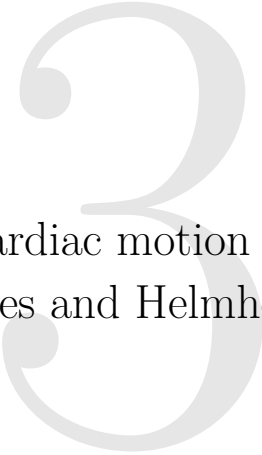
the accuracy reconstruction provided by our new method. The average angular error of motion fields reconstructed using maxima, minima and saddle as feature points decreased of 19.1% , 50.7% and 13% respectively.

We have also shown that further improvements in the accuracy are achieved, in case the method is repeated one second time with a gauge field based on the vector field calculated using covariant derivatives. In this case the average angular error decreased of 1%, 1.3% and 0.74% respectively for motion field estimation using maxima, minima and saddles.

We have applied moreover the technique to a real tagged MR image sequence displaying a heart in phase of contraction. Qualitative results highlight the reliability of the extracted vector field. Finally, in a test evaluation we calculate velocity fields at fixed scales, where the most suitable scale is chosen according to the performance with respect to the ground truth. However, deformations of the cardiac walls differ in different regions, therefore features belonging to two different regions may present the best performance at different scales. In the next chapter we take into account this issue by introducing a new scale selection method based on drift velocities. We provide furthermore an extensive theoretical explanation of the regularization approach and we study the motion field by decomposing it in its rotation free and divergence free components.

Vision is the art of seeing what is invisible to others.

Jonathan Swift, poet



Feature based cardiac motion estimation using covariant derivatives and Helmholtz decomposition

This chapter is adapted from:

Becciu A., Duits R., Janssen B.J., Florack L.M.J., ter Haar Romenij B.M. and van Assen, H.C. Feature based optic flow estimation using covariant derivatives and Helmholtz decomposition: Application to cardiac tagged MRI sequences. To be submitted to the international journal *IEEE Transactions on Medical Imaging*.

Duits, R., Becciu, A., Janssen, B.J, Florack, L.M.J., Assen, H.C. van, Haar Romenij, B.M. ter. Cardiac motion estimation using covariant derivatives and Helmholtz decomposition. *CASA Report* No. 10-31, Eindhoven: Technische Universiteit Eindhoven, 40 pp.(2010)

Note This work was carried out in close cooperation with Dr Remco Duits. The idea of combining the covariant derivatives with the Helmholtz decomposition for vector fields is of both authors. The theory was developed by Remco Duits. The author of this thesis adapted the algorithms for applications on cardiac motion estimation and carried out all the numerical experiments.

Abstract

The investigation and quantification of cardiac movement is important for the assessment of cardiac abnormalities and treatment effectiveness. Therefore we consider a new aperture-problem-free method to track cardiac motion from 2-dimensional MR tagged images and corresponding sine-phase images. Tracking is achieved by following the movement of scale-space maxima, yielding a sparse sampling of the unknown dense optic flow vector field. Interpolation/reconstruction of the velocity field is then carried out by minimizing an energy functional expressed in covariant derivatives (rather than standard derivatives). These covariant derivatives are used to express prior knowledge about the velocity field in the variational framework employed. Furthermore, the optic flow vector field is decomposed in a divergence-free and a rotation-free part, using our multi-scale Helmholtz decomposition algorithm. Finally, this multi-scale Helmholtz decomposition is combined with vector field reconstruction (based on covariant derivatives) in a single algorithm and present some experiments of cardiac motion estimation are presented.

Further experiments on phantom data with ground truth show that both the inclusion of covariant derivatives and of the multi-scale Helmholtz decomposition improve markedly the optic flow reconstruction.

3.1 Introduction

In cardiology literature [51] it has been noted that variation in movement of the cardiac wall may provide a quantitative indication of the health of the cardiac muscle. Cardiac motion extraction is therefore an important area of research. Monitoring and quantification of irregular cardiac wall motion may help in early diagnosis of cardiac abnormalities such as ischemia, area of tissue suffering from obstruction of blood circulation, as well as in providing information about the effectiveness of treatment. In order to characterize the contracting behavior of the cardiac muscle, non-invasive acquisition techniques such as MR tagging can be applied. This methodology allows to locally imprint brightness patterns in the muscle, which deform according to the cardiac muscle and aid to retrieve motion within the heart walls.

At the beginning of the eighties Horn and Schunck introduced a mathematical formulation of optic flow assuming that intensities associated to image objects

did not change along the sequence, [76]. This formulation has been referred to as the Optic Flow Constraint Equation (OFCE):

$$f_x u + f_y v + f_t = 0 \quad (3.1)$$

where $(x, y, t) \rightarrow f(x, y, t) : \mathbb{R}^2 \times \mathbb{R}^+ \rightarrow \mathbb{R}$ is an image sequence, f_x, f_y, f_t are the spatial and temporal derivatives; $\mathbf{v}(\cdot, t)$ is a vector field on \mathbb{R}^2 given by $\mathbf{v}(x, y, t) = (u(x, y, t), v(x, y, t))^T$, where u and v are unknown and x, y and t are the spatial and temporal coordinates respectively. Since scalar-valued functions u and v are unknown, equation (3.1) does not generate a unique solution, caused by the so-called "aperture problem" and therefore Horn and Schunck added a homogeneous smoothness constraint based on the gradient magnitude to a data term, equation (3.1), and minimized the energy functional using a variational approach [76]. A similar scheme has been employed in more recent and sophisticated techniques by Bruhn et al. [28] and Zimmer et al. [181], who used an anisotropic smoothness term and carried out tests on the Yosemite sequence [133] and Middlebury benchmark [175] outperforming the results of most of the current optic flow methods. A multi-scale extension of equation (3.1) has been investigated by Florack et al. [57] and has adopted for cardiac MR images in [59, 122, 147, 163].

Extraction of object displacements has been studied also by means of feature tracking. Thirion [154] has investigated a technique, in which the brightness is preserved and the features are driven to the most likely positions by forces. Janssen et al. and Van Dorst et al. [165, 84] propose multi-scale feature based optic flow methods, where the reconstruction of the dense flow field is obtained from a sparse set of velocities associated to multi-scale anchor points. These last methods, however, are rather general and are not tuned for applications on cardiac motion estimation.

In this chapter the properties of the velocity field generated by rotation and compressibility of the cardiac tissue are taken into account are used during the evaluation of the motion field. This will lead to an improvement of the final result.

Local rotation and contraction of the cardiac muscle can be calculated by investigating the divergence-free and rotation-free parts resulting from the well-known Helmholtz decomposition [10, 167]. This allows to estimate the motion field for the two separate components and to optimize separately the parameters involved in the motion estimation algorithm.

Exploring this decomposition may also play a fundamental role in the clinical diagnosis procedure, since it reveals the essential components of the heart movement. Therefore, for applications such as cardiac motion extraction, blood flow calculation and fluid motion analysis information of these properties may be more suitable. Examples of such optic flow methods have been provided by

[39, 69, 95, 178].

In this work we extract 2-dimensional cardiac wall motion by employing an optic flow method based on feature points: maxima. The dense flow field is reconstructed by employing variational methods; in the smoothness term information obtained by our multi-scale Helmholtz decomposition is included and the regularization components are described in terms of covariant derivatives biased by a gauge field. Advantages of this approach are significant:

- (i) This method does not suffer from the aperture problem.
- (ii) The features are not dependent on constant brightness, since critical points such as maxima will retain their characterization even after occurrence of fading in the image. Therefore, the algorithm can be robustly applied on image sequences (like tagged MR images) in which the intensity constancy is not preserved.
- (iii) The proposed technique takes into account the contraction and rotation of the heart muscle by means of a multi-scale Helmholtz decomposition.
- (iv) The algorithm benefits from the advantages provided by a multi-scale approach:
 - An adaptive scale selection scheme for the feature points has been introduced in this chapter.
 - In our multi-scale approach we *analytically pre-compute* the concatenation of the linear diffusion operator combined with Helmholtz decomposition in order to avoid grid artifacts.
- (v) Finally a new regularization component described in terms of covariant derivatives is investigated. The regularization term includes information from a so-called gauge field and allows a better flow field reconstruction with respect to the one provided by similar techniques, which use standard derivatives [21] instead. For a different optic flow approach where pre-knowledge in the regularization term is included we refer to Nir et al. [124].

The algorithm performance is assessed with two phantoms of which the ground truth is known and tests have been carried out with real data obtained from a patient with myocardial infarcts and a healthy volunteer. Tests on the two phantoms reveal that the proposed optic flow approach improves the motion field reconstruction by roughly 20% with respect to similar methods that do not include the covariant derivatives and multi-scale Helmholtz decomposition in the smoothness term of the energy functional.

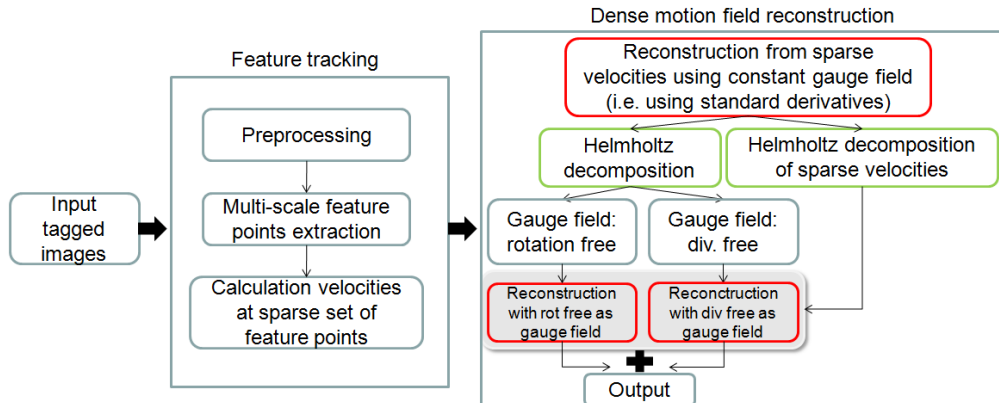


Figure 3.1: Overview of the algorithm. The box on the right shows how the Helmholtz decomposition and covariant derivatives are applied in the dense motion field reconstruction.

Outline of algorithm and chapter

An overview of the proposed algorithm is provided in Figure 3.1 and every step is described as follows. In section 3.2 the preprocessing steps needed to convert raw data into phase images are illustrated. In section 3.3, the scale-space framework is defined and the winding number is used as a tool to extract critical points in scale-space. Moreover, in this section a technique for the refinement of the position of the retrieved feature points up to sub-pixel location is discussed. Section 3.4 describes a methodology used to calculate velocity features and a scale selection scheme. Section 3.5 is dedicated to the multi-scale Helmholtz decomposition of vector fields. In sections 3.6, 3.7 the concept of covariant derivatives is introduced and the mathematical formulation of the proposed optic flow method is provided. Finally in section 3.8 and 3.9 the outcomes of the experiments carried out are presented and discussed.

3.2 Image data set and preprocessing

As already discussed in section 2.2, tagging is a noninvasive technique based on locally perturbing the magnetization of the cardiac tissue via radio frequency impulses. MR tags are artificial patterns, represented as a sinusoidal pattern on the MR images with the aim to improve the visualization of the deformation of tissue [179]. An example of a tagged heart image is displayed in Figure 3.2, column 1. In order to increase the number of tags in the image, Axel and Dougherty [14] spatially modulated the degree of magnetization in the cardiac tissue, whereas Osman et al. [126] proposed the so-called harmonic

phase (HARP) method, which converts MR images to phase images. In our experiments we apply a similar technique and we extract phase images by means of Gabor filters [64]. Such images allow to extract feature points such as maxima minima and saddles with high accuracy. A sine function has been applied for smoothing purposes to the calculated phase images with horizontal and vertical stripes. Later, these images have been combined in order to create a chessboard-like grid from which critical points have been retrieved (see Figure 3.2).

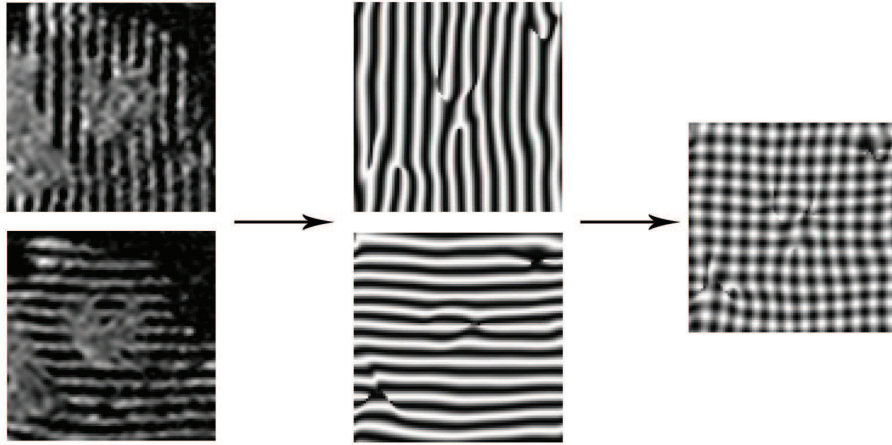


Figure 3.2: Column 1: Short axis views of a patient's left ventricle. Column 2. Sine-phase images. Column 3. Sum of sine-phase images. This sum of sine phase images serves as input in our algorithms and will be denoted by $f(\mathbf{x}, t)$ where $\mathbf{x} = (x, y) \in \mathbb{R}^2$ denotes position and $t > 0$ denotes time. Images are 86×86 pixels with pixel size of $1.2 \times 1.2 \text{ mm}^2$.

3.3 Extraction of critical points in scale space

Our visual system observes (objects in) an image simultaneously at multiple scales. The scale space theory allows to mimic this behavior. The Gaussian scale space representation $I : \mathbb{R}^2 \times \mathbb{R}^+$ of a 2-dimensional *static* image $\mathbf{x} \mapsto f(\mathbf{x}) \in L_2(\mathbb{R}^2)$ is defined by the spatial convolution with a Gaussian kernel

$$I(\mathbf{x}, s) = (f * \phi_s)(\mathbf{x}) ,$$

$$\text{with } \phi_s(\mathbf{x}) = \frac{1}{4\pi s} \exp\left(-\frac{\|\mathbf{x}\|^2}{4s}\right) , s > 0, \quad (3.2)$$

where $\mathbf{x} = (x, y) \in \mathbb{R}^2$ and where $s > 0$ represents the scale¹ of observation [79, 170, 107, 108, 94, 151, 54]. This procedure naturally extends to a multiple-scale representation of a *dynamic* image $(x, y, t) \mapsto f(x, y, t)$:

$$I(x, y, s, t) := (G_s * f(\cdot, \cdot, t))(x, y),$$

with $t, s > 0, \mathbf{x} = (x, y) \in \mathbb{R}^2$.

A convenient tool to extract and classify critical points at different scales is represented by the so-called topological number [146]. The topological number characterizes the local structure of a function by exploring the neighborhood of a certain point. For 2-dimensional functions the topological number is denoted as the *winding number* and represents the integrated change of the angle of the gradient when traversing a closed curve in a plane around the point. The winding number is always an integer multiple of 2π and its value classifies intrinsically the extracted critical point. The winding number is zero for regular points, it is $+2\pi$ for extrema, and -2π for saddle points.

3.3.1 Critical point position refinement

Due to signal discretization, the retrieved critical point location (for example computed by means of the winding number) most likely does not correspond to the real extremum or saddle point position (Figure 3.3). This problem can be solved by describing a fixed time frame image gradient $\nabla I(\cdot, s, t)$, with $s, t > 0$ fixed, in terms of Taylor series expansions to first order such that

$$\begin{aligned} \nabla I(\mathbf{x}_a, s, t) = & \\ & \begin{bmatrix} I_x(\mathbf{x}_e, s, t) + (x_a - x_e)I_{xx}(\mathbf{x}_e, s, t) + (y_a - y_e)I_{xy}(\mathbf{x}_e, s, t) \\ I_y(\mathbf{x}_e, s, t) + (x_a - x_e)I_{yx}(\mathbf{x}_e, s, t) + (y_a - y_e)I_{yy}(\mathbf{x}_e, s, t) \end{bmatrix} \end{aligned} \quad (3.3)$$

where $\mathbf{x}_a = (x_a, y_a)$ and $\mathbf{x}_e = (x_e, y_e)$ represent the true and the estimated critical point location respectively. At critical point positions the image gradient vanishes, therefore the left hand side (l.h.s.) of equation (3.3) vanishes, hence

$$\begin{aligned} \mathbf{x}_a = & \begin{bmatrix} x_a \\ y_a \end{bmatrix} = \\ & \begin{bmatrix} x_e \\ y_e \end{bmatrix} - \begin{bmatrix} I_{xx}(\mathbf{x}_e, s, t) & I_{xy}(\mathbf{x}_e, s, t) \\ I_{yx}(\mathbf{x}_e, s, t) & I_{yy}(\mathbf{x}_e, s, t) \end{bmatrix}^{-1} \begin{bmatrix} I_x(\mathbf{x}_e, s, t) \\ I_y(\mathbf{x}_e, s, t) \end{bmatrix} \end{aligned} \quad (3.4)$$

¹The Gaussian kernel is often defined as

$$\phi_\sigma(\mathbf{x}) = \frac{1}{2\pi\sigma^2} \exp\left(-\frac{\|\mathbf{x}\|^2}{2\sigma^2}\right).$$

The relationship between this definition of Gaussian function and the definition given in equation (3.2) is $s = \frac{1}{2}\sigma^2$.

Equation (3.4) provides position estimation at subpixel level and can be iterated until the desired accuracy has been reached. In the remainder of this article refined critical points positions will be abbreviated as follows $\mathbf{x} = \mathbf{x}_a$.

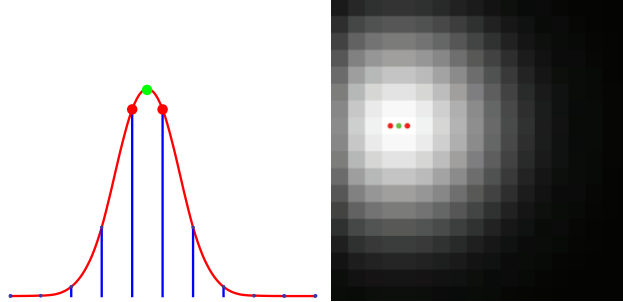


Figure 3.3: Critical point refinement. Left image: a continuum Gaussian signal in 1 dimension and the corresponding sampled signal. The sampled signal shows maxima at two nearby positions (points in red), which are at different locations from the real maximum (point in green). Right image: rasterized version of a 2-dimensional Gaussian signal. Red points are the retrieved maxima, whereas the green point is the true maximum obtained after the refinement.

3.4 Calculation of sparse velocity features

The chessboard like pattern displayed in Figure 3.2 is constructed from stripes that move along with the moving tissue, as a property of MR tags. We are interested in tracking critical points that occur at and between the tags crossings. Critical points move along with the tissue as part of the tags. Tag fading is an MR property and occurs due to finite relaxation time T_1 . This property, however, does not affect the vanishing image gradient (as long as the tag still exists) and therefore does not affect the critical point localization.

In tracking critical points over time we satisfy the equation

$$\nabla I(\mathbf{x}_s^q(t_k), s, t_k) = 0 \quad (3.5)$$

where ∇ denotes the *spatial* gradient and $I(\mathbf{x}_s^q, s, t_k)$ represents the intensity at position \mathbf{x}_s^q , scale s and time frame t_k , where $\mathbf{x}_s^q(t) = \mathbf{x}_s^q(0) + \int_0^t \tilde{\mathbf{v}}_q(\mathbf{x}_s^q(\tau)) d\tau$ such that $\frac{d}{dt} \mathbf{x}_s^q(t) = \tilde{\mathbf{v}}_q(\mathbf{x}_s^q(t))$ with $\mathbf{v}(\mathbf{x}(t), t) = \tilde{\mathbf{v}}(\mathbf{x}(t))$. Index $k = 1 \dots K$ corresponds to the time frame number and q represents the branch of a certain critical point. N_B represents the amount of branches/critical points per frame and K denote the amount of frames. Differentiating equation (3.5) with respect to time t_k

and applying the chain rule for the implicit functions yields

$$\left. \frac{d}{dt} [\nabla I(\mathbf{x}_s^q(t), s, t)] \right|_{t=t_k} = \begin{bmatrix} I_{xx}(\mathbf{x}_s^q(t_k), s, t_k) \tilde{u}_q(\mathbf{x}_s^q(t_k)) + I_{xy}(\mathbf{x}_s^q(t_k), s, t_k) \tilde{v}_q(\mathbf{x}_s^q(t_k)) + \\ + I_{xt}(\mathbf{x}_s^q(t_k), s, t_k) \\ I_{yx}(\mathbf{x}_s^q(t_k), s, t_k) \tilde{u}_q(\mathbf{x}_s^q(t_k)) + I_{yy}(\mathbf{x}_s^q(t_k), s, t_k) \tilde{v}_q(\mathbf{x}_s^q(t_k)) + \\ + I_{yt}(\mathbf{x}_s^q(t_k), s, t_k) \end{bmatrix} = 0 \quad (3.6)$$

where $\frac{d}{dt}$ is the total time derivative. In order to extract the critical point velocities, we can rewrite equation (3.6) as:

$$\begin{bmatrix} \tilde{u}(\mathbf{x}_s^q(t_k)) \\ \tilde{v}(\mathbf{x}_s^q(t_k)) \end{bmatrix} = \begin{bmatrix} u(\mathbf{x}_s^q(t_k), t_k) \\ v(\mathbf{x}_s^q(t_k), t_k) \end{bmatrix} = - (HI(\cdot, \cdot, t_k)(\mathbf{x}_s^q, s))^{-1} \frac{\partial (\nabla I(\mathbf{x}_s^q, s, t_k))^T}{\partial t_k} \quad (3.7)$$

where H represents the spatial Hessian matrix of image I . The scalars $\tilde{u}(\mathbf{x}_s^q(t_k))$ and $\tilde{v}(\mathbf{x}_s^q(t_k))$ are the horizontal and vertical components of a velocity vector at position \mathbf{x}_s^q at the time t_k at scale $s > 0$.

In the remainder of this chapter we will abbreviate the velocity vectors at the critical points as follows

$$\mathbf{d}_q^k := \begin{pmatrix} d_q^{k,1} \\ d_q^{k,2} \end{pmatrix} := \begin{pmatrix} \tilde{u}(\mathbf{x}_s^q(t_k)) \\ \tilde{v}(\mathbf{x}_s^q(t_k)) \end{pmatrix}. \quad (3.8)$$

In the subsequent section we will consider a scale selection scheme per critical point indexed by q and per time-frame $t > 0$.

3.4.1 Scale selection for features at fixed time frames

So far we assumed that velocities are retrieved at a certain scale without specifying the size of the basis function (Gaussian filter) applied at each critical point location. The choice of scale higher than zero may provide more robustness with respect to the noise due to smoothing related to the increase of scale. Moreover, the appropriate scale at different locations in the cardiac muscle may be different, since the heart exhibits different deformations in different regions (i.e stretching. compression).

In choosing the scale, we consider the strength of blobs moving in the image sequence. In this work the word "strength" is related to the spatial extend and intensity contrast of the blob. The stronger a blob is in scale space, the more vertical is its critical path and the higher is the scale of the corresponding annihilation point (top point), see Figure 3.5, left image. A top point (\mathbf{x}, s) is

a singular point in scale space where the gradient and the determinant of the spatial Hessian with respect to an image I vanish [99, 130], i.e.

$$\begin{aligned} \nabla I(\mathbf{x}, s, t) &= 0 \\ \text{and } \det HI(\mathbf{x}, s, t) &= I_{xx}(\mathbf{x}, s, t)I_{yy}(\mathbf{x}, s, t) - (I_{xy}(\mathbf{x}, s, t))^2 = 0 \end{aligned} \quad (3.9)$$

and as a result top points are the singular points where spatial extrema (where eigenvalues of the Hessian share the same sign) and spatial saddles merge (where eigenvalues of the Hessian have different signs).

On the other hand we need to avoid strong dislocation of spatial extrema in scale-space and instable parts of critical curves (see figure 3.4). Typically, the slope of the tangent vector along a critical branch in scale space provides a measure on the stability and dislocation. At scale 0 an extremal branch of a strong extremum (i.e. $s_q(t) \gg 0$) is nearly vertical, whereas at top-point scale $s_q^*(t)$ the slope is horizontal [56]).

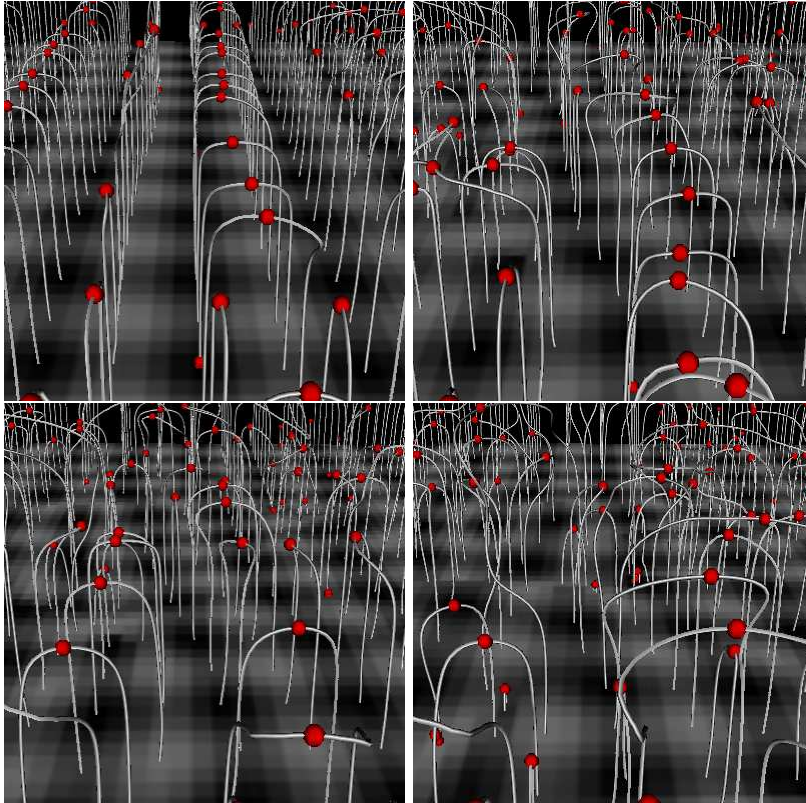


Figure 3.4: From left to right. From row 1 to row 2. Four subsequent frames of the heart chessboard representation illustrated together with the respective critical paths (white lines) and top points (red dots). The plots have been visualized using the software ScaleSpaceVis [92].

Figure 3.4 exhibits four subsequent frames of the heart represented together

with the critical paths in white lines. Due to the symmetry of the MRI tagging chessboard pattern, critical branches annihilate with different neighbors through the sequence. Top points show strong dislocation and have been discarded from our choice of features for this type of images. We choose therefore critical points with scale $s < s_q^*(t)$. Hence for each fixed time $t > 0$, we choose the highest scale s_q such that the slope (in scale-space) of the tangent vectors along the critical path is below a certain a priori angle ϑ with respect to the scale direction $(0, 0, 1)$. We propose the following scale selection per q -th critical branch:

$$s_q(t) := \max \left\{ s = s_{\min} e^{2\tau} \in [0, s_q^*(t)] \mid \text{for all } s' = s_{\min} e^{2\tau'} \in [0, s] \text{ we have } \arccos\left(\frac{\beta}{\sqrt{\left\|\frac{d}{d\tau}\mathbf{x}_s^q(t)\right|_{\tau=\tau'}\|^2 + \beta^2}}\right) < \vartheta \right\}. \quad (3.10)$$

where τ is the so-called *natural scale parameter*, a dimensionless parameter introduced by Florack et al. in [58]. The parameter τ can be any real number, even negative. In equation (3.10) s_{\min} is the scale for $\tau = 0$ and gives the resolution for which the width of the blurring kernel is of the same order of magnitude as the pixel size of the original image. The tangent vector along the critical curve in scale-space is given by

$$\frac{d}{d\tau}\mathbf{x}_s^q(t) = 2s \frac{d}{ds}\mathbf{x}_s^q(t) = -2s [HI(\mathbf{x}_s^q(t), s, t)]^{-1} \Delta \nabla I(\mathbf{x}_s^q(t), s, t),$$

as derived in [108, p.189], where ϑ is an a priori threshold angle (10 degrees in the experiments), and where β is a parameter with physical dimension [Length], see Figure 3.5, right image. In our experiments we set $\beta = (\Delta\tau)^{-1} \sqrt{(\Delta x)^2 + (\Delta y)^2}$, where $\Delta x, \Delta y, \Delta\tau$ denote step-sizes.

In this way the top point scale is discarded in the experiments (by setting $0 < \vartheta \ll \pi/2$), which avoids similar problems as with top points matching and symmetric structures [130] such as the chessboard like structure created by combining frames with horizontal and vertical tags.

3.5 Vector field decomposition

The behavior of the cardiac muscle is characterized by twistings and contractions, which can be studied independently by application of the so-called Helmholtz decomposition. In 1858 Helmholtz [167] showed that any vector field, with properties described below, can always be decomposed in *irrotational* and *solenoidal* components. Given a bounded domain $\Omega \subseteq \mathbb{R}^3$ and a smooth vector field \mathbf{v} , in our case the reconstructed cardiac motion field, $\mathbf{v} \in \mathbf{C}^0(\bar{\Omega})$ and

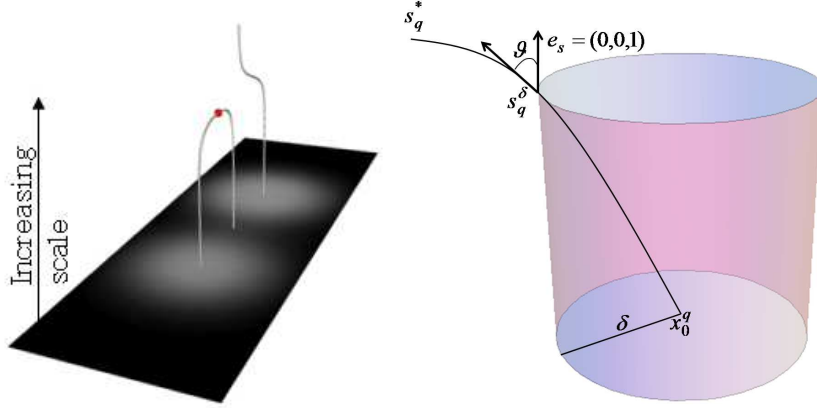


Figure 3.5: Left image: white lines represent critical paths in scale space (where we keep time t fixed) of certain blobs: $(0, 0, 1)$ direction is the scale direction. The red dot on the critical path is the so-called top-point, Eq. (3.9). Right image: Scale selection. Scale s_q^* denotes the top point scale. The highest scale s_q is chosen such that the slope (in scale-space) of the tangent vectors along the critical path is smaller than a certain angle ϑ . The corresponding spatial dislocation of the critical path is denoted by δ .

$\mathbf{v} \in \mathbf{C}^1(\Omega)$, where $\bar{\Omega} = \Omega \cup \partial\Omega$, functions Φ and $\mathbf{A} \in \mathbf{C}^1(\bar{\Omega})$ exist such that

$$\mathbf{v}(\mathbf{x}) = \nabla\Phi(\mathbf{x}) + \nabla \times \mathbf{A}(\mathbf{x}) \quad (3.11)$$

and

$$\nabla \cdot \mathbf{A}(\mathbf{x}) = 0 \quad (3.12)$$

where $\mathbf{x} = (x, y, z) \in \mathbb{R}^3$. In equation (3.11) functions Φ and \mathbf{A} are the so-called *scalar potential* and *vector potential*, whereas $\nabla\Phi(\mathbf{x})$ and $\nabla \times \mathbf{A}(\mathbf{x})$ represent the *irrotational* and *solenoidal* components of vector field \mathbf{v} . However in our cardiac MRI tagging application we consider $\Omega \subseteq \mathbb{R}^2$ and in \mathbb{R}^2 one does not have an outer product at hand and therefore we need the following definition.

Definition 1. Recall that the rotation of a vector field in 3D is in Euclidean coordinates expressed as

$$\text{rot } \mathbf{v} = \nabla \times \mathbf{v} = \begin{pmatrix} \partial_y v^3 - \partial_z v^2 \\ \partial_z v^1 - \partial_x v^3 \\ \partial_x v^2 - \partial_y v^1 \end{pmatrix} \quad (3.13)$$

with $\mathbf{v} = \{\tilde{v}^1, \tilde{v}^2, \tilde{v}^3\}$. In this article we define the rotation of a 2D-vector vector field in Euclidean coordinates as follows

$$\text{rot } \mathbf{v} := \partial_x v^2 - \partial_y v^1. \quad (3.14)$$

with $\mathbf{v} = \{\tilde{v}^1, \tilde{v}^2\}$ and we define the rotation of a scalar field in Euclidean coordinates by

$$\widetilde{\text{rot}} F := \begin{pmatrix} \partial_y F \\ -\partial_x F \end{pmatrix} \quad (3.15)$$

The theory of Helmholtz decomposition in 3D is extended to 2D by replacing the rotation (3.13) consistently by respectively (3.14) and (3.15). For example, the fundamental identity underlying 3D-Helmholtz decomposition is

$$\Delta \mathbf{v} = \text{grad div } \mathbf{v} - \text{rot rot } \mathbf{v} \quad (3.16)$$

where Δ indicates the Laplacian operator $\Delta = \nabla^2$. In 2D equation (3.16) becomes

$$\Delta \mathbf{v} = \text{grad div } \mathbf{v} - \widetilde{\text{rot}} \text{ rot } \mathbf{v} . \quad (3.17)$$

In order to obtain an explicit decomposition (3.22), we derive a solution to the Poisson equation in Ω [41] such that

$$\Delta \boldsymbol{\xi}(\mathbf{x}) = \mathbf{v}(\mathbf{x}) \quad (3.18)$$

by means of

$$\boldsymbol{\xi}(\mathbf{x}) = \int_{\Omega} G^{2D}(\mathbf{x} - \mathbf{x}') \mathbf{v}(\mathbf{x}') d\mathbf{x}' \quad (3.19)$$

where

$$G^{2D}(\mathbf{x} - \mathbf{x}') = \frac{1}{2\pi} \ln \|\mathbf{x} - \mathbf{x}'\| \quad (3.20)$$

is a so-called Green's function of the 2 variables Poisson equation. Moreover, $\boldsymbol{\xi}(\mathbf{x})$ satisfies the identity

$$\Delta \boldsymbol{\xi}(\mathbf{x}) = \nabla(\nabla \cdot \boldsymbol{\xi}(\mathbf{x})) - \widetilde{\text{rot}}(\text{rot } \boldsymbol{\xi}(\mathbf{x})) \quad (3.21)$$

therefore combining

$$\mathbf{v} = \Delta \boldsymbol{\xi} = \text{grad div } \boldsymbol{\xi} - \widetilde{\text{rot}} \text{ rot } \boldsymbol{\xi} = \text{grad } \Phi + \widetilde{\text{rot}} A \quad (3.22)$$

(the 2D equivalent of (3.11)), (3.18) and (3.21), we obtain

$$\Phi(\mathbf{x}) = \nabla \cdot \boldsymbol{\xi}(\mathbf{x}) \text{ and } A(\mathbf{x}) = -\text{rot } \boldsymbol{\xi}(\mathbf{x}). \quad (3.23)$$

However, the decomposition (3.22) is not unique, since if we replace $\boldsymbol{\xi} \mapsto \boldsymbol{\xi} + \mathbf{h}$ with \mathbf{h} a arbitrary harmonic vector field, we have $\Delta(\boldsymbol{\xi} + \mathbf{h}) = \Delta \boldsymbol{\xi} = \mathbf{v}$. The decomposition is unique if we prescribe the field to vanish at the boundary [47]. In order to do so, we subtract the harmonic infilling (see definition 2) from the original vector field. Hence

$$\begin{aligned} \tilde{\mathbf{v}} &= \mathbf{v}(\mathbf{x}) - \boldsymbol{\psi}(\mathbf{x}) = \\ &= \nabla \int_{\Omega} \nabla_{\mathbf{x}} \cdot G^{2D}(\mathbf{x} - \mathbf{x}') \tilde{\mathbf{v}}(\mathbf{x}') d\mathbf{x}' - \widetilde{\text{rot}} \int_{\Omega} \text{rot }_{\mathbf{x}} G^{2D}(\mathbf{x} - \mathbf{x}') \tilde{\mathbf{v}}(\mathbf{x}') d\mathbf{x}' \end{aligned} \quad (3.24)$$

where vector field $\tilde{\mathbf{v}}(\mathbf{x})$ vanishes at the boundaries, with $\boldsymbol{\psi} = (\mathbf{v}|_{\partial\Omega})_{\mathcal{H}}$ as the unique harmonic infilling.

Definition 2. *The Harmonic infilling $\psi = (\mathbf{v}|_{\partial\Omega})_{\mathcal{H}}$ of the field $\mathbf{v}|_{\partial\Omega}$ restricted to the boundary $\partial\Omega$ is by definition the unique solution of*

$$\begin{cases} \Delta\psi(\mathbf{x}) = 0 & \mathbf{x} \in \Omega \\ \psi|_{\partial\Omega} = \mathbf{v}|_{\partial\Omega}. \end{cases}$$

3.5.1 Multi-scale Helmholtz decomposition of the optical flow field

Instead of using standard derivatives in the Helmholtz decomposition (3.24), we can differentiate the involved Green's functions by regularized Gaussian derivatives, i.e. convolution with a derivative of a Gaussian kernel. In this procedure the kernel is affected by a diffusion, which depends on parameter $s = \frac{1}{2}\sigma^2$, the scale. This diffusion removes the singularity at the origin and, therefore, discretization artefacts. The first order Gaussian derivative (with respect to x) of the Green's function through the Fourier domain is:

$$\begin{aligned} \partial_x G_s^{2D}(\mathbf{x}) &= \\ \mathcal{F}^{-1}\left((\omega_1, \omega_2) \mapsto \frac{i\omega_1}{2\pi(\omega_1^2 + \omega_2^2)} \exp(-s(\omega_1^2 + \omega_2^2))\right)(\mathbf{x}) &= \\ \mathcal{F}^{-1}\left((\omega_1, \omega_2) \mapsto \frac{i\omega_1}{2\pi} \int_s^\infty \exp(-t(\omega_1^2 + \omega_2^2)) dt\right)(x, y) &= \\ \int_s^\infty \mathcal{F}^{-1}\left((\omega_1, \omega_2) \mapsto \frac{i\omega_1}{2\pi} \exp(-t(\omega_1^2 + \omega_2^2))\right)(x, y) dt &= \\ \int_s^\infty \frac{x \exp(-\frac{x^2+y^2}{4t})}{8\pi t^2} dt = \frac{x}{2\pi} \frac{1 - \exp(-\frac{x^2+y^2}{4s})}{x^2 + y^2} \end{aligned} \quad (3.25)$$

where ω_1 and ω_2 denote the two-dimensional frequency variables. The derivative of the Gaussian blurred Green's function with respect to y can be calculated using the same approach, hence

$$\partial_y G_s^{2D}(\mathbf{x}) = \frac{y}{2\pi} \frac{1 - \exp(-\frac{x^2+y^2}{4s})}{x^2 + y^2}, \quad \mathbf{x} = (x, y). \quad (3.26)$$

We notice that if the scale $s > 0$ tends to zero the diffused/blurred Green function derivatives tend to the ordinary derivatives

$$\begin{aligned} \lim_{s \rightarrow 0} \partial_x G_s^{2D}(\mathbf{x}) &= \frac{1}{2\pi} \frac{x}{x^2 + y^2} \\ \lim_{s \rightarrow 0} \partial_y G_s^{2D}(\mathbf{x}) &= \frac{1}{2\pi} \frac{y}{x^2 + y^2} \end{aligned} \quad (3.27)$$

where $\mathbf{x} \neq 0$. Figure 3.6 shows the graphs of the derivatives of the blurred Green's function $G_s^{2D}(\mathbf{x})$ for $s = 0$ and $s = 1$.

By combining (3.24), (3.25), (3.26) we obtain

$$\begin{aligned} \tilde{\mathbf{v}}_s := & \text{grad} (\partial_x G_s^{2D}(\mathbf{x}) * \tilde{v}^1 + \partial_y G_s^{2D}(\mathbf{x}) * \tilde{v}^2) - \\ & \widetilde{\text{rot}} (-\partial_y G_s^{2D}(\mathbf{x}) * \tilde{v}^1 + \partial_x G_s^{2D}(\mathbf{x}) * \tilde{v}^2) \end{aligned} \quad (3.28)$$

where $*$ is the symbol for the convolution operation. Hence, taking into account the contribution of the Harmonic infilling ψ , the vector field original vector field is given by

$$\mathbf{v}(\mathbf{x}) = \tilde{\mathbf{v}}_s + \psi(\mathbf{x}). \quad (3.29)$$

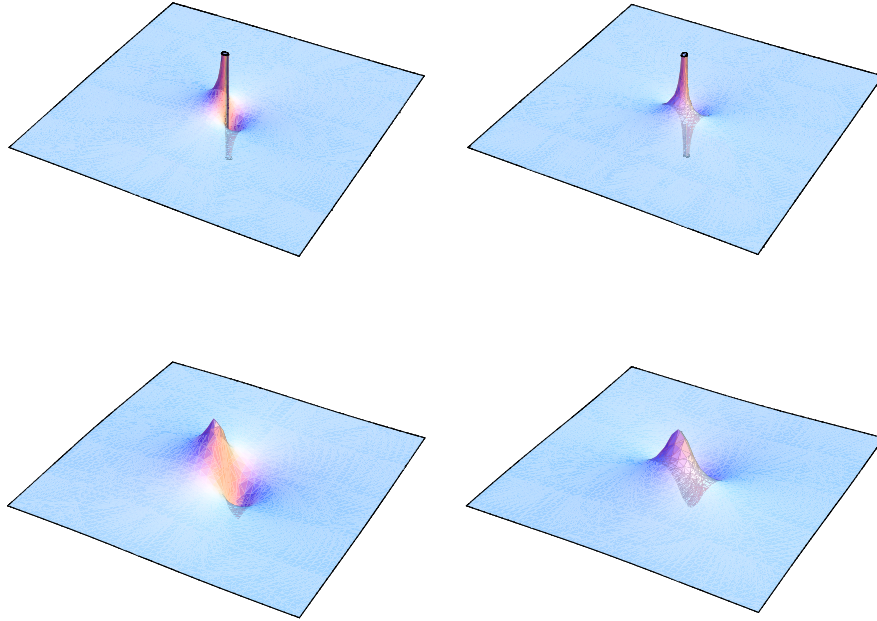


Figure 3.6: Plots of derivatives (3.25) of the 2-dimensional Green's function G_s^{2D} with respect to x and y . The two plots in row 1 display plots of the first order derivatives of the Green's function at scale $s = 0$. The two plots on row 2 show the case $s > 1$. At scale $s > 0$ the kernel no longer has a singularity at the origin and thereby one avoids sampling errors and grid artefacts.

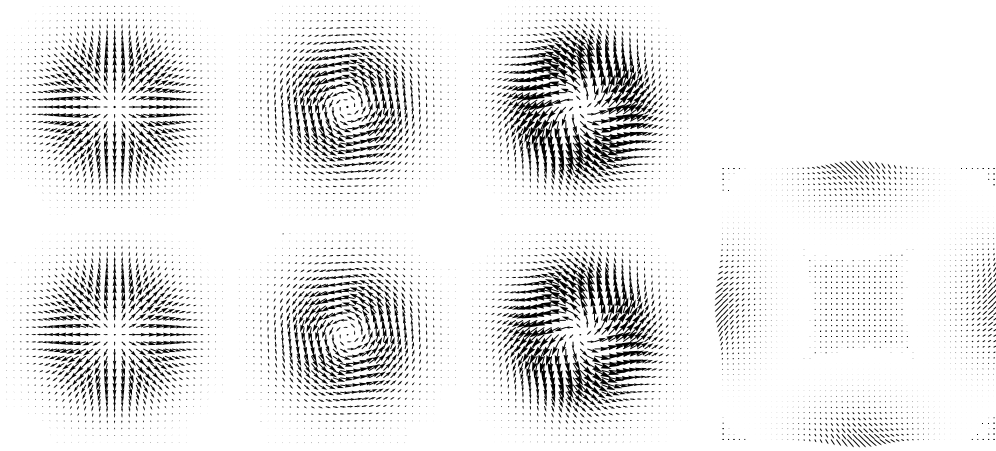


Figure 3.7: Helmholtz decomposition (top row) of the Phantom field \mathbf{v} , given by (3.30) and the output \mathbf{v}_s^{HD} of the Helmholtz decomposition algorithm (bottom row, cf. Eq. (3.29)) on domain $[-1, 1] \times [-1, 1]$. From left to right: the field, rotation-free part of the field, diverging-free part of the field. Most right image shows the harmonic infilling (definition 2), which we amplified by 10^4 since it is extremely small on $[-1, 1] \times [-1, 1]$.

3.5.2 Experiments on the decomposition of the vector field

In order to assess the accuracy of the extracted rotation-free and divergence-free components, as well as the accuracy of the recomposed vector field (the sum of the rotation free, divergence free and Harmonic infilling), we created a software phantom displaying a combination of divergence and rotation, see Figure 3.7 first row. The rotation-free and divergence-free part of the proposed phantom are given by

$$\mathbf{v}(x, y) = \underbrace{(x e_1 + y e_2) \frac{1}{4\pi\gamma} \exp\left(-\frac{x^2 + y^2}{4\gamma}\right)}_{\nabla\Phi_{ideal}} - \underbrace{(y e_1 - x e_2) \frac{1}{4\pi\gamma} \exp\left(-\frac{x^2 + y^2}{4\gamma}\right)}_{\widetilde{\text{rot}} A_{ideal}} \quad (3.30)$$

$(x, y) \in [-1, 1] \times [-1, 1]$, $\gamma = \frac{1}{50}$ (i.e. standard deviation of $\frac{1}{5}$) fixed where $e_1 = (1, 0)^T$ and $e_2 = (0, 1)^T$ represent a Cartesian orthonormal basis. The phantom has been furthermore blurred at scale $s = 1$. The decomposition and recomposition of the phantom's vector field has been carried out using equation (3.28) and (3.29) respectively. The computation has been performed at scale $s = 1$ (step size)² on an equidistant discrete 101×101 grid with spatial step size $\frac{1}{50}$ and has been evaluated using the average angular error (AAE) (3.31) given by

$$AAE = \frac{1}{(101)^2} \sum_{i,j=-50}^{50} \arccos\left(\frac{\mathbf{v}_s^{HD}(\mathbf{x}_{ij})}{\|\mathbf{v}_s^{HD}\|} \cdot \frac{\mathbf{v}(\mathbf{x}_{ij})}{\|\mathbf{v}(\mathbf{x}_{ij})\|}\right), \quad (3.31)$$

$\mathbf{x}_{ij} = \frac{1}{50}(i, j)$, where \mathbf{v}_s^{HD} represents the sum of the divergence free and rotation free part of the Helmholtz-decomposition algorithm and \mathbf{v} is ground truth. Tests on the artificial phantom showed errors $AAE = 0.35$ degrees for decomposing the vector field in rotation-free and divergence-free components, and errors $AAE = 0.4$ degrees for recomposing again the vector field.

In Figure 3.7 we show a comparison between the analytic phantom and its components (first row), and the recomposed vector field and its components (second row). A visual inspection and of the Figures in 3.7 confirms that the decomposition and recomposition of the phantom has been performed with high accuracy. The rotation free and divergence free components of the phantom (Figure 3.7 row 1) are hardly distinguishable from the rotation free, divergence free components and their sum (Figure 3.7 row 2) calculated with the equation (3.29).

3.6 A motivation for using covariant derivatives.

Usually one considers the derivative of a scalar-valued grey-value image (for example the components of a vector-field) $f : \Omega \rightarrow \mathbb{R}$ by means of a Gaussian derivative

$$\partial_x^{(s)} f = \partial_x(\phi_s * f) = (\partial_x \phi_s) * f$$

or by a finite difference (i.e. replace first order Gaussian by the discrete $[1, -1]$ -stencil filter). In this section we will refer to such derivatives as standard derivatives.

However, there is a short-coming to such an operator. It only compares the *difference* of local luminous intensities $\{f(\mathbf{x} + \mathbf{y}) \mid \|\mathbf{y}\| < 2\sigma\}$ with $f(\mathbf{x})$ and it does not take into account the actual *values* $f(\mathbf{x} + \mathbf{y})$ of local luminous intensities. Visual perception, however, does not work like this. Consider for example Figure 3.8. Gradients in dark areas are often perceived differently as gradients in light areas. This could be due to the fact that the visual system has some a priori gauge function that it expects due to typical surrounding (see Figure 3.9).

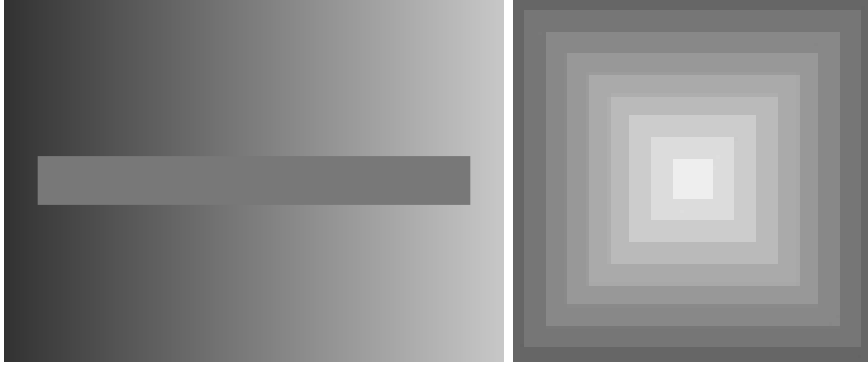


Figure 3.8: The left visual illusion illustrates that because of the surrounding grey-values a gradient is perceived in the rectangle, although the rectangle has constant brightness (so computation of an ordinary gradient in the rectangle yields zero). The right visual illusion illustrates the opposite dependence: due to different surrounding gradient structure the same brightness is perceived differently. Along the diagonal cross sections of the square the brightness is perceived higher than along the horizontal cross sections.

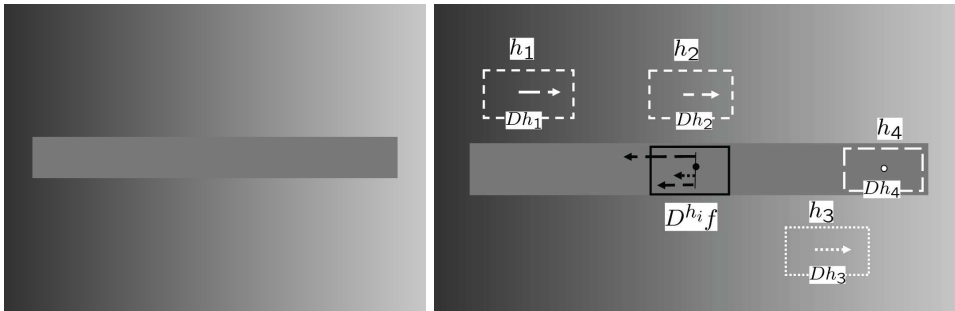


Figure 3.9: Gradient illusion. The rectangle in the middle of the gradient has constant brightness (function $f(x, y)$), which is not perceived as constant by the human visual system. Standard derivatives are not a suitable operator to interpret such an illusion, since the regular gradient vanishes within the rectangle. In the right image, gauge functions have been defined as the dashed boxes, with intensity i.e. $h_i(\tilde{x}, y) = \tilde{x} - x + h_i(\mathbf{0})$ for points within the box. The covariant derivatives expression gives $D^{h_i} f(x, y) = \partial_x f(x, y) - \frac{1}{h_i(x, y)} \partial_x h_i(x, y) f(x, y) = \mathbf{0} + \frac{1}{h_i(\mathbf{0})} (-1, 0)$. The origin of the coordinates has been put in the middle of the rectangles. Black vectors show direction and magnitude of covariant gradients whereas white vectors indicate direction and magnitude if gradients of standard derivatives. The index i has been used to distinguish different gauge functions.

In literature derivatives that take into account the influence of these surrounding areas, by means of gauge functions, are the covariant derivatives.

Here we provide the definition of a covariant derivative of a scalar function. This definition can be extended also to the covariant derivatives of a vector

field, since the components of a vector field are also scalar functions.

Given a scalar function $f : \Omega \rightarrow \mathbb{R}$ with respect to an a priori gauge function $h : \Omega \rightarrow \mathbb{R}$, the covariant derivative is defined by

$$D^h f(x, y) = \left\{ \partial_x f(x, y) - \frac{1}{h(x, y)} \partial_x h(x, y) f(x, y), \right. \\ \left. \partial_y f(x, y) - \frac{1}{h(x, y)} \partial_y h(x, y) f(x, y) \right\} \quad (3.32)$$

where $(x, y) \in \Omega \subset \mathbb{R}^2$ if $h(x, y) \neq 0$.

Note that the covariant derivative is invariant under scalar multiplication of the gauge function, so that

$$D^{\lambda h} f = D^{|h|} f = D^h f, \quad (3.33)$$

for all $h \neq 0$.

The derivative model proposed allows to interpret the Figure 3.9. The illustration shows an image gradient with a rectangle in the middle ($f(x, y)$), which has constant brightness. The pixel values inside the rectangle are not perceived as constant by our brain. This suggests that our visual system does not use standard derivatives to process this type of images, since the regular gradient vanishes within the rectangle. Moreover, the pixels on the left part of the rectangle seem brighter than the pixels in the right part of the rectangle. The covariant derivatives take into account these observation. In Figure 3.9 we define a gauge function as the portion of image in the white dashed box, i.e. $h_i(\tilde{x}, y) = \tilde{x} - x + h_i(\mathbf{0})$. By applying the equation (3.32) for points within the rectangle, we obtain

$$D^{h_i} f(x, y) = \mathbf{0} + \frac{1}{h_i(\mathbf{0})} (-1, 0).$$

The resulting expression is not constant and has opposite sign with respect to the input gauge function. Here we consistently put the origin of coordinate in the middle of the rectangles. Black vectors indicate covariant gradients whereas white vectors indicate regular gradients. The index i distinguishes between different gauge functions.

In our optic flow algorithm we are interested in dense motion reconstruction from a sparse set of velocity vectors. We use the covariant derivatives and the gauge functions in the smoothness term of an energy functional in order to influence the reconstruction of the velocity field. This is useful for instance in the case of very sparse velocity vectors. If the gauge field presents information in the areas, where the sparse velocity vectors are not present, this information will be taken into account during the reconstruction of the dense motion field.

3.6.1 Fibred Space and Covariant Derivatives

In this subsection we briefly explore the concept of a fiber bundle and we extract the formulation of covariant derivative (equation (3.32)) used in this work.

3.6.1.1 Fibred Space

In order to define the covariant derivative of a scalar function, such as an image, as a single component of a field, we have to define the scalar function in the fibred space (see [87]).

In differential geometry a fibred space (E, π, B) is defined by the total space E , a base space B , and a projection π , a mapping of the total space onto the base. Space B presents lower dimension with respect to total space E , that is, several points of E map to the same point of B . In such definition $\mathbb{R}^2 \times \mathbb{R}^2$ defines the total space E , the base B is defined in the image plane \mathbb{R}^2 and the projection $\pi : E \rightarrow B$ provides the location of each pixel in the image plane, such that $\pi(x, y, f^1(x, y), f^2(x, y)) = (x, y)$, where $f^1 \in \mathbb{R}^2$ and $f^2 \in \mathbb{R}^2$, provide the magnitude at position (x, y) of each of the two components of the vector field. Each point $p \in B$ corresponds to a fibre in E , that is, a collection of all points projected to the same point p by the mapping π (see Figure 3.10). A section associated to function f in a fibred space is instead a mapping $S_f : B \rightarrow E$ such that $S_f(x, y) = (x, y, f^1(x, y), f^2(x, y))$. The section selects one point out in each fibre. A grayscale image is a section in a fibred image space with $(\tilde{E} = \{x, y, f^1, f^2\} \in E | f^2 = 0\} \equiv \mathbb{R}^2 \times \mathbb{R}^+, \pi, B = \mathbb{R}^2)$.

3.6.1.2 Covariant Derivatives

In fibred spaces the slope of a section is measured by so-called *connections* or *covariant derivatives*, which are used in this model to compare pixel values from different fibres. A covariant derivative in a fibre space (E, π, B) is a mapping on E . Given $f(x, y) \in B$ and $h(x, y) \in B$ two scalar functions, the standard derivative of the product of these functions with respect to x is defined by the Leibnitz rule as $\partial_x(f h) = (\partial_x f)h + f(\partial_x h)$. We obtain a similar expression for the y direction. The Leibnitz rule of the derivative product can be extended also to the sections. Section S_f given by $S_f(x, y) = (x, y, f^1(x, y), f^2(x, y))$ can be represented as a linear combination² of a set of basis sections with a function

²The product of a function $\psi : \mathbb{R}^2 \rightarrow \mathbb{R}^+$ and a section $S_f : \mathbb{R}^2 \rightarrow \mathbb{R}^4$ is given by $(\psi \cdot S_f)(x, y) = (x, y, \psi(x, y)f(x, y))$.

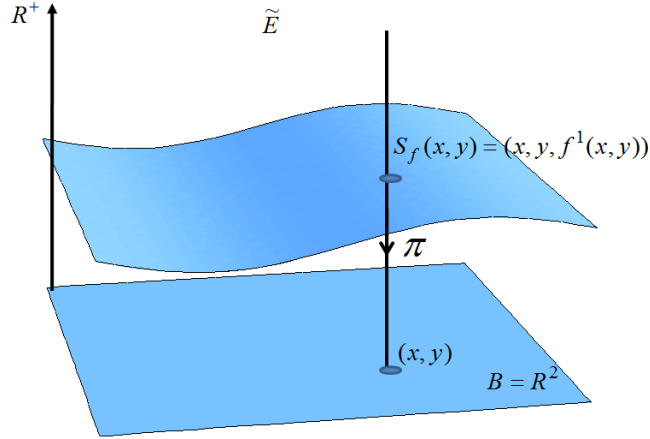


Figure 3.10: A visualization of the fibred space $\tilde{E} = \{x, y, f^1, f^2\} \in E | f^2 = 0\} \equiv \mathbb{R}^2 \times \mathbb{R}^+$, base $B = \mathbb{R}^2$, the mapping $\pi(x, y, f^1(x, y)) = (x, y)$, where x, y represent the Cartesian coordinates and $f^1(x, y)$ gives the pixel value at position x and y . $S_f(x, y) = (x, y, f^1(x, y))$ describes the section of function f . A grayscale image is a section in fibred image space.

$f(x, y)$, hence

$$S_f(x, y) = \sum_{i=1}^2 (f^i \cdot S_i)(x, y) \quad (3.34)$$

in which 2 is the dimension of a fiber. The basis section S_i is defined as $S_1(x, y) = \{x, y, 1, 0\}$ and $S_2(x, y) = \{x, y, 0, 1\}$. The derivative product with respect to x and y for equations (3.34) is

$$\begin{aligned} \nabla_x S_f(x, y) &= \nabla_x \sum_{i=1}^2 (f^i \cdot S_i)(x, y) = \\ & \sum_{i=1}^2 (\partial_x (f^i \cdot S_i)(x, y) + (f^i \cdot \nabla_x S_i)(x, y)) \\ \nabla_y S_f(x, y) &= \nabla_y \sum_{i=1}^2 (f^i \cdot S_i)(x, y) = \\ & \sum_{i=1}^2 (\partial_y (f^i \cdot S_i)(x, y) + (f^i \cdot \nabla_y S_i)(x, y)) \end{aligned} \quad (3.35)$$

where ∂_x and ∂_y are the derivative on a function, whereas ∇_x and ∇_y represent the derivative of a section with respect to x and y coordinates respectively. By definition, the derivative of a section is again a section representable by the basis sections [87], therefore

$$\begin{aligned}\nabla_x S_i(x, y) &= \sum_{j=1}^2 (A_{ix}^j \cdot S_j)(x, y) \\ \nabla_y S_i(x, y) &= \sum_{j=1}^2 (A_{iy}^j \cdot S_j)(x, y)\end{aligned}\tag{3.36}$$

where $A_{ix}^j(x, y)$ and $A_{iy}^j(x, y)$ are matrix valued functions defined in x and y (for vector fields with only one component, such as grayscale images, $A_{ix}^j(x, y) = A_x(x, y)$ and $A_{iy}^j(x, y) = A_y(x, y)$ correspond to functions). And combining the equations (3.35) and (3.36), we obtain

$$\begin{aligned}\nabla_x S_f(x, y) &= \sum_{i=1}^2 \partial_x f^i(x, y) + \sum_{j=1}^2 ((A_{jx}^i f^j) \cdot S_i)(x, y) \\ \nabla_y S_f(x, y) &= \sum_{i=1}^2 \partial_y f^i(x, y) + \sum_{j=1}^2 ((A_{jy}^i f^j) \cdot S_i)(x, y).\end{aligned}\tag{3.37}$$

Since sections can be defined with functions $f : \mathbb{R}^2 \rightarrow \mathbb{R}^2$

$$\begin{aligned}(D_x f^i)(x, y) &= \partial_x f^i(x, y) + \sum_{j=1}^2 (A_{jx}^i \cdot f^j)(x, y) \\ (D_y f^i)(x, y) &= \partial_y f^i(x, y) + \sum_{j=1}^2 (A_{jy}^i \cdot f^j)(x, y)\end{aligned}\tag{3.38}$$

and for $n = 1$ we have

$$\begin{aligned}(D_x f^1)(x, y) &= \partial_x f^1(x, y) + (A_x \cdot f^1)(x, y) \\ (D_y f^1)(x, y) &= \partial_y f^1(x, y) + (A_y \cdot f^1)(x, y)\end{aligned}\tag{3.39}$$

The expressions $D_x = \partial_x + A_x(x, y)$ and $D_y = \partial_y + A_y(x, y)$ represent the so-called *covariant derivatives* for a function with respect to x and y respectively. Given a function $h : \Omega \rightarrow \mathbb{R}$, by definition (see [87]), we have that any section given by $S(x, y) = (x, y, h(x, y))$ can be considered constant in the covariant sense with respect to the chosen $A_x(x, y)$ and $A_y(x, y)$, where the term "constant" means

$$\begin{aligned}D_x h(x, y) &= \partial_x h(x, y) + (A_x \cdot h)(x, y) = 0 \\ D_y h(x, y) &= \partial_y h(x, y) + (A_y \cdot h)(x, y) = 0\end{aligned}\tag{3.40}$$

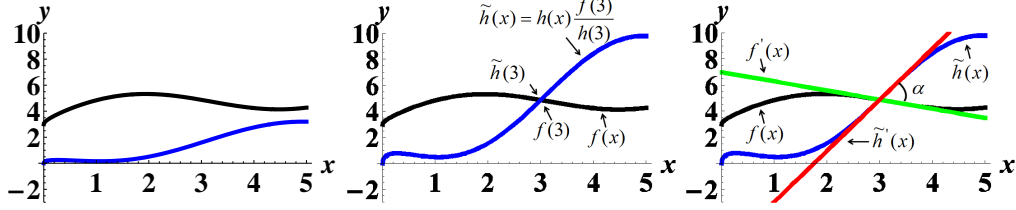


Figure 3.11: Covariant derivative: geometrical interpretation. Given functions $f : \mathbb{R} \rightarrow \mathbb{R}$ and $h : \mathbb{R} \rightarrow \mathbb{R}$, left image, we want to calculate $D^{h(x)} f(x) = f'(x) - \frac{h'(x)}{h(x)f(x)}$ at point $x = 3$. Therefore, we scale the gauge function h such that its graph contains $(3, f(3))$, hence $\tilde{h}(x) = h(x) \frac{f(3)}{h(3)}$, central image. Then we calculate the difference of the slopes of $f(x)$ and $\tilde{h}(x)$ at $x = 3$, right image.

hence,

$$\begin{aligned} A_x(x, y) &= -\frac{\partial_x h(x, y)}{h(x, y)} \\ A_y(x, y) &= -\frac{\partial_y h(x, y)}{h(x, y)} \end{aligned} \quad (3.41)$$

Therefore, applying the result of equation (3.41) to equation (3.39), a covariant derivative of a function f^1 with respect to a function h is given by

$$\begin{aligned} D_x^{h(x,y)} f^1(x, y) &= \partial_x f^1(x, y) - f^1(x, y) \frac{\partial_x h(x, y)}{h(x, y)} \\ D_y^{h(x,y)} f^1(x, y) &= \partial_y f^1(x, y) - f^1(x, y) \frac{\partial_y h(x, y)}{h(x, y)} \end{aligned} \quad (3.42)$$

If we suppose $f : \mathbb{R} \rightarrow \mathbb{R}$ and $h : \mathbb{R} \rightarrow \mathbb{R}$, the covariant derivative can be geometrically interpreted as the difference between the slope of function $f(x)$ and the slope of a gauge function h scaled with respect to function $f(x)$, see Figure 3.11.

A more rigorous mathematical definition provided by Dr Remco Duits have been reported in the appendix (A.1).

3.6.1.3 Interpolation between conventional derivatives and covariant derivatives

In this section we briefly explain that a monotonic transformation on the components of the gauge field takes care of the interpolation between standard derivatives and covariant derivatives. For the sake of illustration we restrict ourselves to the scalar valued case (with positive gauge function $h : \Omega \rightarrow \mathbb{R}^+$)

as the vector valued case follows by applying everything on the two separate components. By applying a monotonic transformation $h \mapsto h^\eta$ on the gauge function we obtain the following covariant derivative

$$\begin{aligned} D^{h^\eta(x,y)} f(x, y) &= Df(x, y) - D(\log h^\eta(x, y))f(x, y) = \\ &= Df(x, y) - \eta(D \log h(x, y))f(x, y) . \end{aligned} \tag{3.43}$$

If $\eta = 0$ the expression (3.43) provides a conventional derivative, whereas the case $\eta = 1$ yields a covariant derivative with respect to gauge function $h(x, y)$.

On the one hand we want to preserve the influence of the gauge field (initial guess) $h(x, y)$. On the other hand outliers in the magnitude of the gauge field $h(x, y)$ get too much influence in the final reconstruction if $\eta \geq 1$. So we observe a trade-off situation for the choice of η in our application. Experiments with different η will be discussed in section 3.8, Figure 3.14.

3.7 Feature based optic flow equation with covariant derivatives and Helmholtz decomposition

In image analysis gauge functions and covariant derivatives have been previously introduced by T. Georgiev [66] in an Adobe Photoshop inpainting problem and subsequently have been studied by [21, 83] for image and vector field reconstruction.

In this work we extrapolate dense motion through the regularization of the optic flow equation by means of covariant derivatives and gauge functions and taking into account the decomposition of the motion field in the divergence-free and rotation-free components. The gauge field imposes an a priori balance between velocity magnitude and velocity field changes, and thereby it is supposed to be close to the velocity field that we would like to reconstruct from a sparse set of features. There are several options in choosing the gauge field. In this work we choose gauge fields as motion fields obtained from regularization reconstruction with standard derivatives (see equation (2.10)) and then we carry out a regularization reconstruction using covariant derivatives (recall the algorithm overview in Figure 3.1). The latter step is then to be considered as a refinement of the first.

In chapter 2 we worked with previous time frame as gauge field. In this chapter we instead employ current time frame as gauge field. Experiments have shown to provide an improvement in the velocity field reconstruction for this latest choice of gauge field. This is not surprising as the images examined in the experiments display sudden transitions over time.

We aim to retrieve the velocity field \mathbf{v} at time-step k , by minimizing the energy functional

$$\begin{aligned}
 \mathcal{E}^{\lambda, \mathbf{h}^k, \mathbf{d}^k}(\mathbf{v}^k) &= \\
 \mathcal{E}_{reg}^{\mathbf{h}^k}(\mathbf{v}^k) + \mathcal{E}_{data}^{\mathbf{d}^k}(\mathbf{v}^k) &= \\
 \sum_{q=1}^{N_B} w_q^k \sum_{j=1}^2 |(\phi_{s_q} * v^{kj})(\mathbf{x}_q) - d_q^{k,j}|^2 + \lambda \int_{\Omega} \sum_{i=1}^2 \sum_{j=1}^2 |D_{x^i}^{h^{k,j}} v^{k,j}(\mathbf{x})|^2 d\mathbf{x}
 \end{aligned} \tag{3.44}$$

where $w_q^k \in \mathbb{R}^+$ is a weighting factor, the parameter $\lambda > 0$ provides balance between regularization part ($\mathcal{E}_{reg}^{\mathbf{h}^k}(\mathbf{v}^k)$) and the data term ($\mathcal{E}_{data}^{\mathbf{d}^k}(\mathbf{v}^k)$), index k indicates the time frame and q enumerates the extremal branches. Index $j \in \{1, 2\}$ indicates the vertical and horizontal component of the field and $x^i \in \{x^1 = x, x^2 = y\}$. Moreover,

$$\phi_k^q(\mathbf{x}) := \phi_{s_q}(\mathbf{x} - \mathbf{x}_q) \tag{3.45}$$

denotes the Gaussian kernel (3.2) centered around \mathbf{x}_q with scale $s_q > 0$, recall Figure 3.5, and where the sparse velocity components $d_q^{k,j}$, Eq. (3.8), are derived by solving Eq. (3.7).

Minimization of (3.44) has been carried out by solving the Euler Lagrange equations and the resulting expression has been discretized by using B-splines. A solution to this minimization problem has been calculated by Dr Remco Duits and has been reported in the appendix (A.2).

In order to investigate and reconstruct separately the rotation-free and divergence-free components of a vector field, the multi-scale Helmholtz decomposition has been furthermore included in equation (3.44). To this end we also decompose the sparse velocities into the divergence-free and rotation-free components. Namely, we reconstruct the velocity field by a regularization with standard derivatives at very small $0 < \lambda \ll 1$, to obtain a regularized velocity field that (nearly) satisfies the hard constraints (as $0 < \lambda \ll 1$). Then we apply a multi-scale Helmholtz decomposition on this field and we extract the divergence-free part and rotation-free part vectors at the position of interest \mathbf{x}_q and scale of interest s_q .

Hence, in order to calculate a dense motion field, we minimize the following energy forms

$$\begin{aligned}
& \mathcal{E}_{\text{divfree}}^{\lambda, \mathbf{h}^k, \mathbf{d}^k}(\mathbf{v}^k) = \\
& \sum_{q=1}^{N_B} w_q^k \sum_{j=1}^2 |(\phi_k^q, v^{k,j,\text{divfree}})_{\mathbb{L}_2(\Omega)} - d_q^{k,j,\text{divfree}}|^2 + \\
& \lambda_1 \int_{\Omega} \sum_{i=1}^2 \sum_{j=1}^2 |D_{x^i}^{h^{k,j,\text{divfree}}} v^{k,j,\text{divfree}}(\mathbf{x})|^2 \, d\mathbf{x} \\
& \mathcal{E}_{\text{rotfree}}^{\lambda, \mathbf{h}^k, \mathbf{d}^k}(\mathbf{v}^k) = \\
& \sum_{q=1}^{N_B} w_q^k \sum_{j=1}^2 |(\phi_k^q, v^{k,j,\text{rotfree}})_{\mathbb{L}_2(\Omega)} - d_q^{k,j,\text{rotfree}}|^2 + \\
& \lambda_2 \int_{\Omega} \sum_{i=1}^2 \sum_{j=1}^2 |D_{x^i}^{h^{k,j,\text{rotfree}}} v^{k,j,\text{rotfree}}(\mathbf{x})|^2 \, d\mathbf{x}
\end{aligned} \tag{3.46}$$

Finally we add up the outcomes of the minimized equation (3.46), such that

$$\mathbf{v}^k(\mathbf{x}) = \mathbf{v}^{k,\text{divfree}}(\mathbf{x}) + \mathbf{v}^{k,\text{rotfree}}(\mathbf{x}) \tag{3.47}$$

3.8 Experiments

In order to assess the accuracy of the proposed optic flow method depicted in Figure 3.1, we reconstruct/interpolate the motion fields of two different phantoms from which we know the ground truth. Phantom one is a sequence consisting of 19 time-frames with size 99×99 pixels of purely contracting and expanding patterns (Figure 3.12, column 2), whereas phantom 2 consists of 13 frames of 93×93 pixels in size and displays non-rigid rotation (Figure 3.12, column 4). Equations for phantom 1 have been provided in section 2.6, whereas a detailed description of phantom 2 has been given in section 5.2. The motion vanish in both phantoms at the boundaries. Extraction of the motion field has been carried out at several spatial scales $s = \{1, 1.22, 1.48, 1.81, 2.21, 2.69, 3.28, 4.\}$ with time scale 1.

Since our approach consists of separate reconstruction of the divergence-free and rotation-free part we index our parameters accordingly. For example λ_1 controls the degree of smoothness in the dense flow field reconstruction of the rotation-free part and η_1 denotes the interpolation parameter between covariant and standard derivatives of the dense flow field reconstruction of the rotation-free part. The corresponding parameters for the divergence-free component are λ_2 and η_2 .

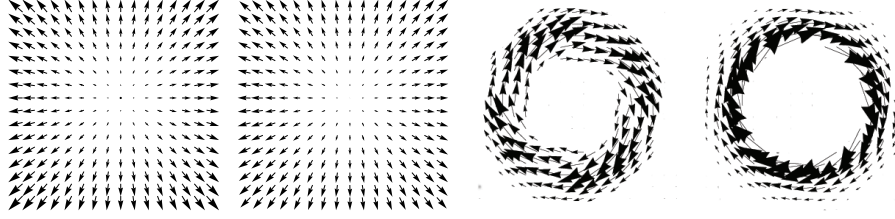


Figure 3.12: Phantoms and reconstructed vector fields. Larger arrows and arrow heads are related to larger flows. In these plots the arrow's length has been amplified 15 times. Column 1 and 2 display frame 5 of the expanding and contracting phantom: ground truth (column 1) and reconstructed vector field using the proposed algorithm (column 2). Column 3 and 4 display frame 3 of the rotating phantom: ground truth (column 3) and reconstructed vector field using the proposed algorithm (column 4).

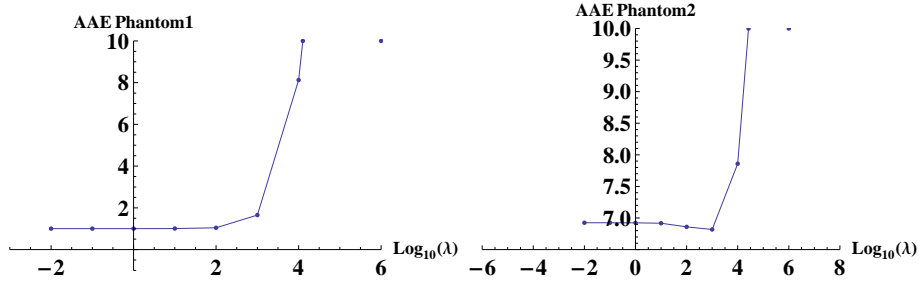


Figure 3.13: Performance of velocity field reconstruction method based on covariant derivatives and Helmholtz decomposition using different values for the smoothing parameter λ (expressed in logarithmic scale). The experiments have been carried out with fixed $\lambda_2 = 10^2$ for phantom 1 and $\lambda_1 = 10^2$ for phantom 2, and we vary parameter λ_1 for phantom 1 and λ_2 for phantom 2 according to a predefined range, such that $\lambda = \{10^{-2}, 10^{-1}, 1, 10, 100, 10^3, 10^4, 10^5, 10^6\}$. Left plot displays AAE behavior for phantom 1. Best performance $AAE = 0.97^\circ \pm 0.62^\circ$ for $\lambda_1 = 10^{-2}$ ($\log_{10} \lambda_1 = -2$). Right plot shows AAE behavior for phantom 2. Best results $AAE = 6.68^\circ \pm 9.48^\circ$ are achieved for $\lambda_2 = 10^3$ ($\log_{10} \lambda_2 = 3$).

Increasing the value of $\lambda > 0$ increases the smoothness of the reconstructed motion field. We choose λ such that the AAE and the L2 norm error of our phantoms with ground truth is minimized, where we set a range of values defined beforehand such as

$$\lambda = \{10^{-2}, 10^{-1}, 1, 10, 100, 10^3, 10^4, 10^5, 10^6\}.$$

The reconstruction method based on conventional derivatives showed best results at $\lambda = 10^{-2}$ and $\lambda = 1$ for the phantom 1 and phantom 2 respectively. The reconstruction method based on covariant derivative performed best at $\lambda = 10^2$ and $\lambda = 10$ for phantom 1 and phantom 2 respectively.

In case of reconstruction based on covariant derivatives and Helmholtz decomposition, we assign a fixed component $\lambda_2 = 10^2$ and $\lambda_1 = 10^2$ for phantom 1

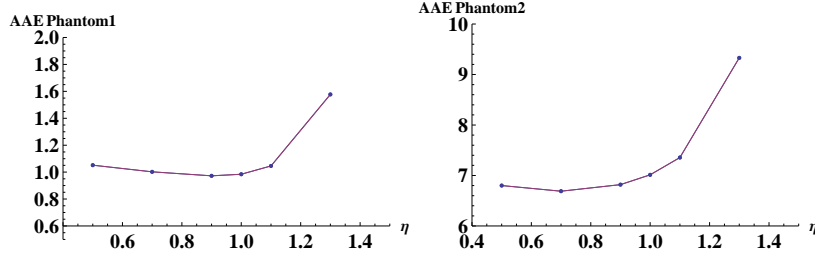


Figure 3.14: AAE behavior for different values of parameter η for the reconstruction method based on both covariant derivatives and Helmholtz decomposition. Parameter η takes into account the influence of the gauge field, recall subsection 3.6.1.3. In the experiments we keep fixed $\eta_2 = 0.5$ for phantom 1 and $\eta_1 = 0.5$ for phantom 2, and we vary parameter η_1 for phantom 1 and η_2 for phantom 2 according to a predefined range $\eta = \{0.5, 0.7, 0.9, 1., 1.1, 1.3\}$. Left plot shows AAE behavior for phantom 1. Best performance $AAE = 0.97^\circ \pm 0.62^\circ$ is obtained for $\eta_1 = 0.9$. Right plot shows AAE behavior for phantom 2. Best result $AAE = 6.68^\circ \pm 9.48^\circ$ is achieved for $\eta_2 = 0.7$.

and phantom 2 respectively and we choose the other λ component from the already defined range. In Figure 3.13 we displayed the AAE behavior for phantom 1 and 2 using the proposed technique imposing different values to λ_1 for phantom 1 and to λ_2 for phantom 2. Here the horizontal axis is expressed in a logarithmic scale with base 10. Best performance is achieved at $\lambda_1 = 10^{-2}$ ($\log_{10} \lambda_1 = -2$) and at $\lambda_2 = 10^3$ ($\log_{10} \lambda_2 = 3$) for phantom 1 and phantom 2 respectively.

Once the choice of the λ_i parameter is established, we investigate parameter η_i , $i = 1, 2$ which takes into account the influence of the gauge field in the velocity field reconstruction, recall subsection 3.6.1.3.

In the experiments we impose a gauge field equal to the outcome of the optic flow method based on conventional derivatives time frame k to reconstruct the motion field at time k (Figure 3.1). This is only one of the possible gauge field choices. Again we select parameter η from a range of a values $\eta = \{0.5, 0.7, 0.9, 1., 1.1, 1.3\}$ such that AAE is minimized. The reconstruction method based on covariant derivatives achieved best results for $\eta = 0.7$ and $\eta = 0.9$ for phantom 1 and 2 respectively. In case of the reconstruction method based on covariant derivative and Helmholtz decomposition we assign a fixed η , $\eta_2 = 0.5$ and $\eta_1 = 0.5$ for phantom 1 and 2 respectively, and we choose the other η_i from the defined range. In Figure 3.14 we display the behavior of AAE for phantom 1 and 2 for different values of η . The proposed reconstruction method provides best performance for $\eta_1 = 0.9$ and $\eta_2 = 0.7$ for phantom 1 and 2 respectively.

In Table 3.1 we display the performance of the optic flow method, where the smoothness component has been described in terms of standard derivatives,

covariant derivatives, and covariant derivatives combined with Helmholtz decomposition. In the assessment the error measure is based on the average angular error (AAE) [20], expressed in degrees, the L2 norm and their corresponding standard deviation. Algorithm evaluation has been performed on 3 subsequent frames for phantom 1 and phantom 2. A comparison with similar optic flow techniques, that do not take into account covariant derivatives and Helmholtz decomposition, shows that the proposed algorithm provides the most accurate reconstruction reaching AAE= 0.97 ± 0.62 degrees and L2 norm error of $3.3 \times 10^{-2} \pm 0.03$ for phantom 1 and AAE= 6.68 ± 9.48 degrees and L2 norm error of 0.16 ± 0.24 for phantom 2. The error measurements outcomes are averaged over the 3 investigated frames.

Figure 3.12 illustrates one frame of the retrieved motion fields for phantom 1 (column 1) and phantom 2 (column 3) and their ground truths in columns 2 and 4 for phantom 1 and 2 respectively. In the plot larger arrows and arrow heads are related to larger flows.

Reconstruction Methodology	Error Measurements Phantom 1		Error Measurements Phantom 2	
	AAE	L2 Norm	AAE	L2 Norm
Conventional Derivatives	$1.26^\circ \pm 1.11^\circ$	$4.2 \times 10^{-2} \pm 0.04$	$8.05^\circ \pm 9.09^\circ$	0.21 ± 0.26
Covariant Derivatives	$1.20^\circ \pm 1.01^\circ$	$3.6 \times 10^{-2} \pm 0.03$	$7.30^\circ \pm 9.81^\circ$	0.19 ± 0.25
Helmholtz Dec. and Covariant Derivatives	$0.97^\circ \pm 0.62^\circ$	$3.3 \times 10^{-2} \pm 0.03$	$6.68^\circ \pm 9.48^\circ$	0.16 ± 0.24

Table 3.1: Performance of the proposed optic flow method using different reconstruction modalities. In the experiments the Average Angular Error (AAE), is expressed in degrees, L2 norm and their corresponding standard deviation have been used as error measure. The measurements are averaged over the investigated 3 frames. Best performances are obtained by the Helmholtz Decomposition and Covariant Derivative reconstruction method, AAE= $0.97^\circ \pm 0.62^\circ$ and L2= $3.3 \times 10^{-2} \pm 0.03$ for phantom 1, and AAE= $6.68^\circ \pm 9.48^\circ$ and L2= 0.16 ± 0.24 for phantom 2.

Divergence-free and rotation-free parts of the vector field may be employed to reveal and quantify abnormal deformation in the tissue. In the following experiments we compare the behavior of motion fields extracted from a healthy volunteer and from a patient, whose heart displays infarcted areas as indicated in Figure 3.17. Acquisition of the heart images has been performed during the systolic phase; we assess 11 frames with resolution of 86×86 pixels and pixel size of $1.2 \times 1.2 \text{ mm}^2$. In these images the temporal resolution is roughly 2×10^{-2} seconds and with thickness of 8 mm . In Figures 3.15 and 3.16 we show the sampled motion field (column 1), rotation-free (column 2) and divergence-free (column 3) parts of the healthy heart case and the diseased case respectively. By means of our Helmholtz decomposition we observe that at the beginning of systole, the healthy heart exhibits a strong rotation (row 1, column 3) and little contraction (row 1, column 2). Halfway the systolic phase, the contribution of rotation-free parts becomes comparable to the contribution of the divergence-free part, that is, vectors inside the cardiac walls present similar length (row 2, column 2 and 3). At the end of systole, contraction becomes more relevant

(row 3, column 2), whereas rotation is almost absent (row 3, column 3). In the investigated diseased case, the heart exerts modest rotation through the whole sequence (row 1,2,3, column 3), leaving contraction as the almost only contribution to the heart beat (row 1,2,3 column 2).

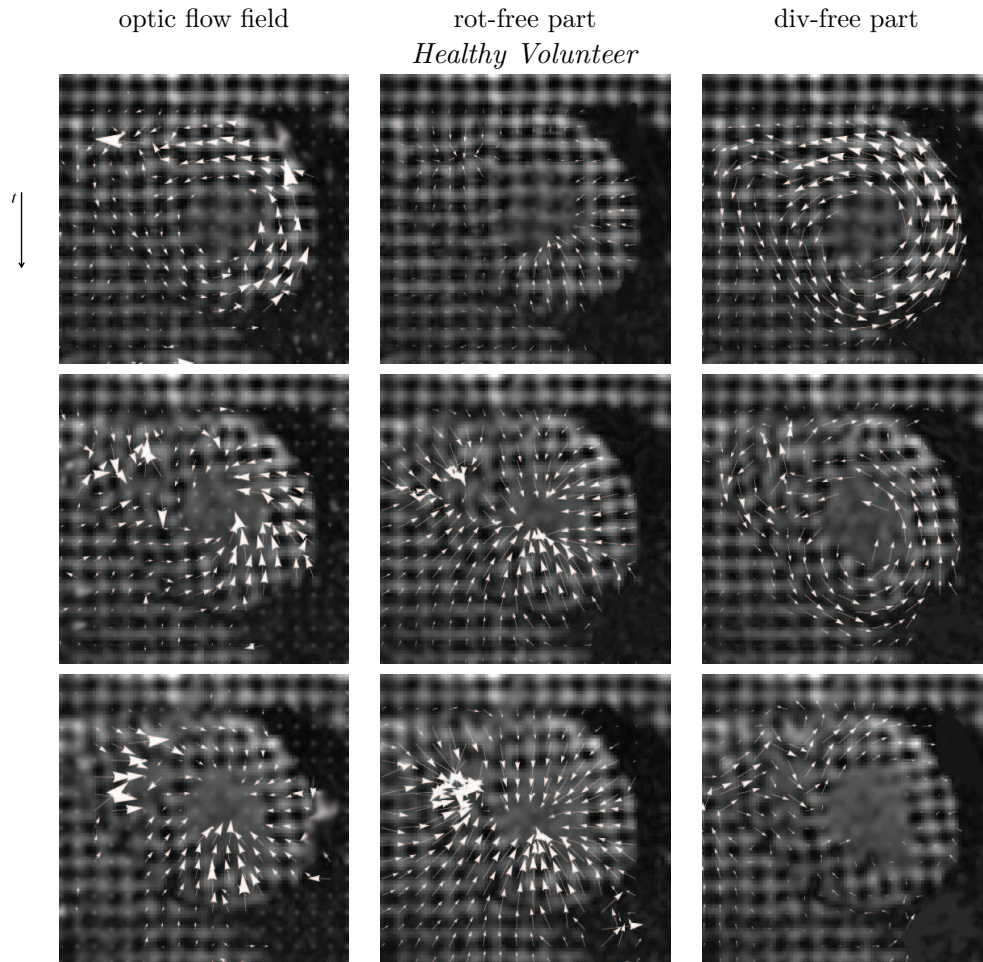


Figure 3.15: Cardiac motion field behavior for a healthy volunteer. We assess frame 3, 6 and 8 of a sequence of 11 frames displaying the cardiac muscle during systole. Column 1 shows the extracted motion fields, column 2 shows the rotation-free part, whereas column 3 shows the divergence-free part.

3.9 Discussion and Conclusion

We have introduced a new approach to estimate cardiac motion by means of gauge fields and Helmholtz decomposition, and thereby we have provided a tool to explore heart behavior.

The proposed optic flow technique contains regularization components described in terms of covariant derivatives, $\partial_{x^i}^{h^j} = \partial_{x^i} v^j - \frac{\partial_{x^i} h^j}{h^j} v^j$, where $\mathbf{v} = (v^1, v^2)^T$ and $\mathbf{h} = (h^1, h^2)^T$ are the unknown vector field and gauge field respectively with coordinates $\{x^1, x^2\} = \{x, y\}$. Gauge fields influence the regularization of the flow field reconstruction (see section 3.6) and in the energy minimization process they typically provide an a priori balance between magnitude (h^j) and spatial variations of velocities ($\partial_{x^i} h^j$). In this new approach the smoothness term does not penalize for changes from an imposed global assumption such as isotropic or anisotropic smoothness, like in many methods in the literature, but rather penalizes for deviations from a predefined motion model: in our case the gauge field. Furthermore, we include a fast multi-scale Helmholtz decomposition with the aim to reconstruct the divergence-free and rotation-free parts of the vector field separately.

We have tested the method with two different phantoms and the extracted motion fields have been compared with the outcomes of similar techniques, for which the smoothness component was expressed in terms of conventional derivatives and covariant derivatives only. The proposed approach provided the best performance and shows the advantage of both using covariant derivatives and using Helmholtz decomposition. Besides improving the quality of reconstruction, Helmholtz decomposition is used as a tool to study cardiac behavior, since vector field decomposition allows to analyze cardiac contraction and cardiac rotation independently.

Finally, we have applied our method on real tagged MR images displaying the left ventricle of a healthy volunteer and a patient. Qualitative results illustrate the reliability of the estimated motion field.

Future work and further improvements

In the algorithm we use gauge fields obtained from the outcomes of optic flow equations based on standard derivatives. This is just one of the possible choices. Gauge fields could also be deformed according to criteria that specifically reflect the heart behavior. Finally, the assessment has been carried out on two real data-sets. It would be interesting to apply the proposed technique on a larger population of images acquired from different volunteers and patients, with the aim to extract parameters that distinguishes cardiac healthy behavior from the presence of diseases.

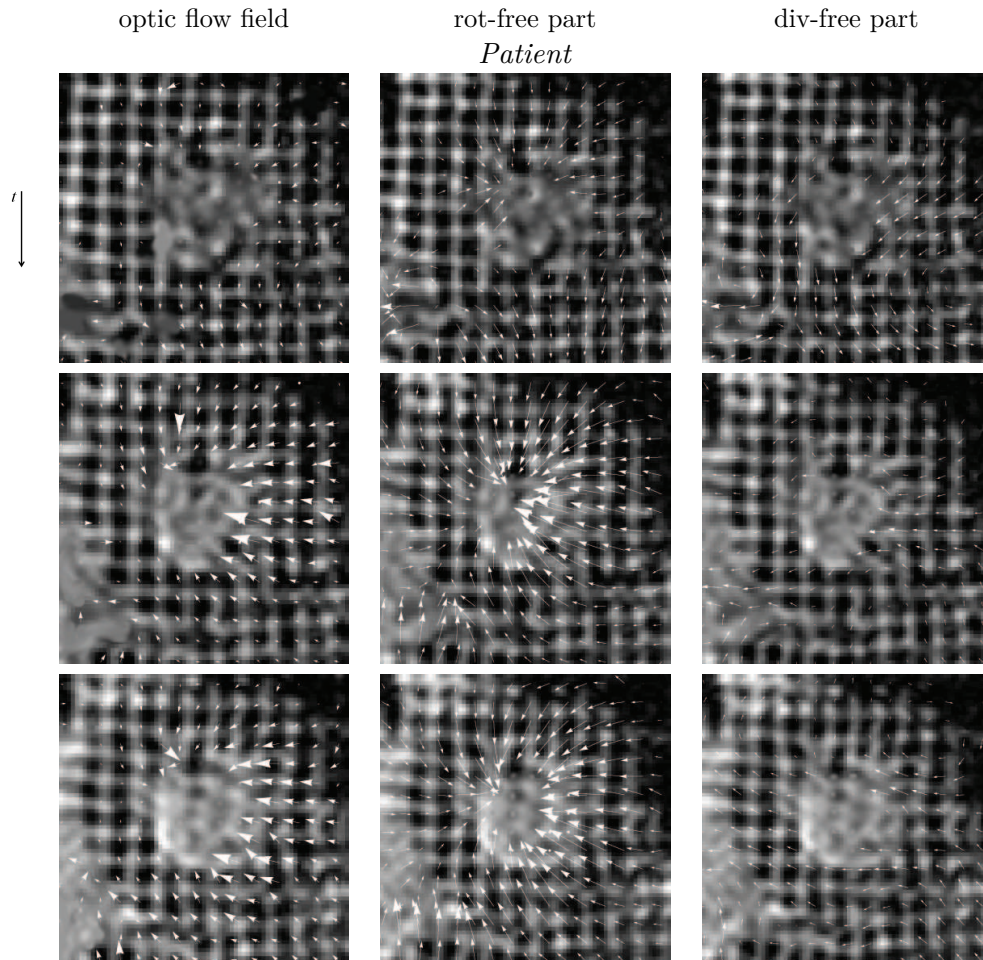


Figure 3.16: Cardiac motion field behavior a patient. We assess frame 3, 6 and 8 of a sequence of 11 frames displaying the cardiac muscle during systole. Column 1 shows the extracted motion fields, column 2 shows the rotation-free part, whereas column 3 shows the divergence-free part.

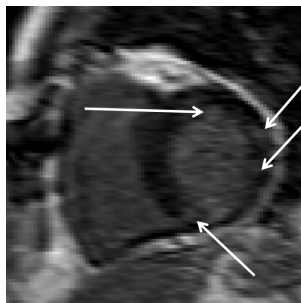


Figure 3.17: Diseased Heart. Arrows show areas where infarction occurred

*Es ist nicht genug zu wissen, man muss auch
anwenden.*

Es ist nicht genug zu wollen, man muss auch tun.

Johann Wolfgang von Goethe

Cardiac motion estimation: analysis of the kinetic Energy

Abstract

Estimations of the heart movement may help studying abnormalities of the myocardium. Cardiac motion fields are however difficult to interpret due to the high amount of information displayed at the same time. In order to simplify the visualization and analysis of such measurements, we extract kinetic energy from the cardiac motion fields. We also calculate the kinetic energy of the divergence-free and rotation-free components of the vector field, in order to study separately the contributions to the heart beat of the cardiac contractions and rotations. In the experiments we investigated the heart behavior of a group of healthy volunteers and one patient. Such experiments reveal that the patient's heart is characterized by a lower kinetic energy in comparison to the healthy subjects. The work concludes with an investigation of the local cardiac kinetic energy measurements. In an experiment with the patient, the kinetic energy estimations allowed to visualize areas associated to myocardial infarct.

4.1 Introduction

The analysis and quantification of cardiac movement is of great interest for the research community, since measurements of alterations in the wall motion may be indicators of diseases such as ischemia. Another great challenge is to localize, to measure the extension and to interpret the severity of infarcted areas in the myocardium. In the literature we find several techniques to detect and analyze abnormal cardiac wall deformation. Such methods are mostly related to stress and strain computation, which explore material deformation of the myocardium and provide information on the forces acting on the cardiac muscle and the influence of the blood pressure [2, 78, 15, 60]. In this work, however, we limit ourself to the analysis of the cardiac kinetic energy and we show that it is a highly promising parameter to explore dynamic cardiac behavior.

Optic flow methods provide automatic quantification of the cardiac dynamic behavior and visualize this information as velocity fields. In the optic flow method used in this work, dense motion fields are reconstructed from a sparse set of velocity features associated to the movement of critical points. The velocity estimation of critical points is carried out with respect to a local reference system with origin located at the critical point position.

Motion fields may be of great help in such investigations, but are complex and hard to interpret due to the high amount of information provided at the same time. A useful and compact way to display such information is to express cardiac movement in terms of scalar fields by means of kinetic energy evaluation.

The kinetic energy represents the energy characterizing an object due to its mo-

tion. In cardiology literature kinetic energy, associated with the cardiac blood flow estimation, has been employed to investigate the left atrium behavior in volunteers and patients with heart failure [155] or to analyze the blood pressure of the pulmonary artery in the presence of stenoses [3]. In such an approach the kinetic energy estimation is carried out by taking into account measurements of volume changes during systole and information of blood density. In order to study the left ventricle kinetics, energy measurements have been mainly carried out by optic flow methods [70, 42] with variational techniques based on the Horn and Schunck approach [76] illustrated in chapter 1.5.3.1. Also in these approaches, the authors tried to establish a measure of distinction between healthy subjects and the patients, providing global and local measurements.

In this chapter we investigate the kinetic energy of the computed motion field and the kinetic energy associated to its rotation-free and divergence-free components. Such a decomposition provides information on the contracting and rotating movements of the cardiac muscle, illustrating what component is more dominant (has higher energy) in different periods of the cardiac cycle. These measurements are carried out over time, globally and locally, where local estimations are displayed by means of the so-called bull's eye plot as a visualization tool.

In the tests we investigated motion extracted from tagged MR images, acquired from a group of 10 volunteers and a patient with myocardial infarcts. The measurements highlighted a strong difference in the amount of kinetic energy between the two groups, with the patient showing less kinetic energy for the whole period of investigation. Moreover, a comparison of the patient's local kinetic energy estimations with a late enhancement MR image, where infarcted areas were highlighted, showed an interesting correspondence between area with a local minimum kinetic energy and an area with scar tissue.

This chapter is subdivided as follows. In section 4.2 and 4.3 the kinetic energy formulation and the bull's eye plot visualization tool have been described. Finally in 4.4 and 4.5 the experiments and the results obtained are discussed.

4.2 Dense Motion Field and Kinetic Energy

For the sake of illustration in this section we briefly reformulate the optic flow equation proposed in section 3.7 and explore its extension for kinetic energy calculation.

As already seen, the optic flow equation relies on two major steps: scale space feature tracked over time and a dense velocity field reconstruction. In order to estimate moving patterns in an image sequence, given a bounded domain

$\Omega \subseteq \mathbb{R}^2$, we look for a velocity vector field $\mathbf{v} \in \mathbf{C}^0(\overline{\Omega})$ and $\mathbf{v} \in \mathbf{C}^1(\Omega)$ that minimizes the following energy functional

$$\begin{aligned}
\mathcal{E}^{\lambda, \mathbf{h}^k, \mathbf{d}^k}(\mathbf{v}^k) = & \\
& \sum_{q=1}^{N_B} w_q^k \sum_{j=1}^2 |(\phi_k^q, v^{k,j,\text{divfree}})_{\mathbb{L}_2(\Omega)} - d_q^{k,j,\text{divfree}}|^2 + \\
\lambda_1 \int_{\Omega} \sum_{i=1}^2 \sum_{j=1}^2 & |D_{x^i}^{h^{k,j,\text{divfree}}} v^{k,j,\text{divfree}}(\mathbf{x})|^2 \, d\mathbf{x} + \\
& \sum_{q=1}^{N_B} w_q^k \sum_{j=1}^2 |(\phi_k^q, v^{k,j,\text{rotfree}})_{\mathbb{L}_2(\Omega)} - d_q^{k,j,\text{rotfree}}|^2 + \\
\lambda_2 \int_{\Omega} \sum_{i=1}^2 \sum_{j=1}^2 & |D_{x^i}^{h^{k,j,\text{rotfree}}} v^{k,j,\text{rotfree}}(\mathbf{x})|^2 \, d\mathbf{x}
\end{aligned} \tag{4.1}$$

In equation (4.1) $\lambda \in \mathbb{R}^+$ controls the degree of smoothness. Symbol h^k represents the so-called gauge field, a motion field of the target phenomenon calculated previously and k is a variable indicating the time frame. In the proposed equation, $(\phi_k^q, v^{k,j})_{\mathbb{L}_2(\Omega)} - d_q^{k,j}$ represents the soft constraint, where ϕ is the Gaussian kernel and d is the velocity associated to a feature at certain scale; $q \in \{1, \dots, N_B\}$ enumerates the critical branch associated to each scale-space feature, $j \in \{1, 2\}$ represents the vertical and horizontal component of the field and w is a weighting factor. The smoothness term of (4.1) can be written as

$$\begin{aligned}
& \sum_{i=1}^2 \sum_{j=1}^2 |D_{x^i}^{h^{k,j}} v^{k,j}(\mathbf{x})|^2 = \\
& \sum_{i=1}^2 \sum_{j=1}^2 |v^{k,j}(\mathbf{x}) - \partial_{x^i}(\log h^{k,j}) v^{k,j}(\mathbf{x})|^2.
\end{aligned} \tag{4.2}$$

In (4.1) divfree and rotfree indicate the divergence-free and rotation free components of the vector field, obtained by employing results of the so-called Helmholtz decomposition (3.5). The minimization of equation (4.1) is carried out by solving the corresponding Euler-Lagrange equations.

Equation (4.1) provides a velocity vector for each pixel in the image sequence. Due to the highly complex information illustrated simultaneously, such vector fields are hard to interpret in clinical practice. In order to reduce the degree of complexity, the estimated vector fields have been converted into scalar fields by calculating the kinetic energy. Given a 2-dimensional cardiac image sequence,

the kinetic energy is defined as

$$KE = \frac{1}{2} \mathbf{m} \int_{\Omega} \sum_{j=1}^2 v_{k,j}^2(\mathbf{x}) d\mathbf{x} \quad (4.3)$$

where \mathbf{m} indicates the cardiac mass, which has been assumed constant in the experiments. Definition (4.3) has been used as the basis to define a set of measurements such as: KE^k , $KE^{k,\text{divfree}}$, $KE^{k,\text{rotfree}}$, $\frac{KE^{k,\text{divfree}}}{KE^{k,\text{divfree}}+KE^{k,\text{rotfree}}}$, $\frac{KE^{k,\text{rotfree}}}{KE^{k,\text{divfree}}+KE^{k,\text{rotfree}}}$ and $\frac{KE^{k,\text{divfree}}}{KE^{k,\text{rotfree}}}$, where k indicates the time frame.

In order to evaluate the contribution to the motion of certain areas in the cardiac walls, kinetic energy has been calculated in sectors defined by the bull's eye plot described in (4.3) and it has been integrated over a time period T , which in the tests correspond to the systolic period. Hence,

$$KE_{\square} = \frac{1}{2} \mathbf{m} \int_0^T \int_{\square \subseteq \Omega} \sum_{j=1}^2 v_j^2(\mathbf{x}, t) d\mathbf{x} dt \quad (4.4)$$

where \square represents the spatial sector of the cardiac walls over which the kinetic energy is calculated.

4.3 Bull's eye plot

The localization and size estimation of infarcted areas in the myocardium play a fundamental role in evaluating the severity of the patient's health condition and in planning therapy treatments. In routine clinical practice scar tissue detection occurs mostly by visual inspection, relying on the expertise and experience of the cardiologist. In order to improve this task, visualization techniques are required. According to the literature, the bull's eye plot is a widely used tool for the analysis and visualization of 2-dimensional slices in the left ventricle [34]. The bull's eye plot consists of three series of concentric rings, which, from extern to intern, provide information of the basal, middle and apical image slices of the left ventricle in the short-axis view (Figure 4.1, row 1). Every ring is divided into four (for apical slices) or six (for middle and basal slices) equi-spaced angular segments, which are color-coded and reflect the parameter values extracted from the myocardium. In our case the parameter is the kinetic energy. Segment 17 defines the apical cap, called apex, and represents the true muscle at the extreme tip of the ventricle. Such rings and angular segments can be subdivided in smaller regions in order to refine the visualization for smaller areas. An extension of such a visualization tool has been provided in [152], where information of the myocardial walls has been illustrated without showing discontinuities.

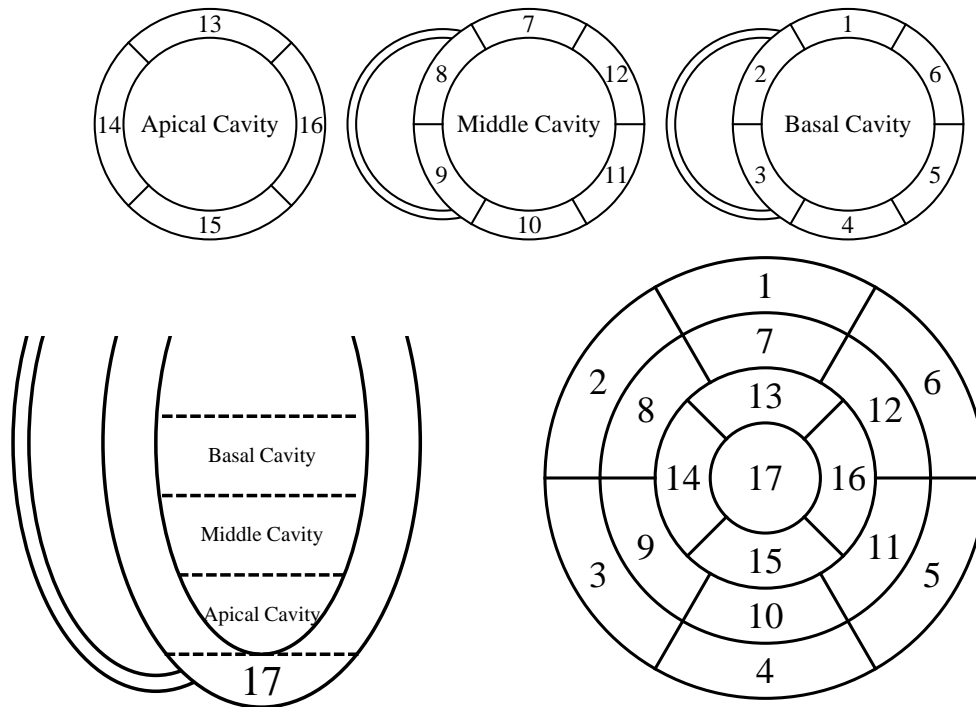


Figure 4.1: A bull's eye plot consists of 3 rings (basal, middle, apical cavity and the apex) and is divided in 17 segments. Row 1 shows the short axis slices. Row 2 left image displays the long axis slices. Row 2, right image illustrates the combination of bull's eye plots.

4.4 Experiments

In order to investigate the dynamic cardiac behavior, equation (4.1) has been applied on tagged MR images datasets acquired from 10 volunteers and one patient. In this section we consider only experiments carried out on short axis visualizations of the basal slice of the cardiac walls. The image acquisition took place at Leiden University Medical Center (LUMC) using a MR 1.5 Tesla scanner. In general each dataset has been acquired during both the systolic phases and consisted of more than 30 frames acquired in each session. Each image presented an in-plane spatial resolution of $1.2 \text{ mm} \times 1.2 \text{ mm}$ with time resolution of 2×10^{-2} seconds and with thickness of 8 mm . Of such frames, the first 15 presented well defined tags, which faded afterwards. Therefore, motion estimation has been carried out from frame 3 to frame 13 in order to reduce the temporal boundaries' influence. In the optic flow equation (4.1) we track feature points such as saddles over time and we reconstruct a dense motion field by imposing $\lambda = 10^{-6}$. In this case weighting factor w depends on the condition number of the Hessian matrix of the sparse velocity vectors as described in section 2.5.

In order to perform measurements only between the endocardium and epicardium of the left ventricle, motion fields have been masked by employing cardiac wall contours which were manually extracted. Finally, the kinetic energy has been calculated using the measurements defined in (4.2). In the estimations, the frame mean velocity has been removed, in order to decrease energy contributions from the rigid motion of the heart as a whole.

In the plots 4.2 and 4.3 kinetic energy estimations of the volunteers and the patient are compared. Measurements have been carried out with respect to the time frame, displayed in the x axis. In Figures 4.2 and 4.3 the patient's kinetic energy is illustrated with dots. In column 1 the ratio of the kinetic energy of either the divergence-free or rotation-free component and the sum of the kinetic energy of divergence-free and rotation-free is expressed. Column 2 shows the behavior of the kinetic energy ratio of the divergence-free and the rotation-free components. Finally column 3 provides information of the kinetic energy of the extracted velocity field, and its divergence-free and rotation-free components. In this latest case the mass is assumed constant, equal to 1 gram per pixel and uniformly distributed.

In Figures 4.2 and 4.3 column 3, it can be seen that in each frame the patient always presents less kinetic energy than the volunteers; namely, the patient maximum kinetic energy of the extracted motion field, rotation-free and divergence-free components are 241.4 Joules, 162 Joules and 33.8 Joules respectively. On the other side, the smallest kinetic energy maximum of the volunteers' motion field and its rotation-free and divergence-free components are 373.9 Joules, 222.2 Joules, 172.7 Joules respectively.

By using equation (4.4), the kinetic energy has been moreover calculated in sectors and displayed by means of the so-called bull's eye plot. Each one of the original 6 sectors of the visualization plot has been further subdivided into 96 sub-sectors, in order to provide a more accurate representation of the tissue behavior. Figure 4.4, 4.5, 4.6 and 4.7 illustrate the kinetic energy of the motion field, divergence-free and rotation-free components of the volunteers and patient integrated over the systolic period. In order to show strong differences in kinetic energy magnitude between the the volunteers and the patient, the intensity values of the volunteers plots were clipped by imposing the range of kinetic energy estimations calculated for the patient case (see Figures 4.4, 4.5 and 4.6). The range of kinetic energy in column 1 is $0 \leq KE \leq 7.6$ Joules, in column 2 is $0 \leq KE \leq 5.98$ Joules and in column 3 is $0 \leq KE \leq 1.51$ Joules. Such plots are color encoded, where colors provide information of kinetic energy magnitude, such that low energy is displayed in blue, middle high energy in green and high energy in yellow. The septum location is associated to the boundaries of sectors 2 and 3 of the bull's eye plot and is enhanced in red color. Such estimations point out once again that the patient kinetic energy is weak all over the cardiac walls, whereas volunteer plots present large green and yellow areas.

Figure 4.8 displays a late enhancement MR image of the patient's heart (top image), with scar tissue highlighted by a contrast agent, and the respective bull's eye plot (bottom image). The bull's eye plot shows a green region with relatively high kinetic energy, which provides the main contribution to the heart beat. This region illustrates in sector 1 an area with a localized minimum highlighted by a black arrow. This area is located close to an infarcted area highlighted by the white arrow in the Figure 4.8 top image. In sectors 4, 5, 6 the late enhancement image displays other infarcted regions, which in the bull's eye plot correspond to areas with very low kinetic energy (see black arrows Figure 4.8 bottom image).

4.5 Discussion

In this chapter we explore heart motion analysis and provide preliminary and promising results, by estimating the kinetic energy of a group of ten healthy subjects and one patient. Such measurements are useful for analyzing the cardiac behavior, may provide information of the cardiac health condition and may help in localizing areas with abnormal cardiac movement. Finally, in this work the kinetic energy of the rotation-free and divergence-free components have been also studied and the measurements have been carried out globally and locally.

Tests on the rotation-free and divergence-free components highlight that during the systole cardiac contractions present a higher energy, with respect to rotation, for both volunteers and the patient. However, compared to the volunteer estimations, the patient shows an overall weaker kinetic energy. It's interesting to notice that the patient's divergence-free kinetic energy contribution presents a maximum five times smaller than the volunteer's smallest energy maximum of the same type. We can therefore conclude that the rotational contribution is almost absent in the patient. This is also clear in the visualization of the patient's divergence-free motion field in Figure 3.16, column 3, where the vectors present a very small magnitude.

However, global measurements do not tell which part of the cardiac wall is contributing to the motion. Therefore, local kinetic measurements have been carried out and the outcomes have been visualized in a modified version of the classical bull's eye plot. Tests performed on volunteers show large areas with green to yellow colors (i.e. high energy) across the whole ring, while in the patient the motion contributions are located especially in sectors 1, 2 and 6. Moreover, tests carried out on the patient highlighted in sector 1 a region with a local minimum between regions with significant kinetic energy. A comparison with a late enhancement cardiac image showed that there was correspondence between the location of the infarcted area in the image and the location of the

local minimum in the bull's eye plot (Figure 4.8). The late enhancement cardiac image display other infarcted areas in sectors 4, 5 and 6, which correspond to regions with very low kinetic energy in sectors 4, 5 and 6 of the bull's eye plot. However, the whole sectors 4, 5, and 6 exhibit low and similar kinetic energy and this leads to a more difficult visual detection of the infarcted areas.

In such MR images contrast agents are used to enhance patterns, such as infarcted areas. Contrast agents, however, have to be injected in the human body and may provoke allergic reactions [26]. On the other side the newly presented kinetic energy quantification technique is not invasive and showed promising results in finding a scar tissue area. In the future it would be interesting to test this method on a larger group of patients. If similar performance would be achieved and the kinetic energy provides information of infarcted areas also in other cases, then besides strain [162], cardiac kinetic measurements might become an effective tool to be employed to limit the usage of contrast agents.

Finally, in this work we assumed the mass constant and equal to 1 gram per pixel. This is of course a very simple choice that does not take into account the density changes due to contraction and relaxation. In estimating the kinetic energy from 2-dimensional cardiac images, the area of tissue from which we carry out the measurements, changes over time also due to through plane heart movement. The total mass of the heart is therefore not preserved and this affects the accuracy of the measurements. In order to overcome this, in the future research we will constrain the optic flow equations such that the mass will be kept constant.

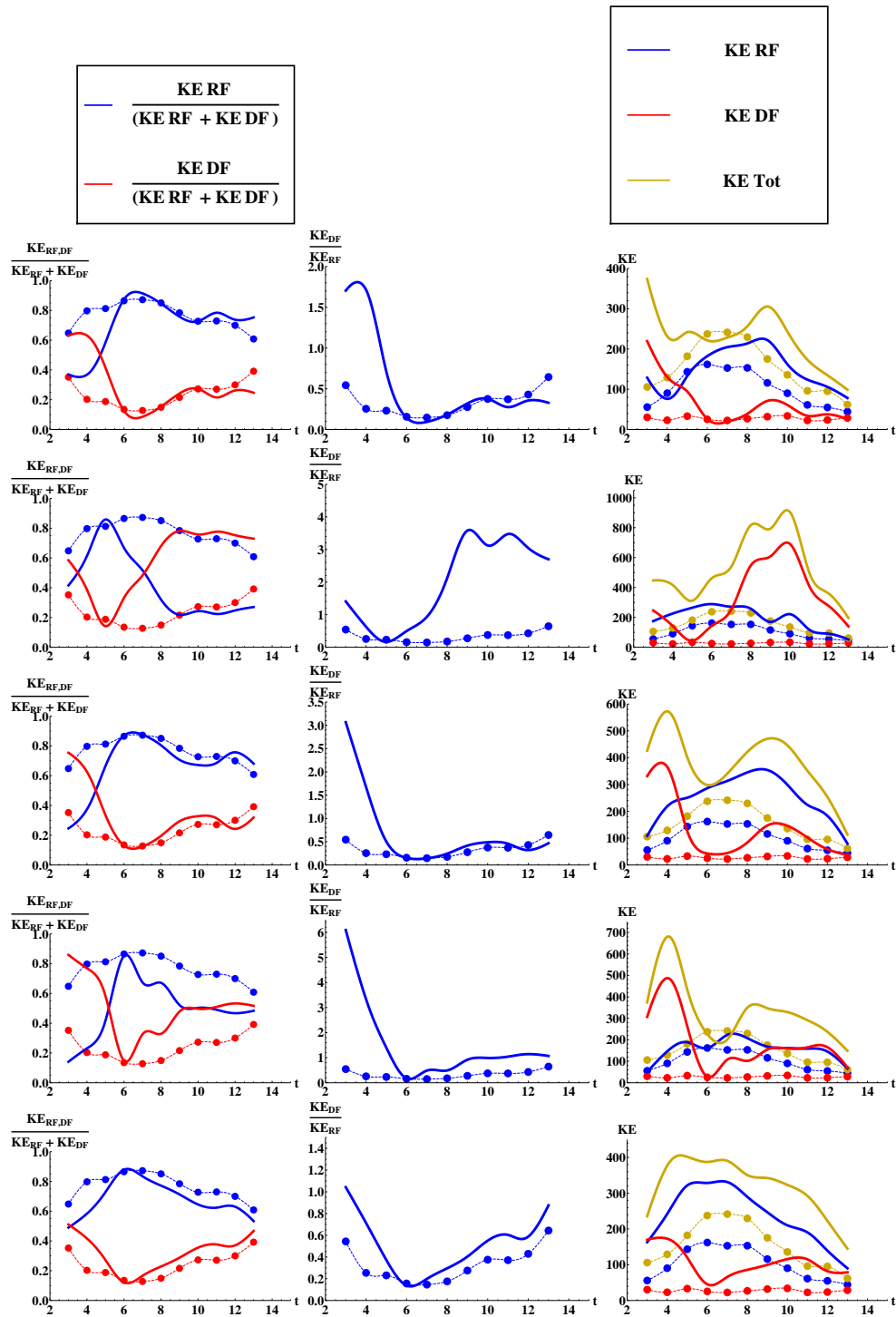


Figure 4.2: Kinetic energy behavior of volunteer 1, 2, 3, 4, 5 and the patient are compared. Patient's behavior is displayed with dots. In the graph KE, DF, RF are kinetic energy, divergence-free and rotation-free components respectively.

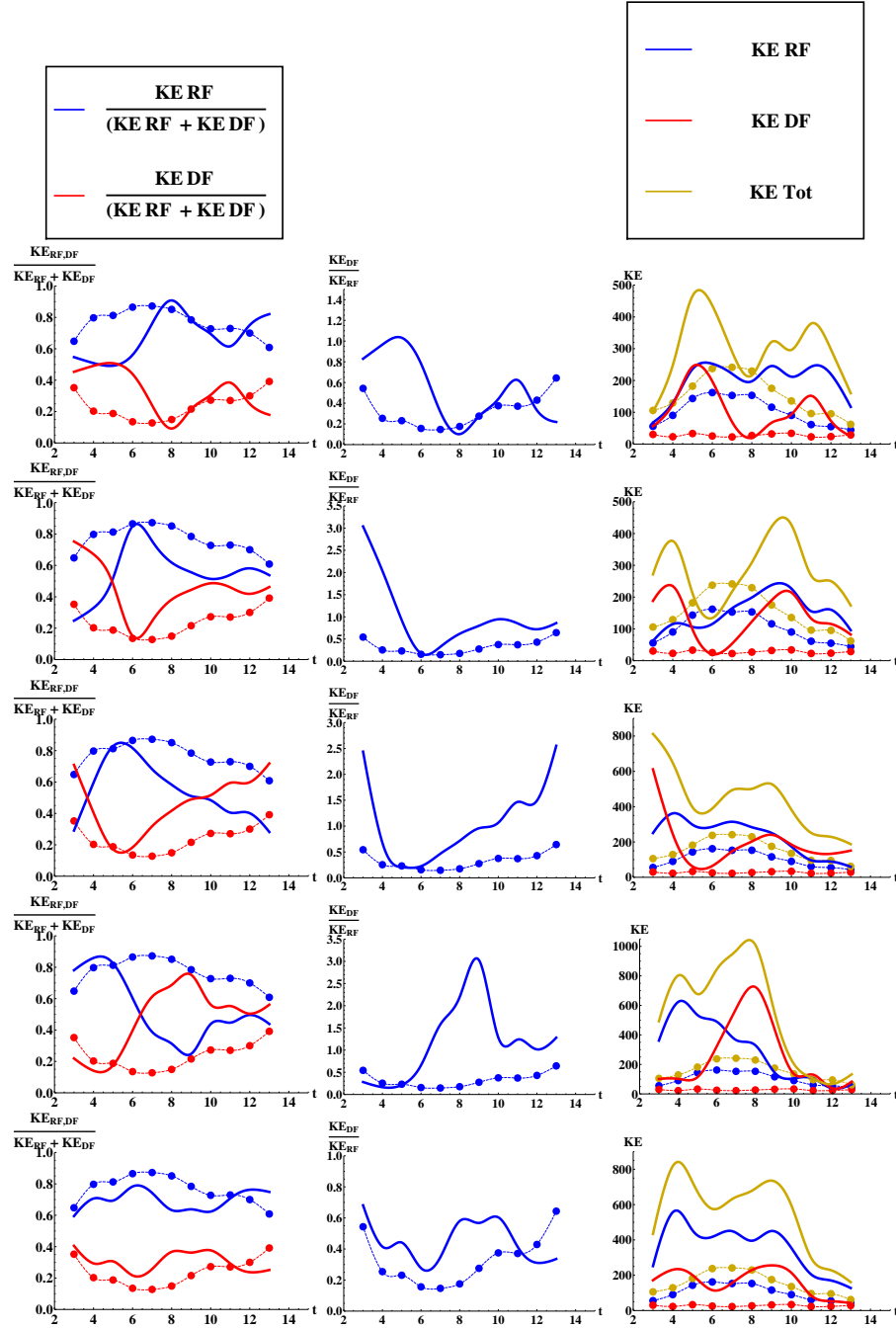
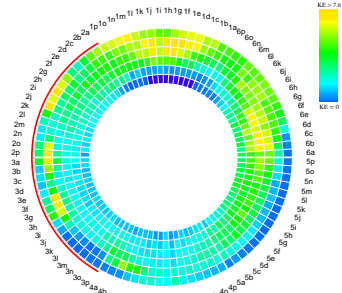
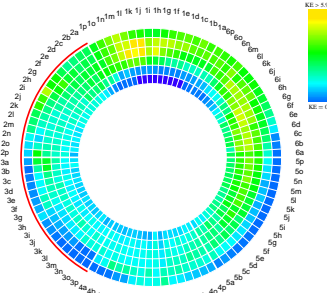


Figure 4.3: Kinetic energy behavior of volunteer 6, 7, 8, 9, 10 and the patient are compared. Patient's behavior is displayed with dots. In the graph KE, DF, RF are kinetic energy, divergence-free and rotation-free respectively.

KE over time optic flow field



KE over time rot-free part



KE over time div-free part

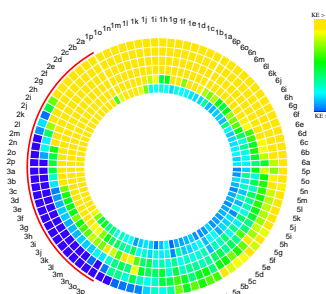
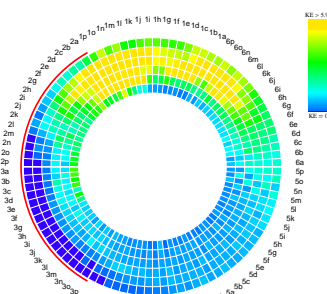
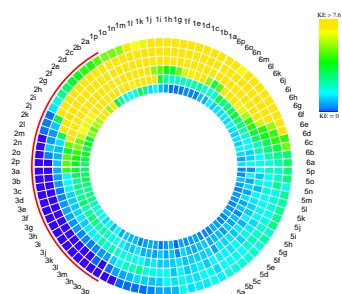
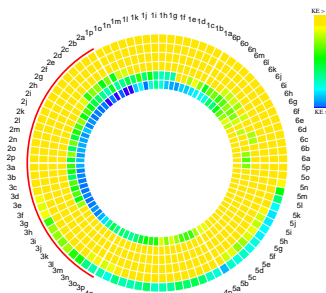
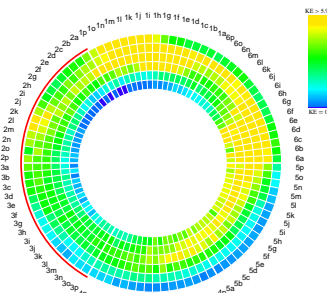
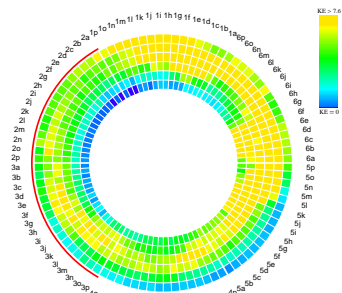
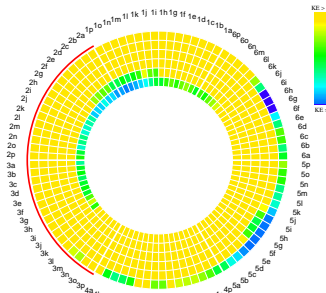
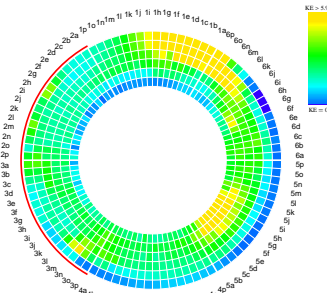
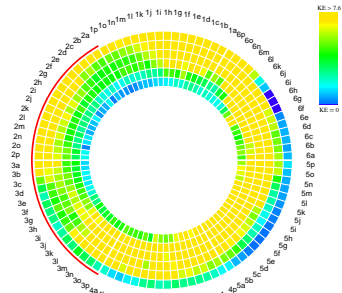
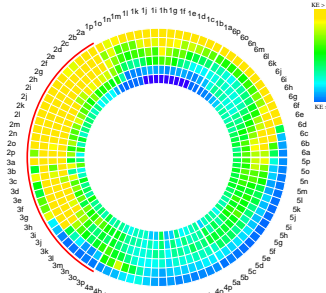


Figure 4.4: Bull's eye plot: Kinetic energy integrated over systole. Row from 1 to 4 illustrate the kinetic energy of the first 4 volunteers. From left to right, kinetic energy of motion field, rotation-free and divergence-free component respectively. Range of kinetic energy: in column 1 $0 \leq KE \leq 7.6$ Joules, in column 2 $0 \leq KE \leq 5.98$ Joules and in column 3 $0 \leq KE \leq 1.51$ Joules.

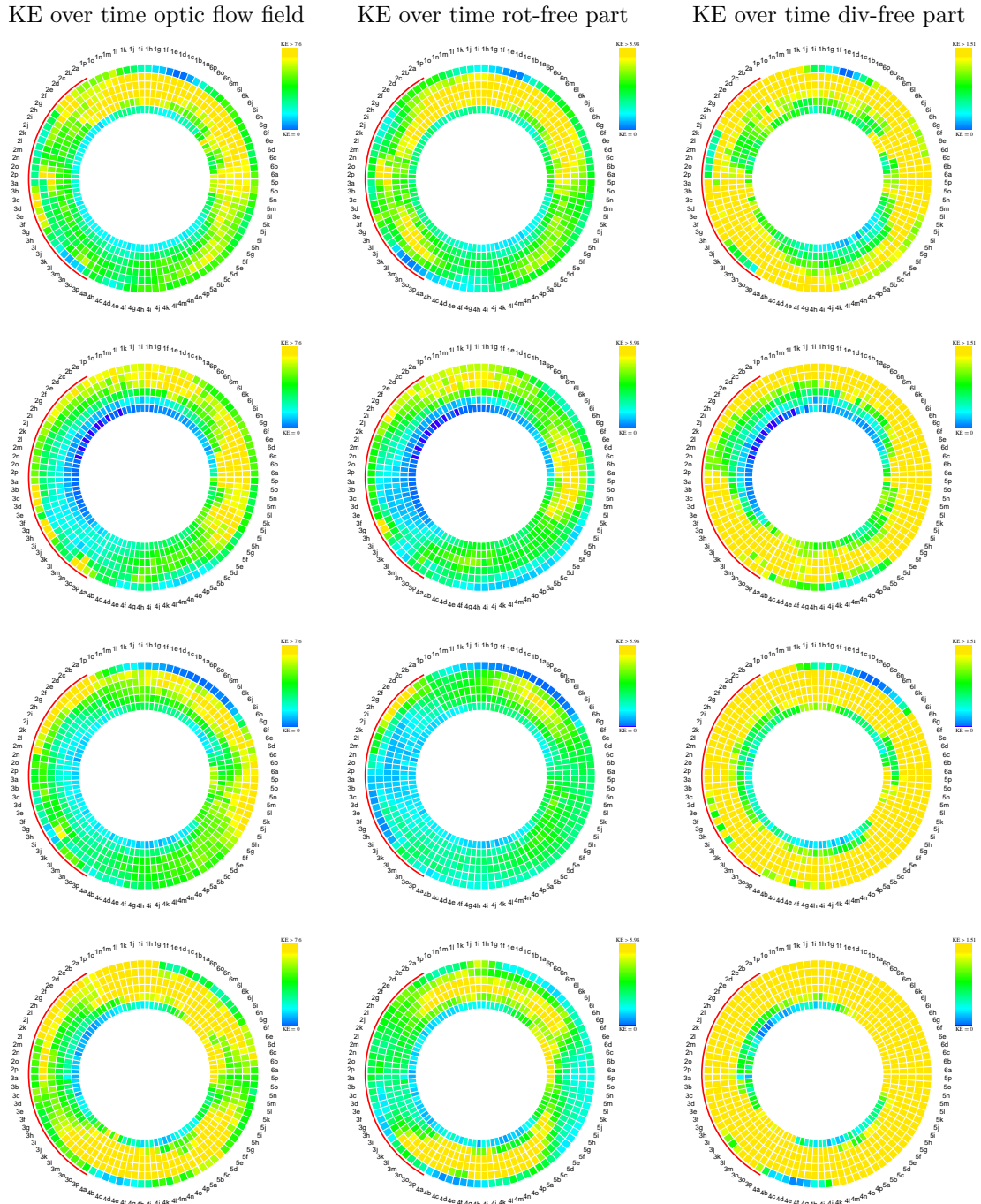


Figure 4.5: Bull's eye plot: Kinetic energy integrated over systole. Row from 1 to 4 illustrate the kinetic energy of volunteer 5 to 8. From left to right, kinetic energy of motion field, rotation-free and divergence-free component respectively. Range of kinetic energy: in column 1 $0 \leq KE \leq 7.6$ Joules, in column 2 $0 \leq KE \leq 5.98$ Joules and in column 3 $0 \leq KE \leq 1.51$ Joules.

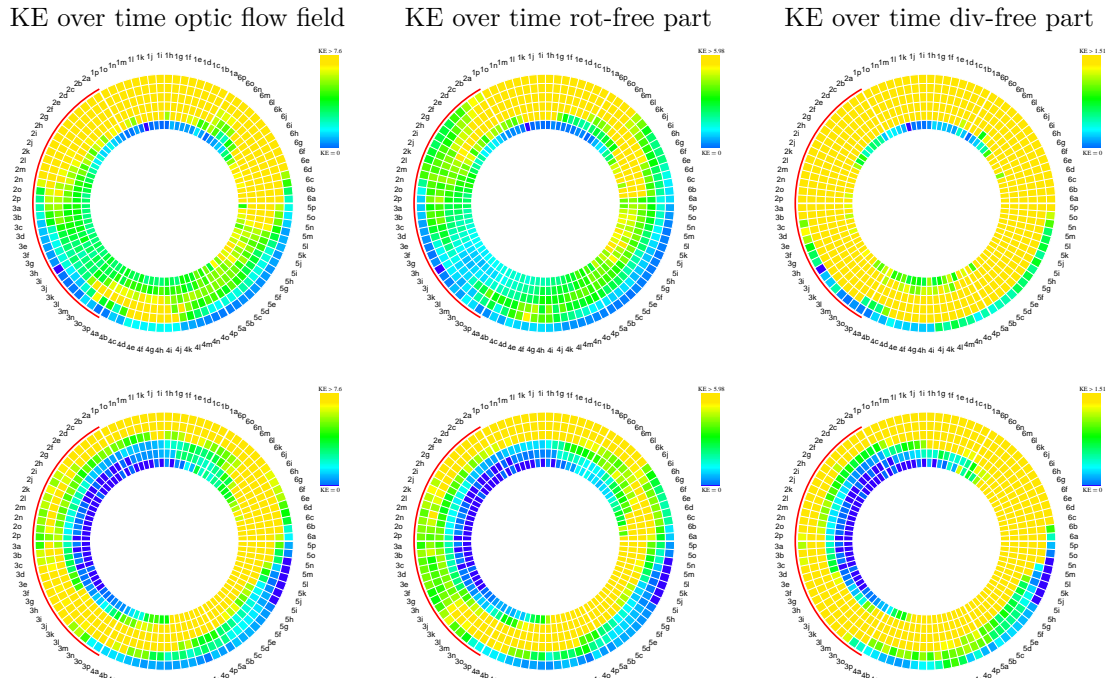


Figure 4.6: Bull's eye plot: Kinetic energy integrated over systole. Row from 1 to 2 illustrate the kinetic energy of volunteer 9 and 10. From left to right, kinetic energy of motion field, rotation-free and divergence-free component respectively. Range of kinetic energy: in column 1 $0 \leq KE \leq 7.6$ Joules, in column 2 $0 \leq KE \leq 5.98$ Joules and in column 3 $0 \leq KE \leq 1.51$ Joules.

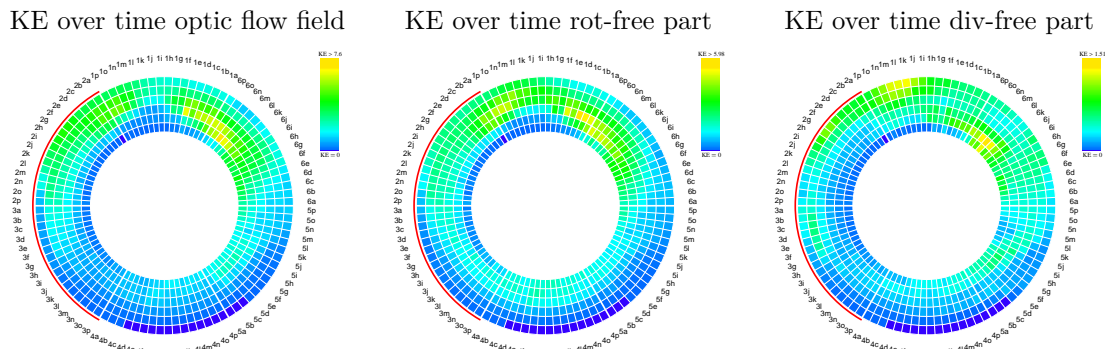


Figure 4.7: Bull's eye plot representing kinetic energy integrated over systole period: patient case. From left to right, kinetic energy of motion field, rotation-free component and divergence-free component. Range of kinetic energy: in column 1 $0 \leq KE \leq 7.6$ Joules, in column 2 $0 \leq KE \leq 5.98$ Joules and in column 3 $0 \leq KE \leq 1.51$ Joules.

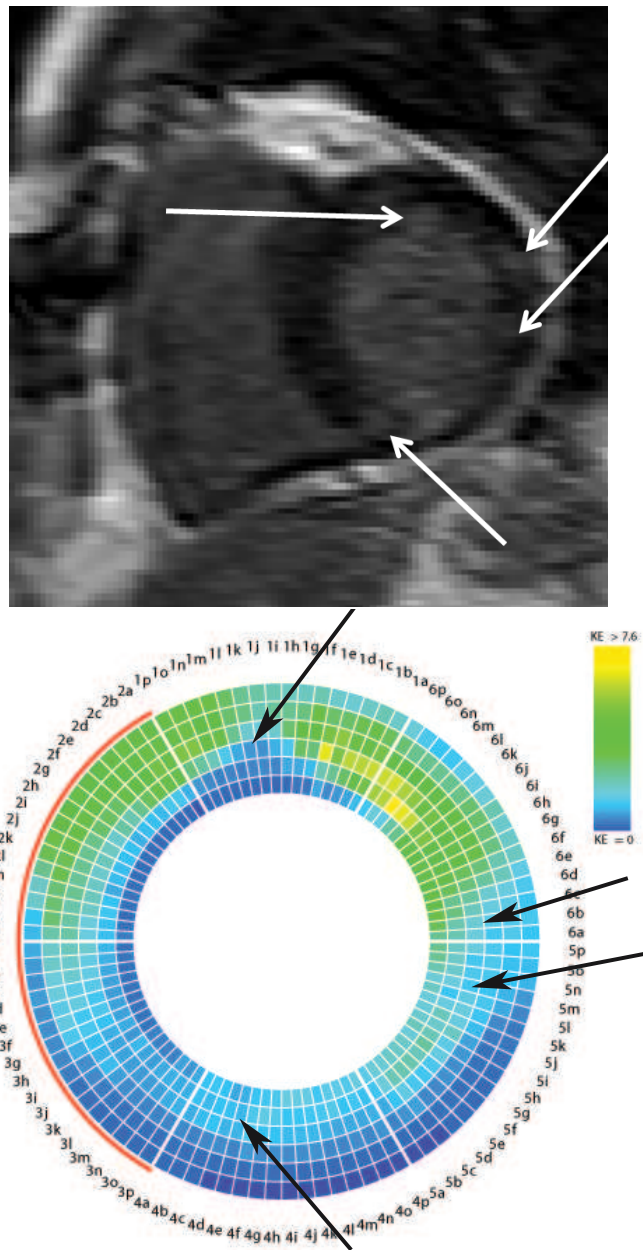


Figure 4.8: Patient's late enhancement MR image (top image) and bull's eye plot of the kinetic energy extracted from the respective motion field (bottom image). In the late enhancement image the arrows point to infarcted regions. In the bull's eye plot these areas present very low kinetic energy (see arrows bottom image). The area in sector 1 corresponds to the area with a localized kinetic energy minimum in the bull's eye plot.

*All life is an experiment. The more experiments
you make the better.*

Ralph Waldo Emerson, poet

Motion extraction: further experiments

Becciu A., Duits R., Janssen B.J., Florack L.M.J., ter Haar Romenij B.M.
and H.C. van Assen. Feature based optic flow estimation using covariant
derivatives and Helmholtz decomposition: Application to cardiac tagged
MRI sequences. To be submitted to the international journal *IEEE Trans-
actions on Medical Imaging*.

5.1 Introduction

In literature several methodologies exist that carry out motion estimation. In order to understand the advantages and drawbacks of each technique it is crucial to evaluate and compare their performance with the same image sequences and with a known ground truth. In this chapter the performance of the optic flow algorithm illustrated and discussed in chapter 3 (equation (3.47)), feature based optic flow with Helmholtz decomposition and covariant derivatives (FBHDCD), is compared with the performance of well known optic flow techniques in the literature such as the Horn and Schunck approach [76], the Lucas and Kanade method [111] and the tuple image multi-scale optic flow equation (TIMS OFCE) developed by Van Assen et al. [163]. Tests are carried out on a phantom with a known ground truth. Accuracy of the extracted motion field has been assessed using the so-called average angular error (AAE) [20] and L2 norm. Experiments revealed that the FBHDCD exhibits the smallest error $AAE = 3.84$ degrees and L2 norm= 0.1.

In tagged MR images intensity varies over time due to T1 decay. In order to evaluate the robustness against brightness changes, the new method is tested directly on the cardiac tagged MR images of a volunteer.

In sections 5.2, 5.3 and 5.4 we describe the phantom used, the two experiments carried out and the performances achieved. Finally, in section 5.5 the results and the future directions are discussed.

5.2 Phantom

In the experiments a digital phantom created in our group has been used [161]. The phantom consists of two sequences with elongated horizontal and vertical stripes. Figure 5.2 illustrates three subsequent frames. The digital phantom mimics the behavior of a mechanical phantom used for tagged MR image acquisitions. This phantom consists of two concentric cylinders, the inner cylinder has radius R_1 and moves with angular displacement ω_1 with respect to a fixed cylinder with radius R_2 (see Figure 5.1). The environment between the walls of the two cylinders is filled with standard gelatine, which deforms according to the movement of the inner cylinder. The angular displacement of the gelatine at any point with radius R with respect of the center of rotation is based on the analytic solution described by Young et al. in [176]. Hence,

$$\omega(R) = \omega_1 \frac{R_2^{-2} - R^{-2}}{R_2^{-2} - R_1^{-2}} \quad (5.1)$$

with $\omega(R_1) = \omega_1$ and $\omega(R_2) = 0$, where the parameter ω_1 represents the angular displacement at radius R_1 . Parameters R_1 , R_2 and ω_1 have been acquired experimentally.

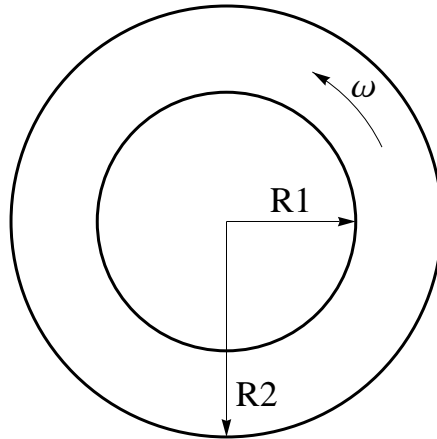


Figure 5.1: The phantom consists of two concentric cylinders with radius R_1 and R_2 . The inner cylinder moves with angular displacement ω_1 , whereas the outer cylinder is fixed.

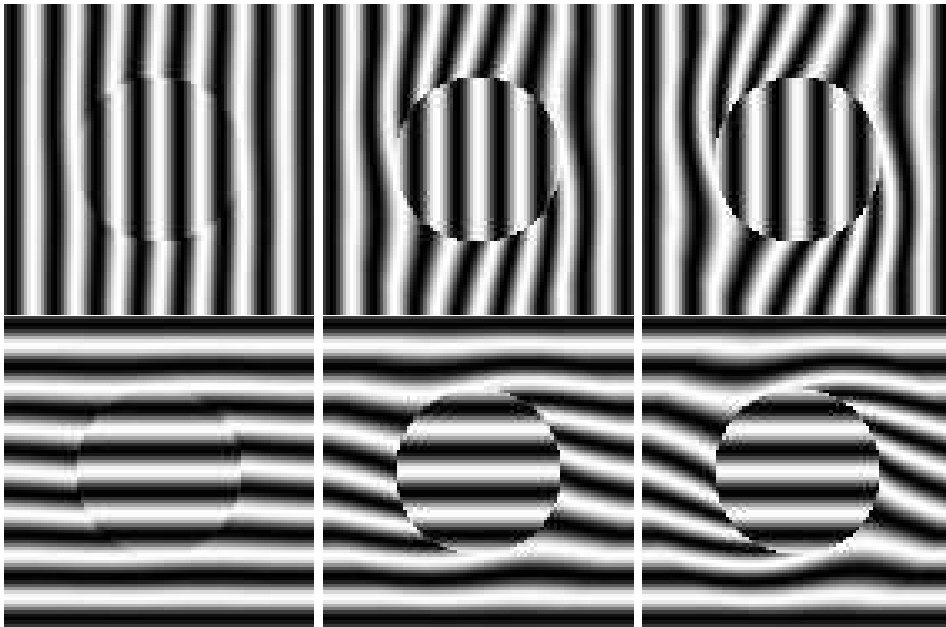


Figure 5.2: Three subsequent frames of the rotating digital phantom used in the experiments.

5.3 Experiment 1: performance of optic flow techniques

The performance of FBHDCD has been compared with the performance of three different optic flow techniques currently used in our group. All methods have been implemented in Mathematica [173] and are: the tuple image multi-scale optic flow equation [163], recall equation (1.12), the Lucas and Kanade [111], and the Horn and Schunck [76], see equations (1.9) and (1.4) respectively. These optic flow algorithms have been applied to three subsequent frames of the phantom described in 5.2, which consists of 13 frames of 93×93 pixels.

The FBHDCD algorithm has been computed using a combination of maxima, minima and saddles as feature points (over 230 feature points per frame), with spatial scale chosen within the range $s = \{1, 1.22, 1.48, 1.81, 2.21, 2.69, 3.28, 4.\}$ and temporal scale $\tau = 1$. As in section 3.8, we employ the same optimized smoothing parameter values $\lambda_1 = 10^2$ and $\lambda_2 = 10^3$ and the same optimized parameter values that take into account the gauge field influence in the phase of vector field reconstruction ($\eta_1 = 0.5$ and $\eta_2 = 0.9$). Computational time per frame has been estimated from five to ten minutes.

The TIMS OFCE algorithm has been assessed using a combination of the following spatial and temporal scales, namely

$$s = \{1.5, 1.61, 1.72, 1.85, 1.98, 2.13, 2.28, 2.45, 2.63, 2.82, 3.02, 3.24, 3.48, 3.73, 4\}$$

and $t = (1.5, 1.73, 2)$. The scales were selected using the minimum condition number of matrix B for each pixel in the image. Also in this case each frame was calculated in roughly five minutes. However, the computational time significantly depends on the amount of spatial and temporal scales involved. An increase in the number of scales employed produces an increase in the computational time.

In the Lucas and Kanade algorithm (equation (1.9)), motion has been extracted in a window of observation of 5×5 pixels. The technique employs the following weighting function to give more prominence to the central pixel of the window

$$W = \frac{1}{16} \begin{bmatrix} 1 & 2 & \sqrt{6} & 2 & 1 \\ 2 & 4 & 2\sqrt{6} & 4 & 2 \\ \sqrt{6} & 2\sqrt{6} & 6 & 2\sqrt{6} & \sqrt{6} \\ 2 & 4 & 2\sqrt{6} & 4 & 2 \\ 1 & 2 & \sqrt{6} & 2 & 1 \end{bmatrix}$$

The flow for each frame has been calculated in less than 10 seconds.

In the Horn and Schunck method (equation (1.4)) the motion field has been estimated with a smoothness parameter $\lambda = 0.5$. Velocity fields have been calculated in less than 40 seconds per frame.

5.3.1 Results

The extracted motion fields have been compared with a known ground truth and the accuracy has been assessed in terms of L2 norm and Barron's average angular error (AAE) [20]

$$\text{Angular Error} = \arccos\left(\frac{V_t}{\sqrt{u_t^2 + v_t^2 + 1}} \cdot \frac{V_e}{\sqrt{u_e^2 + v_e^2 + 1}}\right) \quad (5.2)$$

where V_t is the true vector with spatial component u_t, v_t , and time component 1, whereas V_e is the estimated velocity vector and u_e, v_e and 1 are its spatial and time components respectively.

The FBHDCD algorithm exhibits the smallest average angular error and L2 norm. The measurements are averaged over the 3 investigated frames. The FBHDCD method shows $AAE = 3.84$ and L2 norm = 0.1. Tables 5.1 and 5.2 illustrate the average angular error and the L2 norm error of the discussed optic flow algorithms. Figure 5.3 shows the Barron's angular error (left image) and L2 norm error (right image) per pixel of the FBHDCD algorithm for one frame. In Figure 5.3 the intensity values represent the error magnitude, dark areas correspond to regions with small errors and bright intensities correspond to pixels with high angular errors. The words "small error" and "high error" respectively represent AAEs and L2 norm much smaller and much larger than the FBHDCD's AAE and L2 norm averaged over the investigated 3 frames. Errors larger than 10 degrees have been clipped for AAE, while errors larger than 0.5 have been clipped for the L2 norm image plot. Notice that the highest errors are located around the inner cylinder. Figure 5.4 exhibits the retrieved motion field of one frame and the corresponding ground truth, larger arrows and arrow heads are related to larger flows. In these plots the arrow's length has been amplified 15 times.

5.4 Experiment 2: cardiac motion estimation from tagged MR images

The tuple image multi-scale optic flow algorithm is tuned for applications on phase images. The method assumes that the phase is preserved over the image

Optic Flow Methods	FBHDCD	FBSD	TIMS OFCE	Lucas and Kanade	Horn and Schunck
AAE Frame 3	3.50°	5.15°	4.20°	5.66°	5.55°
AAE Frame 4	4.24°	5.59°	5.91°	5.19°	5.97°
AAE Frame 5	3.77°	5.24°	6.27°	4.40°	5.81°

Table 5.1: Performance of the optic flow methods. Average angular error is measured for all pixels in the image. The optic flow method described in this thesis presents the smallest $AAE = 3.84$ degrees. This error measurement value is the average of AAE for the 3 investigated frames. The acronym FBHDCD is used for "feature based optic flow with Helmholtz decomposition and covariant derivatives", FBSD "feature based optic flow using standard derivatives" and TIMS OFCE is the abbreviation for "tuple Image multi-scale optic flow constraint equation"

Optic Flow Methods	FBHDCD	FBSD	TIMS OFCE	Lucas and Kanade	Horn and Schunck
L2 Norm Frame 3	0.084	0.13	0.11	0.17	0.14
L2 Norm Frame Frame 4	0.12	0.15	0.18	0.24	0.17
L2 Norm Frame Frame 5	0.11	0.15	0.19	0.25	0.17

Table 5.2: Performance of the optic flow methods: magnitude error. L2 norm is measured for all pixels in the image. The optic flow method described in this thesis presents the smallest L2 norm= 0.10. This error measurement value is the average of the L2 norm for the 3 investigated frames. The acronym FBHDCD is used for "feature based optic flow with Helmholtz decomposition and covariant derivatives", FBSD "feature based optic flow using standard derivatives" and TIMS OFCE is the abbreviation for "tuple Image multi-scale optic flow constraint equation"

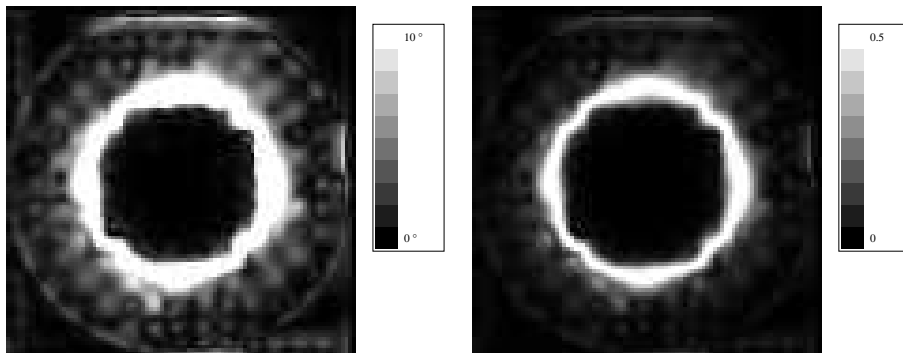


Figure 5.3: Average angular error (left image) and L2 norm error per pixel of frame 3 using the FBHDCD method. Angular errors were clipped at 10 degrees (degree symbol \circ), while L2 norm error were clipped at 0.5. Dark areas represent small angular errors, whiter regions depict larger errors. We notice that the highest errors are located around the inner cylinder due to a strong discontinuity at the boundaries: motion is observed outside the inner cylinder, while no motion is observed inside the inner cylinder.

sequence. A direct application of this technique on the tagged MR images might be therefore not suitable.

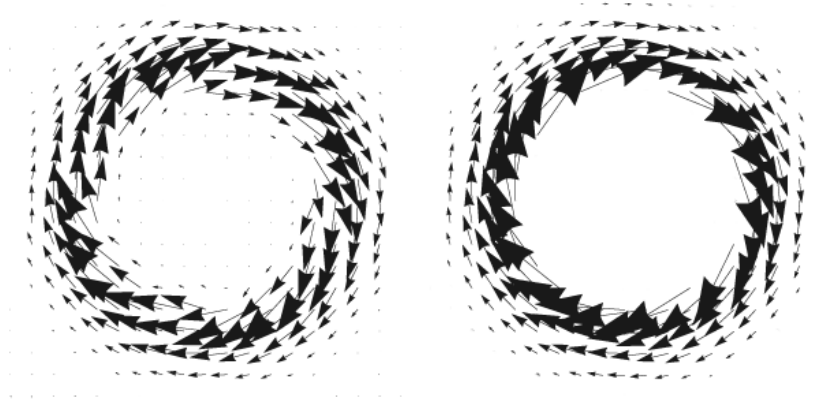


Figure 5.4: Reconstructed vector field (left image) and ground truth (right image) of frame 3. Larger arrows and arrow heads indicate larger flows. In these plots the arrow's length has been amplified 15 times.

While the Lucas and Kanade and Horn and Schunck algorithms are based on the assumption that patterns in the image sequence maintain constant intensity over time, the optic flow algorithm FBHDCD assumes that feature points maintain their characteristics over time. That is, it assumes that critical points will be still a critical points even in the presence of brightness changes. This method has been therefore applied directly to tagged MR images, which present fading due to T1 relaxation time. Figure 5.5 shows four subsequent frames with the retrieved velocity fields extracted from the tagged MR images of the contracting left ventricle of a volunteer. Visual inspection confirms that the retrieved motion fields describe realistically the movement of the cardiac walls.

5.5 Discussion and Conclusion

In this chapter the algorithm defined in 3.47 has been furthermore investigated and its performance has been compared with the performance of very well known optic flow methods in the literature such as the Horn and Schunck approach [76], Lucas and Kanade method [111] and the tuple multi-scale optic flow equation of van Assen et al. [163].

The optic flow algorithms were tested on an artificial phantom from which the ground truth is known and the accuracy of the retrieved vector field has been described in terms of Barron's average angular error (AAE) and L2 norm. The optic algorithm FBHDCD showed excellent performance and provided the smallest error ($AAE = 3.84$ degrees and $L2 \text{ norm} = 0.1$). In section 3.8 the algorithm was tested on the same three subsequent frames and using the same parameters values ($\lambda_1, \lambda_2, \eta_1$ and η_2). However, in that case best performance

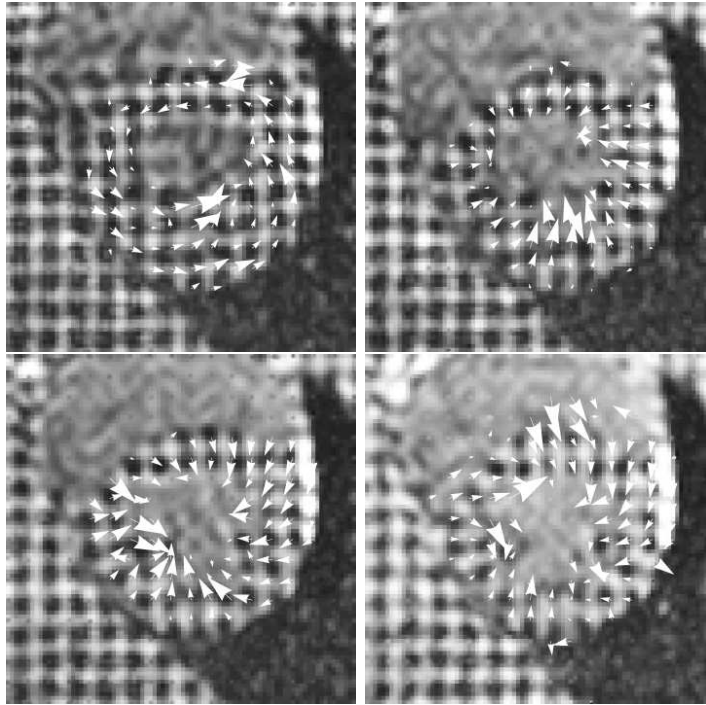


Figure 5.5: Motion fields extracted from tagged MR images of the left ventricle of a volunteer. The images were not converted into phase images. Motion estimation has been performed using the motion field algorithm described in chapter 3.

has been achieved at $AAE = 6.68^\circ$ and $L2 \text{ norm} = 0.16$. The reason for this poorer result is related to the amount of features employed. In section 3.8 maxima were the only feature points used. Each frame exhibited roughly 60 maxima. In the experiments carried out in this chapter we instead use a combination of maxima, minima and saddle points (over 230 critical points per frame), therefore it can be concluded that the accuracy of the reconstructed vector field is strongly dependent on the number of features used in the algorithm. In case of few feature points, techniques based on the optic flow constraint equation have to be preferred.

In the future we will carry out experiments with other feature points such as the scale-invariant feature transform (SIFT) points, which may furthermore improve the algorithm performance.

Due to the high amount of steps undertaken by the FBHDCD method, recall the algorithm overview in Figure 3.1, at the moment the time required to calculate the motion field for each frame of the sequence is roughly 5-10 minutes. Speed tuning was not the goal of the project and therefore it has not been carried out in this work. However in the future, computational expensive parts of the algorithm can be implemented in integrated circuits like field-programmable

gate arrays (FPGAs), which will speed up considerably the final reconstruction of the motion field.

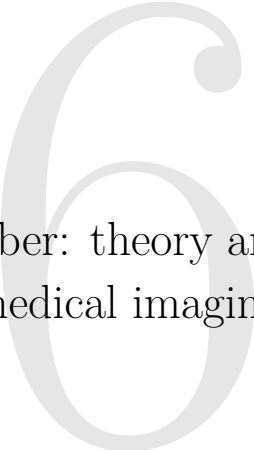
So far we have computed optic flow fields from images with constant brightness, such as the phase images described in 2.2 and 3.2. Tagged MR images exhibit brightness changes over time and in the literature they are converted into phase images, which preserve intensity, with the goal to use methods based on the brightness constancy assumption. The optic flow method FBHDCD has been applied also on these images. Phase images allow to create geometry patterns, from which a large amount of critical points, that move along with the tagging structure, is retrieved. However, the conversion of the tagged MR images into phase images have been performed by filtering the image spectrum in the Fourier domain. Thus we also filter out significant information related to the motion estimation. Our feature based algorithm is not based on constant brightness. As illustrated in Figure 5.5, our technique has been successfully applied directly to tagged MR images. In the future we will carry out experiments on the tagged MR images of phantoms like the one described in 5.2, to discuss how much motion information has been lost in transforming MR images into phase images and at the same time to quantify the accuracy of the motion field retrieved directly from tagged MR images.

5.6 Acknowledgements

Implementation and experiments using the tuple image multi-scale optic flow equation have been carried out by Dr Hans van Assen. Implementation and experiments using the Lucas and Kanade approach and the Horn and Schunck method have been carried out by Laurens Leeuwis during his internship supervised by the author of this dissertation.

*For the wise man looks into space and he knows
there is no limited dimensions.*

Lao Tzu, philosopher



3D winding number: theory and application to medical imaging

This chapter is based on:

Becciu A., Fuster A., Potték M., van den Heuvel B.J.P., ter Haar Romeny B.M. and van Assen H.C. 3D Winding Number: Theory and Application to Medical Imaging. Accepted for publication in the special issue *Modern Mathematics in Biomedical Imaging* of the *International Journal of Biomedical Imaging*.

Note This work was carried out in close cooperation with Dr Andrea Fuster. The theory was conceived by Andrea Fuster and was numerically implemented and developed into a range of applications by the author of this dissertation.

Abstract.

We develop a new formulation, mathematically elegant, to detect critical points of 3D scalar images. It is based on a topological number, which is the generalization to three dimensions of the 2D winding number. We illustrate our method by considering three different biomedical applications, namely, detection and counting of ovarian follicles and neuronal cells and estimation of cardiac motion from tagged MR images. Qualitative and quantitative evaluation emphasize the reliability of the results.

6.1 Introduction

Critical points are very helpful for different purposes and applications in computer vision as key points, landmark points, anchor points and others. In segmentation, for example, critical points have been used to characterize deforming areas of the brain [174] or to enhance ridges and valleys in MR images [63]. In image matching, mappings between the considered images are computed based on their critical points [141, 72]. Image matching has been also performed through so-called *top points*, critical points for which the determinant of the Hessian matrix is equal to zero [131, 17] or through the popular Harris points [74] and the SIFT key point detector [110]. Critical points have also been used in motion estimation algorithms, where the optic flow field is generated from a sparse set of velocities associated to multi-scale anchor points [165, 21].

Critical point detection is an established research field. Blom [23], for example, classifies critical points by counting the sign changes between the analyzed pixels and its neighbors in a hexagonal grid. Nackman [103] defines the image topology in terms of slope districts. The ridge and valley lines are described as the ascending and descending slopes coming from saddle points. The dales and hills are identified as districts whose lines of slope converge to/come from the same pit/peak. These methods have been extensively employed for 2-dimensional applications. In recent years there has been a strong increase of computational power and 3D scalar images are becoming the standard data of investigation, especially in medical imaging. Three-dimensional critical point techniques allow for a more realistic analysis of human organ behavior. For example, tracking algorithms applied on a 2-dimensional heart image sequence retrieve only in-plane contractions and rotations of the cardiac walls but miss the through-plane components. The through-plane components are instead retrieved with 3-dimensional optic flow approaches. In this work we show an application where

the presented critical point detection algorithm is embedded in a feature point based motion estimation technique.

In this chapter we work with a topological number (from homotopy theory) that can locate critical points of scalar images in an arbitrary number of dimensions. In two dimensions it reduces to the so-called winding number and has been studied in detail in [89, 90, 88]. In physics, and in modern cosmology in particular, the winding number appears in the context of topological defects such as monopoles, cosmic strings and domain walls (see, for example, [166] and references therein). We consider this topological number in three dimensions and refer to it as 3D winding number. Properties of this approach are significant:

- The 3D winding number provides information on the character of the critical points.
- The winding number is independent of the shape of hyper-surface S around which is calculated. It is a topological entity.

The chapter is organized in the following way. After some preliminaries (section 6.2.1), we treat extensively the theoretical aspects of the winding number in three dimensions and explain the implementation of our algorithm (sections 6.2.2 and 6.2.3). In sections 6.2.4 and 6.2.5 we describe a methodology to refine the position of the retrieved critical points and we propose a classification of critical points based on the winding number. Furthermore, we test the viability of our method by considering three different biomedical applications, namely, follicle and neuronal cell counting, and cardiac motion estimation in sections 6.3.1, 6.3.2 and 6.3.3 respectively. Finally, in section 6.4 we discuss the results and possibilities for future work.

6.2 Theory

6.2.1 Preliminaries

A critical point of a smooth function $f(x^1, \dots, x^n)$ is a point $\mathbf{x} = (x^1, \dots, x^n)$ for which the gradient of f vanishes, $\nabla f|_{\mathbf{x}} = 0$. In any other case the point is said to be regular. Critical points can be further classified depending on whether the Hessian matrix at the considered point is singular:

$$\det (\partial_i \partial_j f)|_{\mathbf{x}} = 0 \tag{6.1}$$

This is obviously the case if one or more matrix eigenvalues are zero. Such critical points are called degenerate. Otherwise we deal with non-degenerate critical points.

We are interested in finding and classifying critical points of a scalar image $L(\mathbf{x})$. We will do so by computing a topological quantity ν at every point in the image. The topological number of a d -dimensional scalar image at a point \mathbf{x} (with at most isolated singularities) is defined by [89]

$$\nu = \oint_S \Phi(\mathbf{x}) \quad (6.2)$$

where Φ is a $(d-1)$ -form depending on the image intensity and its derivatives (see for example [120] for a general discussion of differential forms). The precise definition of Φ in d dimensions can be found in [89]. In this chapter we will only consider the case $d=3$ (further details are given in next section). The integration is performed on a closed, oriented (hyper)surface S around the considered point.

An important property of Φ is the fact that it is a closed form, $d\Phi=0$. If the image has no singularities in the region V enclosed by S the generalized Stoke's theorem can be applied to (6.2):

$$\nu = \oint_S \Phi(\mathbf{x}) = \int_V d\Phi(\mathbf{x}) \equiv 0 \quad (6.3)$$

Therefore, the quantity ν is just zero at a regular point. At a singular point it takes values of $k\pi$, with k some non-zero integer number depending on the number of dimensions and the character of the singularity¹. The described number is called topological because it does not depend on the chosen hyper-surface of integration in (6.2). Another important property is the fact that it is conserved within such an hyper-surface, i.e., when two or more singularities are enclosed their topological numbers add up. We refer to [89] for a more detailed discussion on these and other properties of ν in an arbitrary number of dimensions.

6.2.2 Winding number in three dimensions

In three dimensions, the integrand in equation (6.2) is a 2-form given by [89]:

$$\Phi = \frac{L_i dL_j \wedge dL_k \epsilon^{ijk}}{(L_l L_l)^{3/2}}, \quad i, j, k, l = x, y, z \quad (6.4)$$

¹ This is true for $d \geq 2$.

Here the indices i, j, k, l can take on values x, y or z , $L = L(x, y, z)$ is the intensity function of a 3-dimensional image, L_x, L_y, L_z are the components of the spatial gradient of the intensity function, $\nabla L = (L_x, L_y, L_z)$, and ϵ is the 3-dimensional Levi-Civita symbol. The wedge product is represented by \wedge . In this chapter we use Einstein's summation convention, i.e., a sum is taken over repeated indices appearing in both subscripts and superscripts. In explicit form equation (6.4) reads:

$$\Phi = \frac{2}{\|\nabla L\|^3} (L_x dL_y \wedge dL_z + L_y dL_z \wedge dL_x + L_z dL_x \wedge dL_y) \quad (6.5)$$

where $\|\nabla L\|$ is the gradient norm. Using the following relations

$$dL_i = L_{ix} dx + L_{iy} dy + L_{iz} dz \quad (6.6)$$

we can rewrite (6.5) as

$$\begin{aligned} \Phi = \frac{2}{\|\nabla L\|^3} \{ & dx \wedge dy [(L_{yx}L_{zy} - L_{yy}L_{zx})L_x + (L_{zx}L_{xy} - L_{zy}L_{xx})L_y + \\ & (L_{xx}L_{yy} - L_{xy}L_{yx})L_z] + \\ & dy \wedge dz [(L_{yy}L_{zz} - L_{yz}L_{zy})L_x + (L_{zy}L_{xz} - L_{zz}L_{xy})L_y + \\ & (L_{xy}L_{yz} - L_{xz}L_{yy})L_z] + \\ & dz \wedge dx [(L_{yz}L_{zx} - L_{yx}L_{zz})L_x + (L_{zz}L_{xx} - L_{zx}L_{xz})L_y + \\ & (L_{xz}L_{yx} - L_{xx}L_{yz})L_z] \} \end{aligned} \quad (6.7)$$

This expression was also given in [150]. After further inspection we notice that it can be reformulated in the following way:

$$\begin{aligned} \Phi = \frac{2}{\|\nabla L\|^3} \{ & dx \wedge dy [(\nabla L_x \times \nabla L_y) \cdot \nabla L] + \\ & dy \wedge dz [(\nabla L_y \times \nabla L_z) \cdot \nabla L] + \\ & dz \wedge dx [(\nabla L_z \times \nabla L_x) \cdot \nabla L] \} \end{aligned} \quad (6.8)$$

where $\nabla L = (L_x, L_y, L_z)$ and

$$\nabla L_x \equiv \partial_x(\nabla L) = (L_{xx}, L_{yx}, L_{zx}) \quad (6.9)$$

$\nabla L_y, \nabla L_z$ are defined analogously. This new form is more elegant and simpler to work with. Comparing (6.7) and (6.8) it is also clear that the latter form will be easier to implement. In what follows we will therefore use expression (6.8) rather than (6.7). In compact form we have:

$$\Phi = \frac{1}{\|\nabla L\|^3} (\nabla L_i \times \nabla L_j) \cdot \nabla L dx^i \wedge dx^j \quad (6.10)$$

where i, j take on values x, y or z . In this formulation Φ is antisymmetric as the vector product is anti-commutative.

6.2.3 Implementation

We study the nature of every voxel by performing the integration of expression (6.8) on a $3 \times 3 \times 3$ cube that contains it. Note that, for each face of the cube, only one term in (6.8) survives in the integration given by equation (6.2). For example, if we integrate on a cube face with $z = \text{constant}$ it is clear that $dz = 0$ and therefore only the first term has to be taken into account.

One of the issues we face in the implementation is the integration of differential forms. We make use of the following identity for integration of differential forms in Euclidean space [149]:

$$\int_{\Omega} f(x^1, \dots, x^n) dx^1 \wedge \dots \wedge dx^n = \pm \int_{\Omega} f(x^1, \dots, x^n) dx^1 \dots dx^n \quad (6.11)$$

Here, $f(x^1, \dots, x^n) dx^1 \wedge \dots \wedge dx^n$ is a n -form² in \mathbb{R}^n and Ω is an oriented domain. Note that the integral on the right-hand side is just the usual integral of the function $f(x^1, \dots, x^n)$. The sign on the right-hand side depends on the orientation of the considered integration domain (+ for positively oriented, – for negatively oriented). For example, from (6.8) and (6.11), the integration on $z = \text{constant}$ opposite cube faces reads

$$\nu_{xy} = \int_{z=\text{const.}} \Phi = \frac{2}{\|\nabla L\|^3} \left(\int_{\text{up}} (\nabla L_x \times \nabla L_y) \cdot \nabla L dx dy - \int_{\text{down}} (\nabla L_x \times \nabla L_y) \cdot \nabla L dx dy \right) \quad (6.12)$$

We consider the image intensity function on the faces of a $3 \times 3 \times 3$ cube to be $L = L(x_{\alpha+a}, y_{\beta+b}, z_{\gamma+c})$, where a, b, c are shifting indices of a plane on the cube taking on values 0, 1, 2 and $\alpha = 1, \dots, N_x - 2$, $\beta = 1, \dots, N_y - 2$, $\gamma = 1, \dots, N_z - 2$ are indices of the image volume with N_x, N_y and N_z representing the volume size in x, y and z directions. With these conventions, equation (6.12) can be expressed numerically as

$$\nu_{xy}^{\alpha, \beta, \gamma} = \sum_{a,b=0}^2 (\nabla L_x \times \nabla L_y) \cdot \nabla L (x_{\alpha+a}, y_{\beta+b}, z_{\gamma+2}) - \sum_{a,b=0}^2 (\nabla L_x \times \nabla L_y) \cdot \nabla L (x_{\alpha+a}, y_{\beta+b}, z_{\gamma}) \quad (6.13)$$

The winding numbers on planes $x = \text{constant}$ and $y = \text{constant}$ can be computed in a similar way. The total winding number for the considered cube is then

$$\nu^{\alpha, \beta, \gamma} = \nu_{xy}^{\alpha, \beta, \gamma} + \nu_{yz}^{\alpha, \beta, \gamma} + \nu_{zx}^{\alpha, \beta, \gamma} \quad (6.14)$$

² If the considered differential form has more than one component the identity simply holds for each one of them.

The numerical implementation of the 3D winding number algorithm can be summarized in the following steps:

- Initialize scalar image $L(x, y, z)$.
- Calculate the winding number for all voxels in the image volume.


```

for  $\alpha = 1$  to  $N_x - 2$  do
  for  $\beta = 1$  to  $N_y - 2$  do
    for  $\gamma = 1$  to  $N_z - 2$  do
       $\nu^{\alpha,\beta,\gamma} = \nu_{xy}^{\alpha,\beta,\gamma} + \nu_{yz}^{\alpha,\beta,\gamma} + \nu_{zx}^{\alpha,\beta,\gamma}$ 
    end for
  end for
end for

```
- Divide the outcomes of $\nu^{\alpha,\beta,\gamma}$ by 4π .
- In order to distinguish the type of critical points retrieved (maxima or minima from saddles), extract the sign of the Hessian matrix determinant at locations where $\nu^{\alpha,\beta,\gamma} \neq 0$.

6.2.4 Refinement of critical point positions

Due to signal discretization, the retrieved critical point location might not be completely accurate (see Figure 6.1 for an illustration of this issue for the 1D and 2D case). The position can be refined at sub-pixel level by considering the Taylor expansion of the intensity gradient around the retrieved point:

$$\begin{aligned} \nabla L(\mathbf{x}) = & (L_x(\mathbf{x}_e) + (x - x_e)L_{xx}(\mathbf{x}_e) + (y - y_e)L_{xy}(\mathbf{x}_e) + (z - z_e)L_{xz}(\mathbf{x}_e), \\ & L_y(\mathbf{x}_e) + (x - x_e)L_{yx}(\mathbf{x}_e) + (y - y_e)L_{yy}(\mathbf{x}_e) + (z - z_e)L_{yz}(\mathbf{x}_e), \\ & L_z(\mathbf{x}_e) + (x - x_e)L_{zx}(\mathbf{x}_e) + (y - y_e)L_{zy}(\mathbf{x}_e) + (z - z_e)L_{zz}(\mathbf{x}_e)) \end{aligned} \quad (6.15)$$

where $\mathbf{x} = (x, y, z)$ and $\mathbf{x}_e = (x_e, y_e, z_e)$ denote the true and estimated critical point location respectively. We can write equation (6.15) in a more compact form:

$$L_i(\mathbf{x}) = L_i(\mathbf{x}_e) + (j - j_e)L_{ij}(\mathbf{x}_e) \quad (6.16)$$

where i, j can take on values x, y or z . The intensity gradient at a critical point vanishes. The refined critical point position is therefore:

$$\begin{pmatrix} x \\ y \\ z \end{pmatrix} = \begin{pmatrix} x_e \\ y_e \\ z_e \end{pmatrix} - HL^{-1}(\mathbf{x}_e) \begin{pmatrix} L_x(\mathbf{x}_e) \\ L_y(\mathbf{x}_e) \\ L_z(\mathbf{x}_e) \end{pmatrix} \quad (6.17)$$

Here H is the Hessian matrix. Equation (6.17) provides the critical point position at subpixel level and can be iterated until the desired accuracy has been reached.

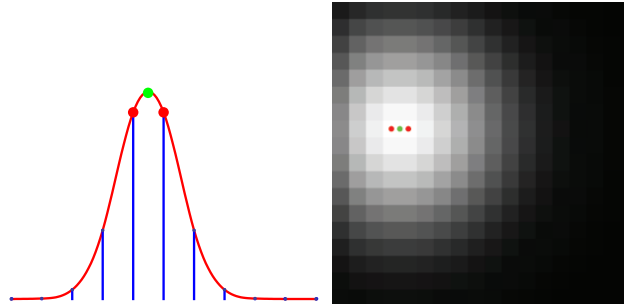


Figure 6.1: Critical point refinement. Left image: A continuum Gaussian signal in 1 dimension and the corresponding sampled signal. The sampled signal shows maxima at two nearby positions (points in red), which are at different locations from the real maximum (point in green). Right image: Rasterized version of a 2-dimensional Gaussian signal. Red points are the retrieved maxima, whereas the green point is the true maximum obtained after the refinement.

6.2.5 Classification of critical points

In three dimensions there are four types of non-degenerate critical points, namely, minima, 1-saddles, 2-saddles and maxima. They are characterized by the number of negative eigenvalues of the 3×3 Hessian matrix, the index, at the corresponding point: 0, 1, 2 or 3. Each 1-saddle (2-saddle) point is connected to two, not necessarily distinct, minima (maxima) by integral lines. A more detailed description of 3D saddle points can be found in [113].

The winding number at a certain image point is given by the integral of expression (6.10) on an appropriate surface enclosing the point. The winding number of (isolated) critical points in three dimensions takes values of $4k\pi$, with $k = \pm 1$ [150, 151]. We will argue that the winding number can be used for classification of extrema and saddle points in 3D. As a matter of fact, the winding number is able to distinguish between the two types of saddle points in 3D.

In Tables 6.1 and 6.2 we summarize the explicit values for the index and winding number of the different types of critical points. For completeness, we treat also the 2-dimensional case. Note that extrema in 3D can have either positive or negative winding number, unlike the 2D case. Saddles have positive or negative winding number as well, depending on the type of saddle point. It is now possible to classify critical points according to their winding number. Once the sign has been calculated it suffices to examine the image intensity at the considered point and its close neighborhood to distinguish between a minimum and a 2-saddle or a maximum and a 1-saddle.

The proposed correspondence between the index and winding number in three dimensions is well-grounded. The following has been shown for a non-degenerate

2D	<i>index</i>	<i>winding number</i>
minimum	0	$+2\pi$
saddle	1	-2π
maximum	2	$+2\pi$

Table 6.1: Index and winding number of critical points in 2D.

3D	<i>index</i>	<i>winding number</i>
minimum	0	$+4\pi$
1-saddle	1	-4π
2-saddle	2	$+4\pi$
maximum	3	-4π

Table 6.2: Index and winding number of critical points in 3D.

3D	<i>sign (det H)</i>	<i>winding number</i>
minimum	+	$+4\pi$
1-saddle	-	-4π
2-saddle	+	$+4\pi$
maximum	-	-4π

Table 6.3: Correspondence between the sign of the Hessian determinant and winding number for critical points in 3D.

critical point in an arbitrary number of dimensions [89]:

$$\nu = \text{sign}(\det H) C_d \quad (6.18)$$

where H is the Hessian matrix and C_d is a constant depending only on the number of dimensions d . In three dimensions C_d is equal to 4π . The relation between the winding number and the sign of the Hessian in $d = 3$ is given in Table 6.3. This is clearly in agreement with the postulated winding number for the different types of critical points.

6.3 Experiments

The proposed algorithm has been implemented in Mathematica [173] and it has been tested on three different biomedical applications, viz. follicle detection, neuronal cell counting and cardiac left ventricle motion analysis. In order to

perform the experiments we make use of the scale-space framework [79, 108, 94, 151, 54]. The Gaussian scale-space representation $L : \mathbb{R}^3 \times \mathbb{R}^+$ of a 3-dimensional static image $\mathbf{x} \mapsto f(\mathbf{x}) \in \mathbb{L}_2(\mathbb{R}^3)$ is given by the spatial convolution with a Gaussian kernel

$$L(\mathbf{x}, s) = (f * \phi_s)(\mathbf{x}) , \text{ with } \phi_s(\mathbf{x}) = \frac{1}{4\pi s} \exp\left(-\frac{\mathbf{x}^2}{4s}\right) \quad (6.19)$$

where $\mathbf{x} = (x, y, z) \in \mathbb{R}^3$ and $s > 0$ represents the scale. In the remainder of the chapter the image intensity function should be regarded as a function of both location and scale, $L = L(\mathbf{x}, s)$.

6.3.1 Follicle detection

Ovarian follicles are the basic eggs of the female reproductive system. In particular the number of primordial follicles decreases with the age reaching a minimum during the menopause. Therefore, follicle analysis and counting may provide information on fertility prospects [35, 52, 135]. At the stage of development that they can be measured with 3D ultrasound, the human follicles present roughly a spherical shape with a typical diameter of two to five *mm* and appear darker with respect to surrounding tissue on ultrasound images (see Figure 6.3) [114].

Detection and counting of follicles is usually carried out manually by inspecting the 2D slices from a 3D data set. This is a repetitive and tedious task which might introduce mistakes especially in the typically noisy data sets. Robust and automated detection of follicles is therefore useful.

In the experiments we automatically locate and count ovarian follicles of three different patients using ultrasound image volumes with a size of $128 \times 110 \times 180$, $138 \times 116 \times 176$ and $180 \times 108 \times 126$ voxels respectively. Image acquisition has been carried out by an experienced echographer with 3D ultrasound system Combison 5600 (Kretz Technik AG, Medicor, Austria / Korea), which has been equipped with a 12 MHz transvaginal 3D probe of 2.2 *cm*. The system performs image volume acquisition in about 2 seconds and allows to reliably detect follicles with diameter of 3 *mm* or bigger. The image data were processed in order to include only the ovary after the scanning.

In the images the center of the follicles exhibits a local minimum intensity. In these points the intensity gradient vanishes. Due to the noisy nature of the images, the data sets exhibit several locations where minima occur outside the follicle structure, producing false positives. The follicle detection algorithm consists of two main steps:

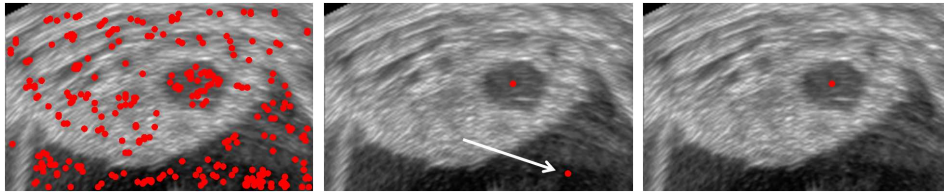


Figure 6.2: Follicle detection. The red dots highlight the detected minima. The left image shows detected minima at scale $s = 2$. The image is very noisy and the algorithm detects also the minima corresponding to noisy grains (false positives). The central image shows minima detected at scale $s = 9$. The arrow shows a minimum detected outside the ovarian tissue (false positive), whereas the red dot inside the ovarian tissue corresponds to the center of a follicle. In the right image the false positive outside the ovarian boundaries has been filtered out.

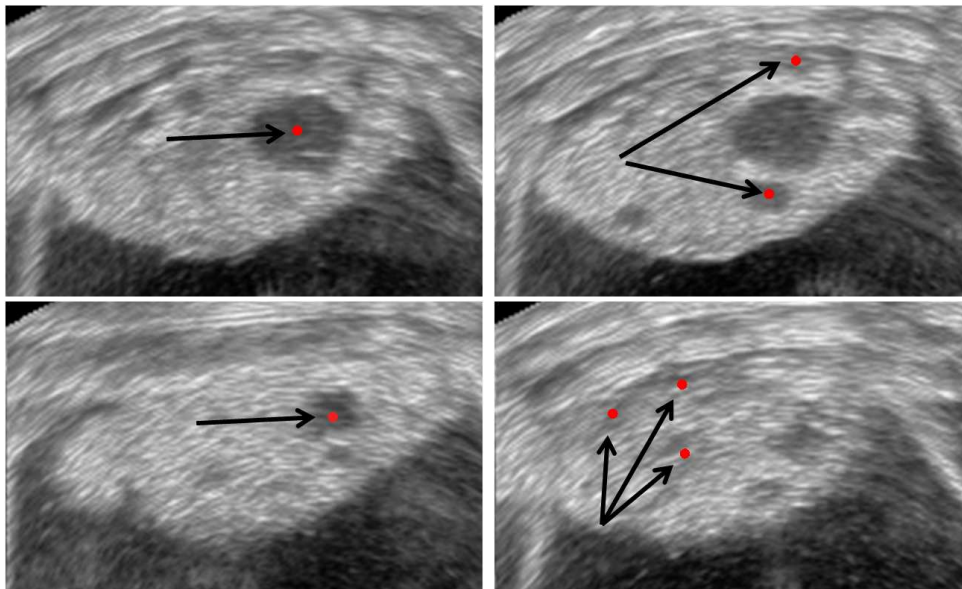


Figure 6.3: Follicle detection. 2D slices of the 3D ultrasound image smoothed data set corresponding to one of the patients. Lighter areas display the ovary, dark circular blobs are the follicles. Red dots indicate retrieved local minima in 3D at scale $s = 9$ voxels.

- The 3D volume images have been isotropically smoothed using different scales.
- Evaluation of the 3D winding number is carried out in order to retrieve the follicle centers.

In this procedure we observe a trade-off situation for the choice of the proper scale. We notice that follicles present a larger structure with respect to grains of the raw data. In the experiments the scale is heuristically chosen sufficiently

high to avoid grain detection (see Figure 6.2, left image for critical point detection at small scale), but not so high that smaller follicles are missed. In this experiment the results of follicles extraction have been achieved at scale $s = 9$ voxels. The same critical point detection procedure has been followed also for the experiments on neuronal cell counting and cardiac motion estimation.

After critical point localization, the ovarian tissue has been manually segmented in each slice in order to create a mask and filter out the minima retrieved outside the ovarian boundaries (false positives) (see Figure 6.2, central and right image).

In the three data sets, results establish the presence of 19 follicles for patient one, 8 for patient two and 11 for patient three. Manual counting of an expert revealed 17 follicles for patient one and 7 for patient two and 10 for patient 3 ([150], pag. 68, Table 2, patient one, two and three). The computational time for each data set at scale $s = 9$ is less than 5 minutes on a PC with Intel Core TM 2 Duo 2 GHz processor and 4 GB RAM. The same computer has been used to carry out the experiments of neuronal counting and cardiac motion estimation. For each individual the amount of detected follicles indicates relatively good fertility prospects according to [1], especially in the case of patient one. In Figures 6.2 and 6.3 retrieved minima are associated to red dots.

6.3.2 Neuronal cell counting in cerebellum

The cerebellum is a region of the central nervous system located in the so-called hindbrain. It is responsible for motor activity, regulation of muscle tone and also plays an important role in cognitive and language functions in humans. In spite of occupying only around ten per cent of the whole brain volume, the cerebellum contains about fifty percent of all neurons. The number of neurons varies depending on the age and health condition, such as in Alzheimer's disease [171]. Cell density is useful biomarker, however neuronal cell counting is often done manually. This is a time-consuming task where human mistakes cannot be excluded. The eye of the observer will perform increasingly worse at such repetitive tasks. As result, estimations made for large number of cells may become unreliable. For example, the number of Purkinje cells (the principal neurons of the cerebellum) in humans have been estimated to be between 14 and 26 millions [97]. Automatic counting methods are therefore preferable.

Several cell counting methods can be found in the literature. They are mostly based on the cell density distribution in a certain volume and a good guess of the scientist [97, 98, 16, 145, 148, 172]. These methods assume that the cell distribution in the volume of reference stays uniform in the whole region of interest. If this is not the case, such methods will not provide a reliable outcome. The algorithm proposed in this chapter carries out automatic detection and

counting without any assumptions about the cell distribution. Therefore, it may overcome the shortcomings of such techniques and provide more accurate results.

In the experiments we consider two image volumes of neurons labeled with propidium iodide with dimensions $2048 \times 2048 \times 25$ ($164.5 \times 164.5 \times 42.7 \mu\text{m}^3$) and $2048 \times 2048 \times 15$ ($230.3 \times 230.3 \times 32 \mu\text{m}^3$) voxels, respectively. The images were acquired with a confocal microscope. They correspond to two different regions of a 18 days old rat cerebellum. The neuron cell bodies are seen to be roughly spherical (see Figure 6.4). Part of the first image volume shows dense labeling which could not be discriminated into single cells (see right-hand side of the left image in Figure 6.4). As a consequence we could not investigate the whole volume.

Neurons have been retrieved as local minima with the proposed algorithm using scale 9 voxels, after enhancing the blobs in the image volume using a scale-normalized Laplacian operator. Our method retrieved 250 cells in stack 1 and 376 cells in stack 2 (Figure 6.4). A careful visual counting has been carried out on the first 8 slices of stack 1 by an expert neurobiologist, who could recognize 102 neuronal cells. Every slice was carefully inspected in order not to count the same cell twice and not miss smaller cells closer to the bigger ones. This investigation took between 20 and 30 minutes. Although our method has not been optimized for speed purposes it needed roughly 10-15 minutes to detect 112 neurons on the same data subset.

Additionally, we compared the algorithm outcomes with the performance of a simple and fast technique based on the extraction of maxima and minima taking into account the local image intensity [151]. In this method the intensity of each voxel is compared with the intensity of the respective 26 neighbors. Both approaches provided similar results: 250 cells and 376 cells for stack 1 and 2 using the 3D winding number and 271 cells and 361 for stack 1 and 2 using the critical point detector based on intensities.

6.3.3 3D cardiac motion estimation

Cardiac disease may strongly influence the dynamic behavior of the cardiac muscle. Estimation and visualization of the cardiac motion may become an important tool for diagnosis, providing indications of progress of the disease and/or therapy. Optic flow methods measure the apparent velocity of moving patterns in an image sequence. At the beginning of the 1980's Horn and Schunck [76] introduced an optic flow approach based on brightness constancy, estimating the motion by solving the so-called Optic Flow Constraint Equation (OFCE). This technique, however, may not be the preferable choice for

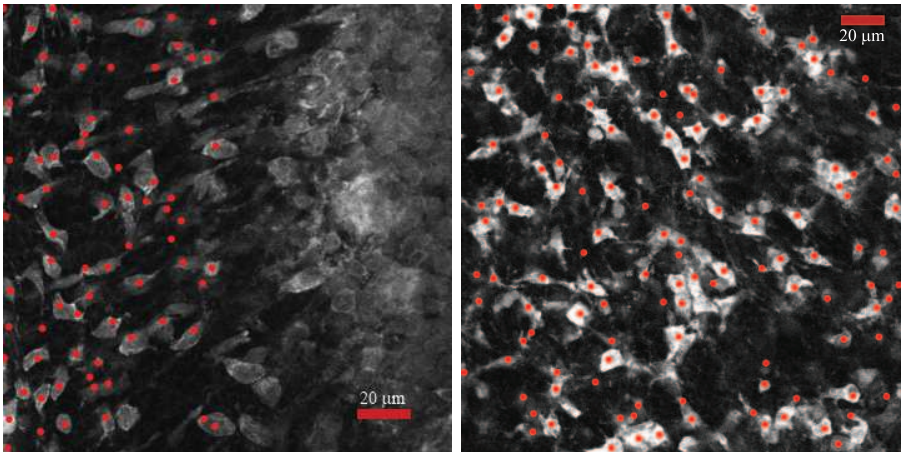


Figure 6.4: Cerebellum cell counting. Left image: A slice of stack 1. Right image: A slice of stack 2. Red dots indicate neurons retrieved by the algorithm.

extracting motion from tagged³ MR images (see Figure 6.5 row 1). For these images the constant intensity assumption does not hold due to tag fading under spin-lattice relaxation time (indicated with T1).

Over the years cardiac motion estimation has become a well-established research field. In the literature, however, there are few optic flow algorithms for 3D cardiac images [19, 127] due to the lack of data sets and sufficient available computational power in the past years.

A 3D motion field exhibits expansions, contractions and twistings of the cardiac tissue, making the results more realistic with respect to the ones provided by a 2D velocity field, where the through-plane motion component is missing. In the experiments we investigate a 3D tagged MR image sequence of a human heart. Cardiac motion is estimated by calculating the velocity of critical points, maxima in this case, which are located at the tag crossings. This optic flow technique is not based on brightness conservation, therefore it can be robustly applied directly on tagged MRI. In chapter 7 a similar 3D motion estimation procedure has been presented. In this case, the critical points have been extracted by a methodology based on zerocrossings.

6.3.3.1 Cardiac image data set

The cardiac data used in the experiments consists of 23 frames with a temporal resolution of 30 *ms*, acquired by a 3D CSPAMM sequence [137]. Each frame

³ The term tags refers to the sinusoidal pattern on the MR images, introduced with the goal to enhance the visualization of the tissue movement [179]

presents 14 slices in the short axis and two different long axis views (Figure 6.5 row 1); the images display a size of 112×112 pixels, with $1 \times 1 \text{ mm}^2$ of pixel resolution. The recorded slices are perpendicular with respect to each other and in the experiments we combine them to obtain a grid (Figure 6.5 row 2, 3 and 4 respectively). Due to sparseness in the slices, we interpolate the 14 slices in each frame in order to obtain image voxels of $112 \times 112 \times 112$ pixels.

6.3.3.2 Calculation of velocity at critical points position and application to cardiac MRI sequence

As already mentioned, we are interested in tracking the critical points (maxima) that occur at the tag crossings of the chessboard-like pattern displayed in row 4 of Figure 6.5. In this case we have a sequence of images and therefore the image intensity is also a function of time, i.e., $L(\mathbf{x}(t), s, t)$ where $\mathbf{x}(t) = (x(t), y(t), z(t))$. The feature points move along with the cardiac tissue, since they are part of the tags. We also mentioned that MR tags fade due to relaxation time T_1 . This property does not influence the vanishing image gradient as long as the tags are visible, and therefore it does not affect the maxima detection at the tag crossings.

By definition, the gradient of an image sequence $L(\mathbf{x}(t), s, t)$ vanishes at critical point positions

$$\nabla L(\mathbf{x}(t), s, t) = 0 \quad (6.20)$$

where ∇ denotes the spatial gradient and s and t represent the scale and time respectively. In order to calculate the velocity at points with local maximum intensity (tag crossings) over time, we differentiate equation (6.20) with respect to time t and apply the chain rule for implicit functions. Hence,

$$\mathbf{V}(t) = \begin{pmatrix} u(t) \\ v(t) \\ w(t) \end{pmatrix} = -HL(\mathbf{x}(t), s, t)^{-1} \frac{\partial(\nabla L(\mathbf{x}(t), s, t)^T)}{\partial t} \quad (6.21)$$

where H represents the spatial Hessian matrix of image L , T indicates transpose, $v(t) = dy/dt$ and $w(t) = dz/dt$ represent the velocity components in horizontal, vertical and through-plane directions. In the experiment described in this section we use a fixed scale s for all frames, for each experiment. In the literature similar optic flow approaches that calculate velocity estimation at feature point location using the Hessian matrix are discussed in [21, 22, 84, 165].

The optic flow algorithm has been applied on a real sequence of 23 tagged volume MR images representing a human beating heart. The images exhibit a resolution of $112 \times 112 \times 112$ voxels and contained tags of 8 voxels wide. The velocity estimation is carried out at the tag crossings, the locations where

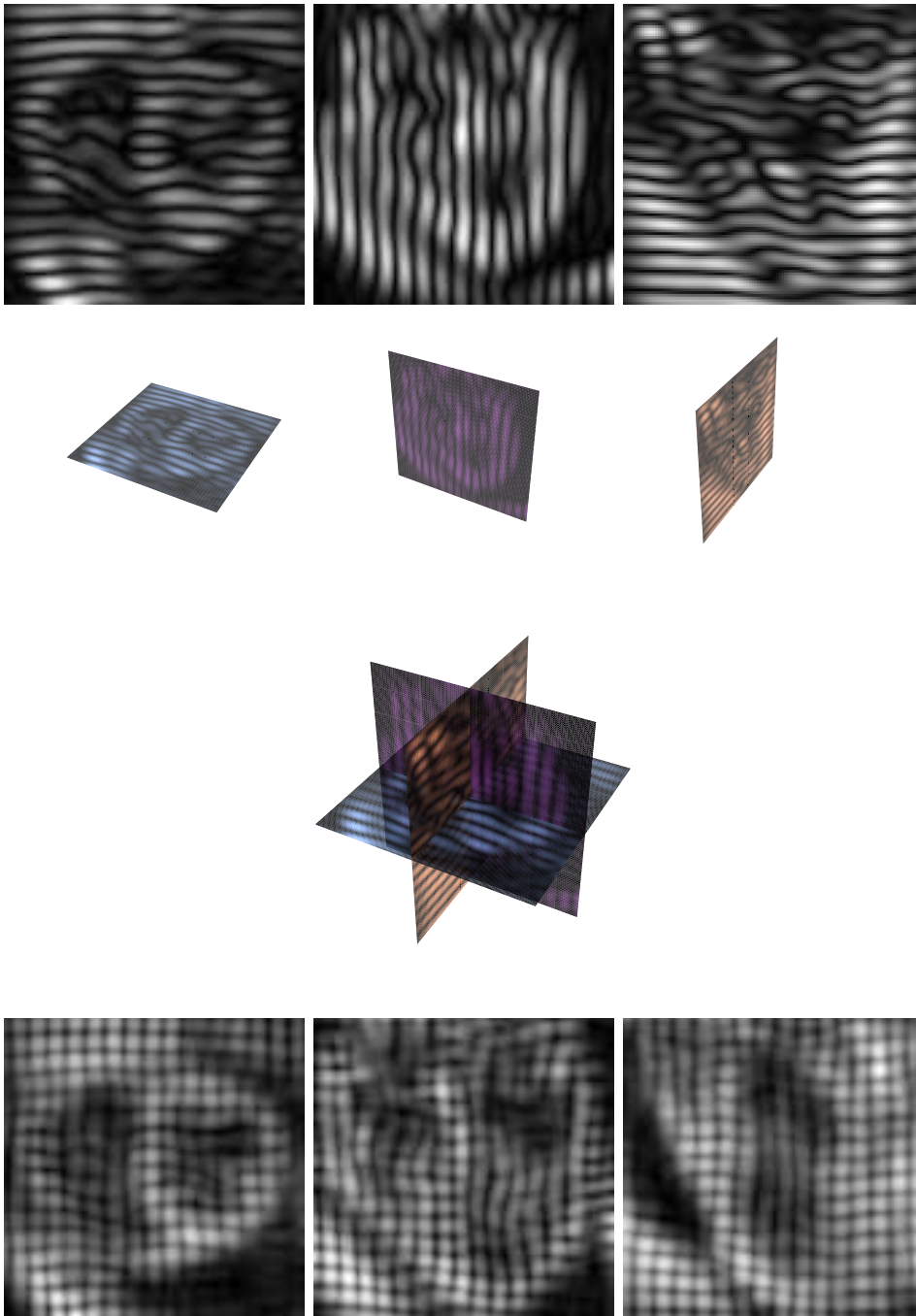


Figure 6.5: Cardiac tagged MR images, frame 3. Row 1 and 2 from left to right: Short axis view with horizontal tags, 2 long axis views with vertical and horizontal tags respectively. Row 3: Combination of the image planes. Row 4 displays the outcome of the combination of image planes. The images exhibit a chessboard pattern.

critical points (maxima) are detected. The computation is carried out at a fixed scale of $s = 3$ voxels and also took roughly 5 to 10 minutes per frame. In Figure 6.6 we show the retrieved motion field for the cardiac data set investigated in the experiments. The images display the left ventricle in phase of contraction. After a qualitative inspection, we notice that the algorithm retrieves a critical point velocity in all three directions, providing valuable information for the quantitative analysis of the patient heart's dynamic behavior.

6.4 Discussion and Conclusion

The work described in this chapter investigates the 3D winding number as an efficient tool to retrieve and classify critical points in volume images. We provide a new formulation of the 3D winding number, simplifying the mathematics and implementation involved with respect to previous work [150]. We discuss the advantages of the proposed technique such as its ability to both locate and classify critical points. We carry out tests on three different real applications (ovarian follicle and neuron counting, and cardiac motion estimation from tagged MRI). We finally discuss the experimental results and we show their qualitative and quantitative reliability.

In our applications we highlight the usefulness of our algorithm in tedious and repetitive operations such as particle counting. The algorithm is able to find blobs and distinguish different cells located next to each other in all data sets. In order to carry out manual counting, the user may either count cells slice by slice or, to speed up the procedure, may perform a 3D projection of the slices and carry out manual counting. In this latest case he may miss certain cells that are close but behind the ones located on the top. On the neuronal data set, for instance, our method detected 4 cells with roughly similar in-plane location (distance less than $3.6 \mu m$ with respect to each other), but different height.

In the experiment with the follicles and neurons we highlight that our algorithm detects a similar amount of follicles and neurons as a trained echographer and neurobiologist, which is already a strong advantage of the proposed method. However, critical point detection has been carried out with a scale chosen globally. A critical point extraction performed at small scale might detect noisy grains (false positives). On the other hand a critical point search carried out at too high scales may miss locations of follicles/neurons that present a smaller structure with respect to the other follicles/neurons in the data set. These problems might be avoided by choosing different scales for follicles/neurons with different sizes. In the future we will carry out experiments in this direction.

In the experiments we assume that the cells have a roughly spherical shape.

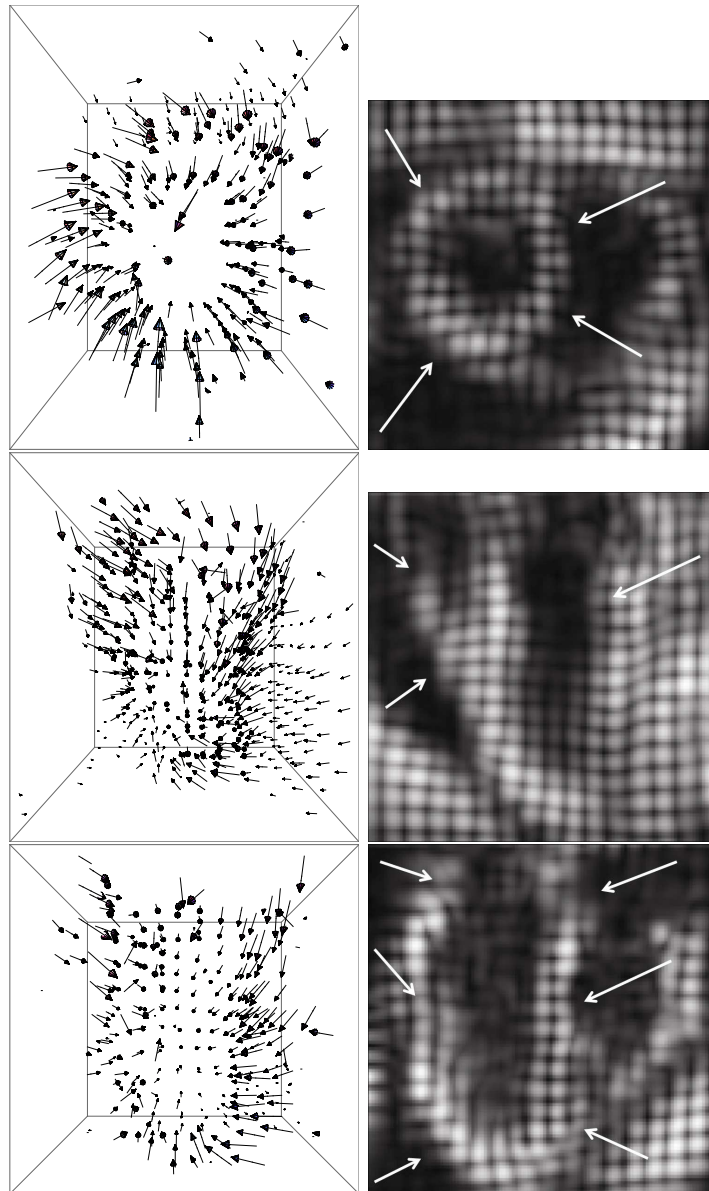


Figure 6.6: Three-dimensional velocity flow field of one frame of the left ventricle in phase of contraction (column 1) under 3 different views and the correspondent cross-sections of the cardiac image volume (column 2). In column 2 the left ventricle is highlighted by white arrows (column 2). Row 1 displays the short axis view, whereas row 2 and 3 show the 2 long axis views. The retrieved 3-dimensional vectors illustrate with accuracy the cardiac motion behavior and overcome shortcomings typical of the 2-dimensional optic flow methods, such as through-plane motion detection.

The neurons, however, have a roughly spherical head (the soma), connected to a tail (the axon). In this case, extremal points were sometimes found in the

axons. The algorithm may therefore count twice the same cell, increasing the error of the final estimation (see Figure 6.4). A way to overcome this problem would be to take into account the geometry of the neuron and remove outcomes coming from the axon. In future research we will tune the algorithm to this specific application.

So far, we have considered the winding number in the context of scalar images. However, other applications of the 3D winding number might be investigated such as detection of singularities in 3D vector fields [112]. These have been proved to be helpful in the visualization of 3D flow fields [101]. In the biomedical context, this could be applied to improve the visualization of blood flow.

In the literature, as we already discussed, other critical point retrieval methodologies are known. Critical points estimation can be carried out by taking into account the local intensity [151], where the intensity of each voxel is compared with that of the respective 26 neighbors. In section 6.3.2 we compare the performance of the 3D winding number algorithm with respect to that of the critical point detection method based on local intensity estimation. Both methods provided similar counting estimation. However, the intensity based method is able to locate only maxima and minima, while the 3D winding number provides also information for saddle points. The 3D winding number algorithm is therefore preferable since it is able to characterize all types of critical points. In the future we will carry out experiments on 3D saddle points detection, which have interesting applications in flow visualization [153, 138]. Finally we will also compare the 3D winding number algorithm with other feature points detectors such as SIFT for 3D applications.

6.5 Acknowledgements

A preliminary implementation of the 3D winding number technique has been carried out by Bart van den Heuvel during his internship supervised by the author of this dissertation.

Nothing is more revealing than movement.

Martha Graham, dancer choreographer

7

A multi-scale feature based optic flow method for 3D cardiac motion estimation

This chapter is partly based on:

Becciu, A., Assen, H.C van, Kozerke, S., Florack, L.M.J., Roode, V.J., Haar Romeny, B.M. ter. A multi-scale feature based optic flow method for 3D cardiac motion estimation. *Second International Conference on Scale Space and Variational Methods in Computer Vision*. Lecture Notes in Computer Science, Vol. 5567, pp. 588-599, 2009.

Abstract

The dynamic behavior of the cardiac muscle is strongly dependent on heart diseases. Optic flow techniques are essential tools to assess and quantify the contraction of the cardiac walls. Most of the current methods however are restricted to the analysis of 2D MR-tagging image sequences: due to the complex twisting motion combined with longitudinal shortening, a 2D approach will always miss the through-plane motion. In this chapter we investigate a new 3D aperture problem free optic flow method to study the cardiac motion by tracking stable multi-scale features such as maxima and minima on 3D tagged MR and sine-phase image volumes. We apply harmonic filtering in the Fourier domain to measure the phase. This removes the dependency of intensity changes of the tagging pattern over time due to T1 relaxation. The regular geometry, the size-changing patterns of the MR-tags stretching and compressing along with the tissue, and the phase- and sine-phase plots represent a suitable framework to extract robustly multi-scale landmark features. Experiments were performed on real and phantom data and the results revealed the reliability of the extracted vector field. Our new 3D multi-scale optic flow method is a promising technique for analyzing true 3D cardiac motion at voxel precision, and free of through-plane artifacts present in multiple-2D data sets.

7.1 Introduction

Cardiac diseases represent one of the major causes of death and disability in the western countries [136]. Symptoms of cardiac illness can be sometimes traced back from the adolescence [6, 115], making a prevention in the childhood a necessity. Cardiac illnesses may influence the deformation and motion of the cardiac walls. A visualization and quantification of cardiac motion may therefore become an important step in the diagnosis, giving indications of the progress of the disease and/or therapy and perhaps even as precursors of cardiac symptoms.

The promise of stem cell injection in the myocardium to instigate cardiac infarct repair, needs quantitative and highly accurate 3D motion and local deformation analysis.

Optic flow is one of the traditional techniques in carrying out motion analysis. It measures the apparent velocity pattern of moving structures in an image sequence. One of the first applications of optic flow methods to tagged MRI was introduced by Dougherty et al. [46]. Florack et al. [57] developed a robust differential technique in a multi-scale framework, whose application to cardiac MR images was presented by Niessen et al. [123, 122] and Suinesiaputra et al. [147]. Van Assen et al. and Florack and Van Assen [163, 59] developed a method based on multiple independent MR tagging acquisitions, removing altogether

the aperture problem, by generating as many equations as unknowns.

In recent years there has been a high increase of computational power and it is becoming more feasible to compute 3-dimensional optic flow fields from MRI data. However, most of the current methods for flow estimation are restricted to the analysis of 2-dimensional MR images, even if the extension to a 3-dimensional approach would be straightforward. In case of cardiac motion estimation, 2-dimensional optic flow techniques capture only expansions, contractions and rotations of the cardiac tissue, missing, however, the twisting motion. A 3-dimensional optic flow technique takes into account all the components of the cardiac motion, providing therefore a more realistic estimation of the heart behaviour. The 3-dimensional version of the so-called optic flow constraint equation already examined in chapter 1, 2, and 3 is:

$$L_x u + L_y v + L_z w + L_t = 0 \quad (7.1)$$

where $u(x, y, z, t)$, $v(x, y, z, t)$ and $w(x, y, z, t) : \mathbb{R}^4 \rightarrow \mathbb{R}$ are now the unknown velocity vectors. An example of 3-dimensional gradient based optic flow estimation has been proposed in 2004 by Barron [19]. He explored the 3-dimensional motion from gated MRI cardiac datasets extending the Horn and Schunck [76] and Lucas and Kanade [111] approaches to three dimensions. This method, however, imposes a constant intensity assumption, which in MRI tagging images does not hold due to the T1 relaxation. Pan et al. [127] instead tracked a cardiac mesh, consisting of a collection of material points extracted from HARP images. A similar approach which makes use of the so-called "slice-following" was performed by Sampath and Prince [140].

In this chapter we investigate cardiac motion from image *volumes* by exploiting point features in Gaussian scale-space. These features are interesting candidates for motion analysis: for those points the aperture problem does not arise and they are detected in a robust framework, which is inspired by findings of the multi-scale structure of the visual system. In the experiments maxima and minima are chosen as feature points and the approach has been tested on an artificial and real image sequence. Outcomes of the proposed technique reveal the reliability of the vector field. In section 7.2 a preprocessing approach is presented. In 7.2.1 and 7.2.2 the image structure of the data and the dataset are discussed. The multi-scale framework used in the experiments and a convenient technique for extracting multi-scale features is explored in section 7.3. There we also present the calculation of a sparse velocity vector field, the dense flow field extension and the angular error measure. Finally in sections 7.4 and 7.5 we describe the experiment, the results, and discuss future directions.

7.2 Materials

7.2.1 Image Structure

In 1988 Zerhouni et al. [179] introduced a tagging method for noninvasive assessment of myocardial motion. The method introduces structure, represented as dark stripes (Figure 7.1 top) on the image aiming to improve the visualization of the intramyocardial motion. The approach was later improved by Axel and Dougherty and Fischer et al. [14, 53], who explored magnetic resonance imaging using spatial modulation of magnetization (SPAMM) and (CSPAMM) respectively. The images, however, suffer from tag fading, making the frames not suitable for optic flow methods based on conservation of brightness. In the harmonic phase (HARP) method [126, 139], MR images are filtered in the spectral domain and this technique overcomes the fading problem by taking into account the spatial phase information from the inverse transform of the filtered images. In our experiments a similar technique was employed using Gabor filters [64]. Three tagged image series with mutually perpendicular tag lines were acquired (Figure 7.1 top) and all but the first harmonic peak was suppressed using a band-pass filter in the Fourier domain (Figure 7.1, row 3). After applying the inverse Fourier Transform, in the filtered images the phase varies periodically from 0 to 2π creating a saw tooth pattern (Figure 7.1 row four, columns 1 to 3). A sine function was applied to the phase images so as to avoid spatial discontinuities in the input due to the saw tooth pattern. A combination of sine phase frames was later employed to produce a grid, from which the feature points (maxima and minima) were retrieved (Figure 7.1 bottom).

7.2.2 Dataset

The experiments were carried out on a 3-dimensional tagged MR image volume sequence of a patient heart. The data were acquired using a 3D CSPAMM sequence [137] developed at ETH Zurich, Switzerland and consisted of 23 frames with a temporal resolution of 30 ms. In each frame, 14 image slices were present for each of three different views (one short axis and two long axis views). The different views were perpendicular with respect to each other (Figure 7.2, row 2) and by combining them, a grid is obtained from which the critical points were retrieved (Figure 7.2, row 3). The images present a resolution of 112×112 pixels and in order to obtain an image volume of $112 \times 112 \times 112$ voxels, linear interpolation through the 14 slices was applied. Here we display again the Figure already shown in 6.3.3.

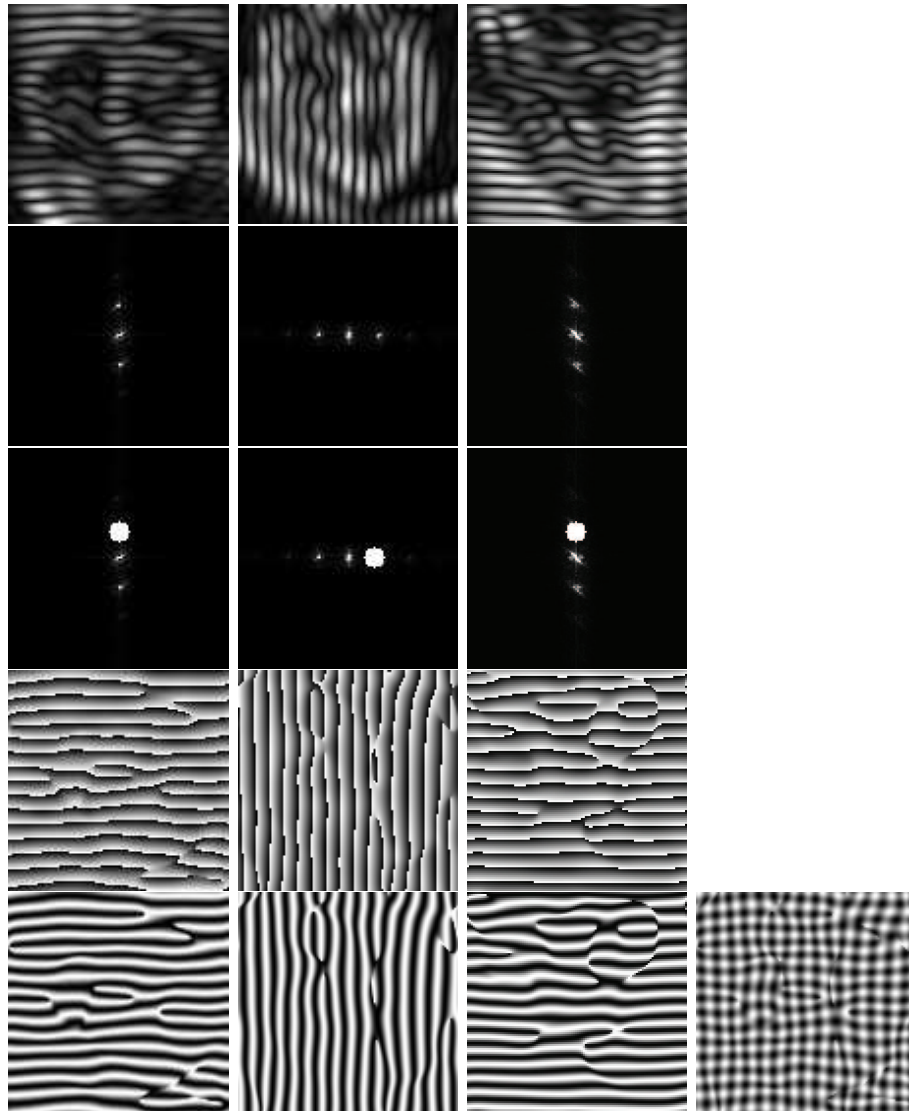


Figure 7.1: Top: cross sections of the cardiac MR tagged images volumes of a patient. From left to right: short axis view (frames present horizontal tags), 2 long axis views (frames present vertical and horizontal tags). Second row: Fourier spectrum of the MR tagged images. Middle: Fourier spectrum with the band-pass filter. Fourth row: phase plots, the phase varies periodically from 0 to 2π creating a saw tooth pattern. Bottom: sine phase images and a slice view of the volume grid obtained by combining three sine phase volumes.

7.3 Method

7.3.1 Scale Space

Scale is one of the most important concepts in human vision. When we look at a scene, we instantaneously view its contents at multiple scale levels. The Gaus-

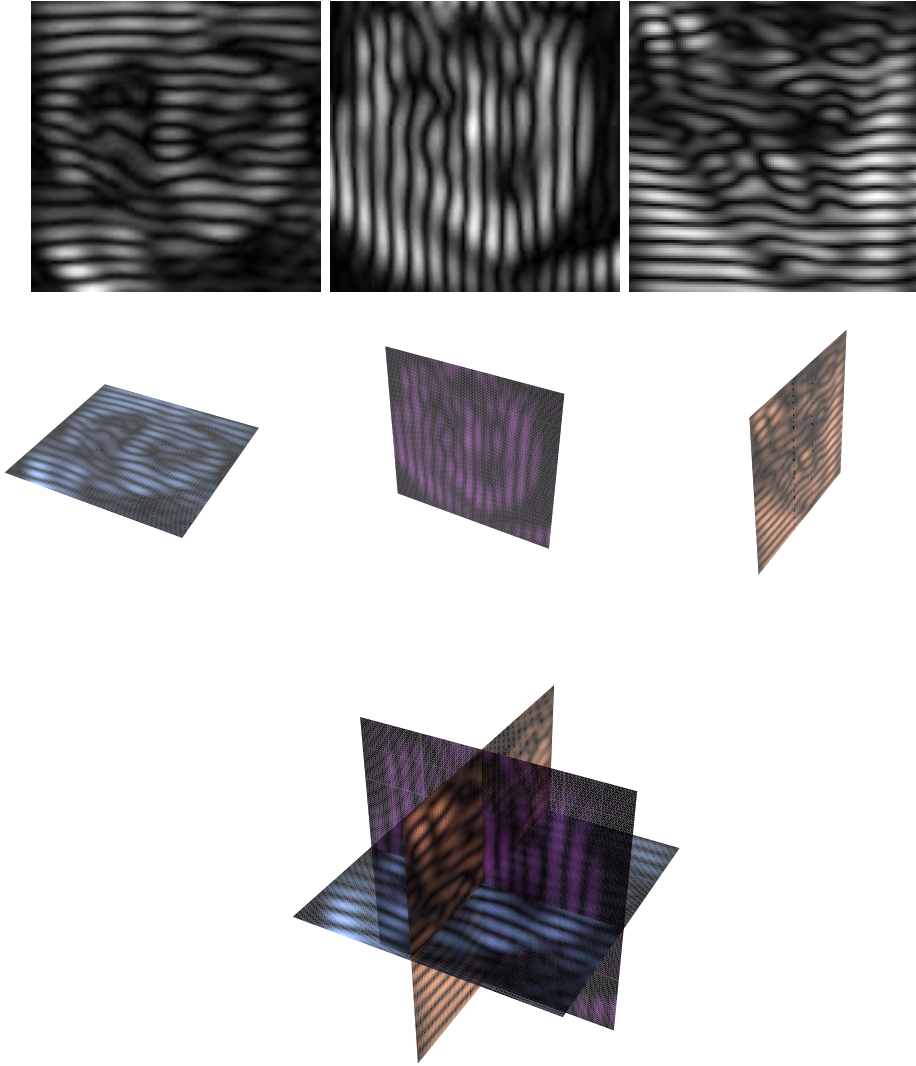


Figure 7.2: Ninth cardiac MR tagged frame. Row 1 and 2 from left to right: short axis view (frames present horizontal tags), 2 long axis views (frames present vertical and horizontal tags). Row 3 illustrates a combination of the image planes.

sian scale-space representation $L(x, y, z, s) \in \mathbb{R}^3 \times \mathbb{R}^+$ of a raw 3-dimensional image $f(x, y, z) \in \mathbb{R}^3$ is defined by the convolution of $f(x, y, z)$ with a Gaussian kernel $\phi(x, y, z, s) \in \mathbb{R}^3 \times \mathbb{R}^+$.

$$L(x, y, z, s) = (f * \phi)(x, y, z, s) \quad (7.2)$$

where $\phi(x, y, z, s) = \frac{1}{(\sqrt{2\pi}s)^3} \exp(-\frac{x^2+y^2+z^2}{2s^2})$. In equation (7.2) x , y and z are the spatial coordinates, whereas $s \in \mathbb{R}^+$ denotes the variance of the Gaussian

kernel (scale). Equation (7.2) provides a blurred version of the image, where the strength of blurring depends on the choice of scale. For an extensive review on scale space see [94, 151, 54, 107].

7.3.2 Critical point detection

Singularities (critical points) induced by the MR tagging pattern are interesting candidates for structural descriptions. In this chapter computation of critical points in scale space is performed with by detecting locations where the gradient of the input image vanishes. Classification of the detected points can be then carried out by determining the sign of the eigenvalues of the Hessian matrix. Locations where the signs of all eigenvalues are positive correspond to locations of local minima; locations where the eigenvalues are all negative, match with locations of local maxima and, finally, eigenvalues with mixed signs provide information about saddle points.

7.3.3 Sparse Velocities of Feature Points and Dense Flow Field

In our experiments given a sequence of frames, we assume that the singularity (feature) points move along with the moving tissue (this is true by construction of the tagging pattern, provided the feature points correctly correspond to the tag crossings). In general, given a point in a sequence of frames defined as $L(x(t), y(t), z(t), t)$, where t indicates the time, the critical points are defined implicitly by a vanishing spatial gradient:

$$\nabla L(x(t), y(t), z(t), t) = 0 \quad (7.3)$$

In order to track the feature points, we derive equation (7.3) with respect to time and apply the chain rule for implicit functions, yielding:

$$\frac{d}{dt} [\nabla L(x(t), y(t), z(t), t)] = \begin{bmatrix} L_{xx}u + L_{xy}v + L_{xz}w + L_{xt} \\ L_{yx}u + L_{yy}v + L_{yz}w + L_{yt} \\ L_{zx}u + L_{zy}v + L_{zz}w + L_{zt} \end{bmatrix} = 0 \quad (7.4)$$

where $\frac{d}{dt}$ is the total time derivative, and where we have dropped space-time arguments on the right hand side (r.h.s.) for simplicity. Equation (7.4) holds only on the location of critical points and can be also written as:

$$\begin{bmatrix} u \\ v \\ w \end{bmatrix} = -HL^{-1} \frac{\partial \nabla L^T}{\partial t} \quad (7.5)$$

where H denotes the Hessian matrix of $L(x(t), y(t), z(t), t)$ and T indicates transpose.

The velocities computed by equation (7.5) represent the flow field at a sparse set of positions. In order to retrieve a dense velocity field, the sparse velocities have been interpolated using homogeneous diffusion interpolation. Given a spatial domain $\Omega \rightarrow \mathbb{R}^3$, the scalar functions $u(x, y, z)$, $v(x, y, z)$ and $w(x, y, z)$ are the horizontal and vertical components of a velocity vector $V : \Omega \rightarrow \mathbb{R}^3$. We know the velocity vectors just at certain positions and we call these vectors $\tilde{V} = \{\tilde{u}, \tilde{v}, \tilde{w}\}$ such that $\tilde{V} : \Omega_s \rightarrow \mathbb{R}^3$, where Ω_s is a finite subset of Ω . We are interested in retrieving a dense set of vectors $V \forall x, y, z \in \Omega$. In order to do so, we minimize the energy function

$$E(u, v) = \int_{\Omega} (\|\nabla u(x, y, z)\|^2 + \|\nabla v(x, y, z)\|^2 + \|\nabla w(x, y, z)\|^2) dx dy dz \quad (7.6)$$

under the constraint $V = \tilde{V} \forall x, y, z \in \Omega_s$. The minimization of equation (7.6) is carried out by employing Euler-Lagrange equations and the resulting expression can be solved with numerical schemes.

7.3.4 Angular Error

The flow vector at certain positions in the image can deviate from the true flow vector at that position in direction and in length. In our assessment we are interested in the movement from one frame to the next. Therefore, we set the time component of the flow vector to 1, yielding a 4-dimensional vector $V = \{u, v, w, 1\}$. The computed vector field has been compared with the ground truth extracted by two artificial sequences described in section 7.4. The assessment has been performed using the so-called average angular error (AAE) introduced by Barron et al. [20]

$$\text{Angular Error} = \arccos\left(\frac{V_t}{\sqrt{u_t^2 + v_t^2 + w_t^2 + 1}} \cdot \frac{V_e}{\sqrt{u_e^2 + v_e^2 + w_e^2 + 1}}\right) \quad (7.7)$$

where V_t is the true vector with spatial component u_t, v_t, w_t and time component 1, whereas V_e is the estimated velocity vector and u_e, v_e, w_e and 1 are its spatial and time components respectively.

7.4 Results

The proposed optic flow method was applied on a real sequence of 23 MR image volumes (Figure 7.1), representing the beating heart of a patient. The images presented a resolution of $112 \times 112 \times 112$ voxels and contained tags of 8 voxels wide. The spatial scale is defined as $\sigma = \sqrt{2s}$ and the experiments

were performed from spatial scale $\sigma = 1$ until scale $\sigma = 3$ at time scale 1. In order to assess the quality of the extracted vector field, one artificial translating sequence of 19 frames was built using the first frame of the sine phase grid image (Figure 7.1, row 5 and column 4). The algorithm was also tested on a more realistic sine phase grid phantom with the same number of frames and with non rigid motion, such as contraction and expansion. Computed vector fields of the translating sequence and the expanding and contracting phantom are depicted in Figure 7.3. The computation of the flow field was performed from frame 8 to frame 11 in order to avoid outliers due to temporal boundary conditions.

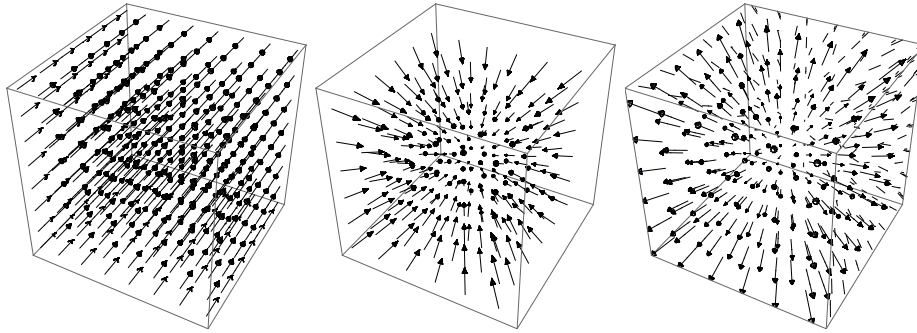


Figure 7.3: Vector fields in the artificial sequence. Vector field of the translating sequence (left) and two frames of the contracting and expanding phantom's vector field(middle and right).

In Table 7.1 the performance of the proposed method, employing scale-space maxima and minima, is displayed. The error measurement was carried out only on locations of retrieved features, in order to assess the reliability of the corresponding velocity. In both sequences, evaluation revealed a high accuracy of the extracted vector fields for both maxima and minima, suggesting to employ a combination of the two retrieved velocities during the interpolation process. The error measure is expressed in degrees. Accuracy of the dense vector field is dependent on the reconstruction method used. As a preliminary study, the homogeneous diffusion interpolation method was applied in this optic flow algorithm.

Feature	Translating Sequence		Nonrigid Motion	
	Maxima	Minima	Maxima	Minima
AAE	5.4×10^{-5}	2.4×10^{-5}	1.0	0.2
Std	2.1×10^{-5}	1.3×10^{-5}	1.4	0.1

Table 7.1: Performance of the proposed optic flow method with different multi-scale feature points. In the experiments the Average Angular Error (AAE) and its standard deviation have been employed as error measurement. The error measure is expressed in degrees. The scales used in the experiment were: spatial scale $\sigma = \{1, 1.3, 1.7, 2.3, 3\}$, time scale 1.

Figure 7.4 depicts plots of average angular error for both phantoms with respect to the scale σ . The graphs reveal that the smallest average angular error was obtained at different scales for different features, highlighting the importance of using a multi-scale approach. In particular for the translating sequence, maxima and minima (Figure 7.4 row 1) obtained best performance at scale $\sigma = 1$ and scale $\sigma = 1.3$ respectively, in case of the contracting and expanding phantom, maxima and minima registered best performance at scale $\sigma = 2.3$ and scale $\sigma = 1.7$ respectively (Figure 7.4 row 2). Figure 7.5 displays the 3-dimensional

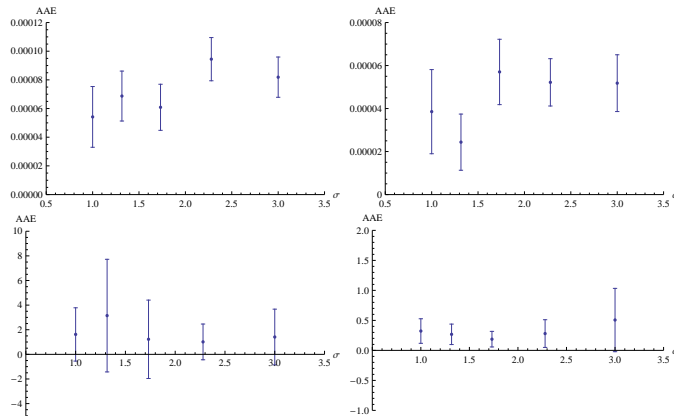


Figure 7.4: Average Angular Errors plots in function of scale. Plots in row 1 display the average angular error for the vector field extracted from the translating sequence. Case maxima, column 1; case minima, column 2. Plots in row 2 depict the average angular error for motion field computed from the contracting and expanding phantom. Case maxima, column 1; case minima, column 2.

sparse vector fields on the 2-dimensional cross-section of the tenth frame of the real cardiac image volume. The heart is in phase of contraction. On the short axis view in row 1 and column 1, the velocity vectors in yellow point not only to the center of the ventricle, but point also down. To the right, the same image is displayed from another perspective showing how the method is able to find through-plane components of the velocity vectors. This is confirmed also by the velocity vectors of the long axis view images in row 2, which point down as well.

7.5 Discussion

In this chapter we investigate a new method to track cardiac motion from 3-dimensional volume images by following the movement of multi-scale singularity points. The computed 3-dimensional vector field exhibits expansions, contractions and twistings of the cardiac tissue (Figure 7.5), and provides more information on motion than velocity fields obtained by a 2-dimensional approach.

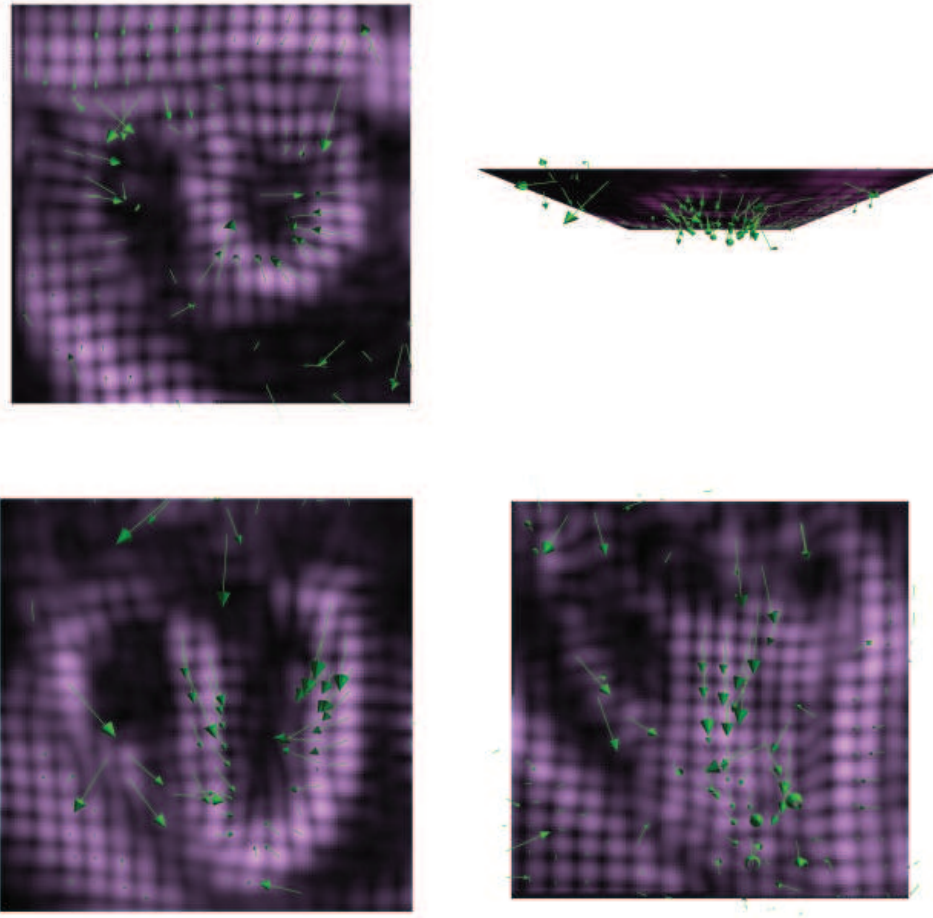


Figure 7.5: 3-dimensional velocity flow field on 2-dimensional cross sections of the cardiac image volume. Short axis (row 1) and two long axis (row 2). The 3-dimensional vectors describe with accuracy the cardiac motion and overcome problems typical of the 2-dimensional optic flow methods, such as through-plane motion detection.

In the latter case, results would only highlight contractions, expansions and rotations of the cardiac muscle, and through-plane motion would not be detected. The method has been assessed using two phantoms, one translating sequence and one expanding and contracting phantom, for which the ground truth was known. In both cases qualitative and quantitative analysis of the results emphasize the reliability of the vector field. The experiments have been carried out using only multi-scale maxima and multi-scale minima. In future tests the algorithm will be assessed also with other multi-scale features points and combinations of those. In the tests the velocity field of our approach has been extracted at fixed scales. The most suitable scale has been chosen taking into account the performance of the method with respect to the ground truth.

In real data, due to continuous deformation of the cardiac walls, the structure changes scale over time, thus, the final results obtained in the assessment may not be optimal. Therefore, it may be interesting to repeat the same experiments by using a more sophisticated scale selection method. Furthermore, the behavior of the cardiac muscle is characterized by twistings and contractions, therefore, interpolation with a term, that takes into account the rotation and the expansion of the vector field may improve the results.

Finally, the retrieved motion field may find also an application in validating mathematical models describing heart deformation. Ubbink et al. [156], for instance, compared three simulations of the cardiac muscle, illustrating how the orientation of modeled myofibers plays an important role in the computation of the final strain. A validation of these methods might be carried out by comparing the simulated strain with a ground truth strain calculated from the extracted optic flow field using real data.

So eine Arbeit wird eigentlich nie fertig, man muss sie für fertig erklären, wenn man nach Zeit und Umständen das Mögliche getan hat.

J. W. von Goethe, Italienische Reise, 1787



Conclusions and future research

8.1 Feature based estimation of myocardial motion from tagged MR images (Summary)

In the past few years we witnessed an increase in mortality due to cancer relative to mortality due to cardiovascular diseases. In 2008, the Netherlands Statistics Agency reports that 33.900 people died of cancer against 33.100 deaths due to cardiovascular diseases, making cancer the number one cause of death in the Netherlands [33]. Even if the rate of people affected by heart diseases is continually rising, they "simply don't die of it", according to the research director Prof. Mat Daemen of research institute CARIM of the University of Maastricht [50]. The reason for this is the early diagnosis, and the treatment of people with identified risk factors for diseases like ischemic heart disease, hypertrophic cardiomyopathy, thoracic aortic disease, pericardial (sac around the heart) disease, cardiac tumors, pulmonary artery disease, valvular disease, and congenital heart disease before and after surgical repair.

Cardiac imaging plays a crucial role in the early diagnosis, since it allows the accurate investigation of a large amount of imaging data in a small amount of time. Moreover, cardiac imaging reduces costs of inpatient care, as has been shown in recent studies [77]. With this in mind, in this work we have provided several tools with the aim to help the investigation of the cardiac motion.

In chapters 2 and 3 we have explored a novel variational optic flow methodology based on multi-scale feature points to extract cardiac motion from tagged MR images. Compared to constant brightness methods, this new approach exhibits several advantages. Although the intensity of critical points is also influenced by fading, critical points do retain their characteristic even in the presence of intensity changes, such as in MR imaging. In an experiment in section 5.4 we have applied this optic flow approach directly on tagged MR images. A visual inspection confirmed that the extracted motion fields realistically depicted the cardiac wall motion. The method exploits also the advantages from the multi-scale framework. Because sparse velocity formulas 2.9, 3.7, 6.21, and 7.5 provide a number of equations equal to the number of unknowns, the method does not suffer from the aperture problem in retrieving velocities associated to the critical points.

In chapters 2 and 3 we have moreover introduced a smoothness component of the optic flow equation described by means of covariant derivatives. This is a novelty in the optic flow literature. Many variational optic flow methods present a smoothness component that penalizes for changes from global assumptions such as isotropic or anisotropic smoothness. In the smoothness term proposed deviations from a predefined motion model are penalized.

Moreover, the proposed optic flow equation has been decomposed in rotation-

free and divergence-free components. This decomposition allows independent tuning of the two components during the vector field reconstruction. The experiments and the Table of errors provided in 3.8 showed that the combination of the smoothness term, influenced by a predefined motion model, and the Helmholtz decomposition in the optic flow equation reduces the average angular error substantially (20%-25%) with respect to a similar technique that employs only standard derivatives in the smoothness term.

In section 5.3 we extracted the motion field of a phantom of which we know the ground truth of and compared the performance of this optic flow method with the performance of other optic flow methods well known in the literature, such as the Horn and Schunck [76] approach, the Lucas and Kanade [111] technique and the tuple image multi-scale optic flow constraint equation of Van Assen et al. [163]. Tests showed that the proposed optic flow methodology provides the smallest average angular error ($AAE = 3.84$ degrees) and $L2$ norm = 0.1.

In this work we employed the Helmholtz decomposition also to study the cardiac behavior, since the vector field decomposition allows to investigate cardiac contraction and cardiac rotation independently. In chapter 4 we carried out an analysis of cardiac motion of ten volunteers and one patient where we estimated the kinetic energy for the different components. This decomposition is useful since it allows to visualize and quantify the contributions of each single vector field component to the heart beat. Local measurements of the kinetic energy have also been used to detect areas of the cardiac walls with little movement. Experiments on a patient and a comparison between a late enhancement cardiac image and an illustration of the cardiac kinetic energy on a bull's eye plot illustrated that a correspondence between an infarcted area and an area with very small kinetic energy exists.

With the aim to extend in the future the proposed optic flow equation to a 3D approach, in chapter 6 we investigated the 3D winding number approach as a tool to locate critical points in volume images. We simplified the mathematics involved with respect to a previous work [150] and we provided several examples and applications such as cardiac motion estimation from 3-dimensional tagged images, follicle and neuronal cell counting.

Finally in chapter 7 we continued our investigation on volume tagged MR images, by retrieving the cardiac motion field using a 3-dimensional and simple version of the proposed optic flow equation based on standard derivatives. We showed that the retrieved motion fields display the contracting and rotating behavior of the cardiac muscle. We moreover extracted the through-plane component, which provides a realistic illustration of the vector field and is missed by 2-dimensional approaches.

8.2 Remarks and future research

In this section we present a non exhaustive list of future directions opened by this work.

Spatio-temporal smoothing term. The optic flow algorithm proposed in chapter 2 and 3 exhibits a smoothness component consisting of spatial derivatives only. Spatio-temporal smoothness constraints have been already investigated in the literature [27, 169], and provide better performance with respect to techniques with a spatial smoothness constraint only. In the future we will tackle also this issue. However, if we extend the smoothness term in the temporal direction, we regularize with respect to a third direction (time), therefore increasing the computational time. To avoid high computational costs, in the future the algorithm should be re-implemented in programmable hardware like field-programmable gate arrays (FPGA).

Extension of the new optic flow technique to 3-dimensional tagged cardiac MR image sequences. As already mentioned in chapter 7, recently we witnessed an increase in computational power and it is already possible (even if it is not common) to obtain 3-dimensional tagged MR images. In the future we will extend the technique proposed in chapter 3 also for these images.

Application to echo-cardiography images (speckle tracking). In our motion estimation algorithm we extract velocity features from a sparse set of critical points, then we reconstruct a dense motion field minimizing an energy functional. We believe that the feature point tracking procedure may also be suitable for speckle tracking in echo-cardiography. In the future we will carry out experiments in this direction.

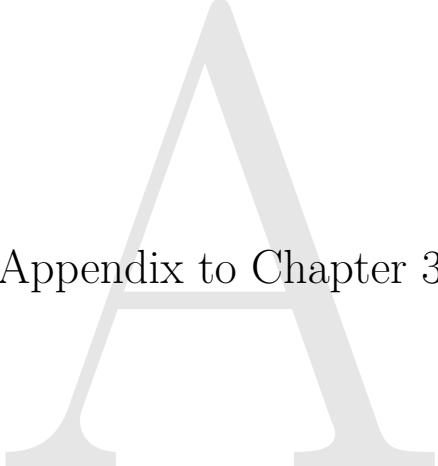
Application to general image sequences. Besides having shown that our optic flow method is suitable for cardiac tagged MR images, this technique can be applied also to more generic image sequences. In the future we will tackle this issue including the assessment of performance with image sequences like the well known *Yosemite* sequence. A comparison with the results of the state of the art optic flow algorithms will be also carried out.

Quantification of cardiac motion parameters. Calculation of the local kinetic energy in chapter 4 shows promising results and encourages to pursue the future studies in this direction. However, we tested our method only on one patient and we can not establish whether the technique provides reliable results for different cases. In order to overcome this, we need to investigate the cardiac behavior of a large population of patients with several types of heart diseases and compare the outcomes with the results obtained from different parameters, such as strain, and from different protocols such as late-enhancement MRI, or

modalities like Tissue Doppler Imaging with Ultrasound.

Saddles computation. In chapter 6 we extensively discussed the benefits of the 3D winding number, as a tool that characterizes all critical points. However, in the chapter we restricted our investigation only to the extraction of 3-dimensional maxima and minima. In the future we will investigate 3-dimensional saddles, which play an important role in the flow field visualization [138, 153].

Possible new applications. Finally, the methodologies explored in this thesis find application in several areas of cardiac medicine. An example is the regenerative medicine. One may for example quantify the motion and study the cardiac behavior of subjects that suffered from myocardial infarction and have been treated with stem cell therapy [25, 44, 159] in a longitudinal study.



Appendix to Chapter 3

This appendix is based on selected sections of:

Duits R., Janssen B.J., Becciu A. A variational approach to cardiac motion estimation based on covariant derivatives and multi-scale Helmholtz decomposition. Submitted to the international journal *Quarterly of applied mathematics*

Duits, R., Becciu, A., Janssen, B.J, Florack, L.M.J., Assen, H.C. van, Haar Romenij, B.M. ter. Cardiac motion estimation using covariant derivatives and Helmholtz decomposition. *CASA Report* No. 10-31, Eindhoven: Technische Universiteit Eindhoven, 40 pp.(2010)

A.1 Covariant derivatives

Consider the vector¹ bundle

$$E := (\Omega \times \mathbb{R}^2, \pi, \Omega)$$

where $\Omega \subset \mathbb{R}^d$, $d = 2, 3$, is the image domain, where the fundamental projection $\pi : \Omega \times \mathbb{R}^2 \rightarrow \Omega$ is given by

$$\pi(x, y, v_1, v_2) = (x, y), \quad (x, y, v_1, v_2) \in \Omega \times \mathbb{R}. \quad (\text{A.1})$$

where respectively v_1 and v_2 denote the velocity in x and y direction.

A fiber in this vector bundle is the two dimensional vector space $\pi^{-1}(x, y) = \{(x, y, v_1, v_2) \mid v_1, v_2 \in \mathbb{R}\}$ ². A section σ in the vector bundle is the surface which basically represents the graph of some vector-valued function $v : \Omega \rightarrow \mathbb{R}^2$:

$$\begin{aligned} \sigma_{\mathbf{v}}(x, y) = \\ \{(x, y, v_1, v_2) \in \Omega \times \mathbb{R}^2 \mid v_1 = v_1(x, y), v_2 = v_2(x, y)\}, \\ \mathbf{v} = (v^1, v^2)^T, \end{aligned}$$

note that $\pi \circ \sigma_{\mathbf{v}} = \text{id}_{\Omega}$, i.e. $(\pi \circ \sigma_{\mathbf{v}})(x, y) = (x, y)$ for all $(x, y) \in \Omega$, (i.e. σ_v is a section in a vector bundle).

Now that we have set the very basic ingredients for the vector bundle (E, π, Ω) . We stress that we do *not* work in the much more common tangent bundle setting $(\Omega \times T(\Omega), \tilde{\pi}, \Omega)$ where sections are vector fields and where $\tilde{\pi}(x, y, \mathbf{v}(x, y)) = (x, y)$. Consequently, we have to rely on the more general concept of covariant derivatives in vector bundle rather than the covariant derivative in the tangent bundle, which we explain next.

A.1.1 A Tool from Differential Geometry: Connections on the Vector Bundle E

A connection on a vector bundle is by definition a mapping $D : \Gamma(E) \rightarrow \mathcal{L}(\Gamma(T(\Omega)), \Gamma(E))$ from the space of sections in the vector bundle $\Gamma(E)$ to the space of linear mappings $\mathcal{L}(\Gamma(T(\Omega)), \Gamma(E))$ from the space of vector fields on Ω denoted by $\Gamma(T(\Omega))$ into the space of sections $\Gamma(E)$ in the vector bundle E

¹In previous work we called $(\mathbb{R}^2 \times \mathbb{R}^+, \pi, \Omega)$ a vector bundle, but formally speaking this is not right \mathbb{R}^+ is not a vector space.

²Here we stress that we do *not* assume that this two dimensional vector space is the tangent space $T_{(x,y)}(\Omega)$, since our vector bundle is not a tangent bundle

such that

$$\begin{aligned}
D_{\mathbf{v}+\mathbf{w}}\sigma &= D_{\mathbf{v}}\sigma + D_{\mathbf{w}}\sigma , \\
D_{f\mathbf{v}}\sigma &= fD_{\mathbf{v}}\sigma , \\
D_{\mathbf{v}}(\sigma + \tau) &= D_{\mathbf{v}}\sigma + D_{\mathbf{v}}\tau , \\
D_{\mathbf{v}}(f\sigma) &= \mathbf{v}(f)\sigma + fD_{\mathbf{v}}\sigma
\end{aligned} \tag{A.2}$$

for all vector fields $\mathbf{v} = \sum_{i=1}^2 v^i \partial_{x^i}$, $\mathbf{w} = \sum_{i=1}^2 w^i \partial_{x^i} \in \Gamma(T(\Omega))$ (i.e. sections in tangent bundle $T(\Omega)$) and all $f \in C^\infty(\Omega, \mathbb{R})$ and all sections $\sigma \in \Gamma(E)$ in the vector bundle E . Note that we used the common short notation $D_{\mathbf{v}}\sigma = (D\sigma)(\mathbf{v})$. One can verify that (A.2) implies that

$$\begin{aligned}
((D\sigma_{\mathbf{v}})(X))(\mathbf{c}(t)) &= \\
D(v^1\sigma_1 + v^2\sigma_2)(X)(\mathbf{c}(t)) &= \\
\sum_{j=1}^2 X|_{\mathbf{c}(t)}(v^j)\sigma_j + & \\
\sum_{j=1}^2 \sum_{i=1}^2 v^j(\mathbf{c}(t))\dot{c}^i(t) (D_{\partial_{x^i}}\sigma_j)(\mathbf{c}(t)) &\in \Gamma(E),
\end{aligned} \tag{A.3}$$

where $\sigma_1(x, y) = (x, y, 1, 0)$ and $\sigma_2(x, y) = (x, y, 0, 1)$ denote the unit sections in x and y -direction and where $X|_{\mathbf{c}(t)} = \sum_{i=1}^2 \dot{c}^i(t) \partial_{x^i}|_{\mathbf{c}(t)}$ denotes a vector field on Ω tangent to a curve $\mathbf{c} : (0, 1) \rightarrow \Omega$ is a smooth curve in the image domain $\Omega \subset \mathbb{R}^2$, with $\dot{\mathbf{c}}(t) = \frac{d}{dt}\mathbf{c}(t)$ and components $\mathbf{c}^i(t) = \langle dx^i, \dot{\mathbf{c}}(t) \rangle$ obtained by the dual basis vector fields dx^1, dx^2 in the co-tangent bundle $T^*(\Omega)$.

Formula (A.3) tells us that the connection is entirely determined by its output on the (constant) basis sections σ_j and the basis vector fields ∂_{x^i} , i.e. D is uniquely determined by $\{D_{\partial_{x^i}}\sigma_j\}_{i,j=1,2}$. Now for each $i, j = 1, 2$ this output $D_{\partial_{x^i}}\sigma_j$ is a section and consequently there exist unique functions $\Gamma_{ij}^k : \Omega \rightarrow \mathbb{R}$ (Christoffel-symbols) such that

$$(D_{\partial_{x^i}}\sigma_j)(\mathbf{c}(t)) = \Gamma_{ij}^k(\mathbf{c}(t))\sigma_k .$$

A.1.2 Covariant derivatives on the Vector Bundle E induced by gauge fields.

In this article we restrict ourselves to the diagonal case (no interaction between the components)

$$\Gamma_{ij}^k = A_i^k \delta_j^k , \text{ with } A_i^k := \Gamma_{ik}^k, \tag{A.4}$$

We impose this restriction for pragmatic reasons: It keeps the implementation relatively simple. Moreover, this choice is a straightforward generalization of our previous work on reconstruction of scalar valued functions using covariant derivatives [83]. Although this choice does not affect the rules for covariant derivatives on a vector bundle (A.2), this restriction may not be a necessary.

Consequently, we have

$$\begin{aligned}
(Dv^1\sigma_1)(\partial_{x^i}) &= (\partial_{x^i}v^1 + A_i^1 v^1) \sigma_1, \text{ for } i = 1, 2. \\
D_{\partial_{x^i}}\sigma_{\mathbf{v}} &= (D\sigma_{\mathbf{v}})(\partial_{x^i}) = \\
&(\partial_{x^i}v^1 + A_i^1 v^1) \sigma_1 + (\partial_{x^i}v^2 + A_i^2 v^2) \sigma_2 \\
\text{with } \mathbf{v} &= \sum_{i=1}^2 v^i \sigma_i \in \Gamma(E)
\end{aligned} \tag{A.5}$$

Now the next step is to choose $\{A_i^j\}$ such that an a priori given section $\sigma_{\mathbf{h}}$ (a so-called *gauge-field*, [83])

$$\begin{aligned}
(x, y) &\mapsto \sigma_{\mathbf{h}}(x, y) \text{ with } \sigma_{\mathbf{h}}(x, y) = \\
&(x, y, h^1(x, y), h^2(x, y)), \mathbf{h} = (h^1, h^2)^T,
\end{aligned}$$

is “invisible” with respect to the covariant derivative, i.e. we must solve for

$$\begin{aligned}
(D\sigma_{\mathbf{h}})(\partial_{x^i}) &= 0 \text{ for all } i = 1, 2 \Leftrightarrow \\
(\partial_{x^i}h^1 + A_i^1 h^1) \sigma_1 + (\partial_{x^i}h^2 + A_i^2 h^2) \sigma_2 &= \\
0 \sigma_1 + 0 \sigma_2 \text{ for all } i = 1, 2 \Leftrightarrow \\
A_i^j &= -\frac{\partial_{x^i}h^j}{h^j} \text{ for all } i, j = 1, 2,
\end{aligned} \tag{A.6}$$

so that the covariant derivative $D^{\mathbf{h}}$ induced by gauge-field $\sigma_{\mathbf{h}} \in \Gamma(E)$ is given by

$$\begin{aligned}
(D_{\partial_{x^i}}^{\mathbf{h}}\sigma_{\mathbf{v}})(\mathbf{x}) &= \\
(\partial_{x^i}v^1(\mathbf{x}) - \frac{\partial_{x^i}h^1(\mathbf{x})}{h^1(\mathbf{x})}v^1(\mathbf{x})) \sigma_1 + \\
(\partial_{x^i}v^2(\mathbf{x}) - \frac{\partial_{x^i}h^2(\mathbf{x})}{h^2(\mathbf{x})}v^2(\mathbf{x})) \sigma_2 &= \\
((\partial_{x^i})^{h_1})(\mathbf{x}) \sigma_1 + ((\partial_{x^i})^{h_2})(\mathbf{x}) \sigma_2.
\end{aligned}$$

Now that we introduced everything in a formal differential geometry setting we will simplify our notations. In the remainder of this article, we will identify sections $\sigma_{\mathbf{v}}$ in E with the corresponding vector-functions $\mathbf{v} : \Omega \rightarrow \mathbb{R}^2$, and for all $\mathbf{x} \in \mathbb{R}^2$,

$$\begin{aligned}
\sigma_{\mathbf{v}=v^1, v^2}(\mathbf{x}) &= (\mathbf{x}, v^1(\mathbf{x}), v^2(\mathbf{x})) \Leftrightarrow \mathbf{v}(\mathbf{x}) = (v^1(\mathbf{x}), v^2(\mathbf{x}))^T \\
\sigma_1 &= (0, 0, 1, 0) \Leftrightarrow \mathbf{e}_1 := (1, 0)^T, \\
\sigma_2 &= (0, 0, 0, 1) \Leftrightarrow \mathbf{e}_2 := (0, 1)^T.
\end{aligned} \tag{A.7}$$

and briefly write $\partial_{x^i}^{\mathbf{h}}\mathbf{v} : \Omega \rightarrow \mathbb{R}^2$ for the vector function corresponding to the section $D_{\partial_{x^i}}^{\mathbf{h}}\sigma_{\mathbf{v}} : \Omega \rightarrow E$, i.e. :

$$(x, y, \partial_{x^i}^{\mathbf{h}}\mathbf{v}(x, y)) = (D_{\partial_{x^i}}^{\mathbf{h}}\sigma_{\mathbf{v}})(x, y).$$

where we applied short notation $\partial_{x^i}^{\mathbf{h}\mathbf{v}} := D_{\partial_{x^i}}^{\mathbf{h}} \sigma_{\mathbf{v}}$.

Note that covariant derivatives are invariant under sign-transitions.

$$A_i^j = -\frac{\partial_{x^i} h^j}{h^j} = -\frac{\partial_{x^i} |h^j|}{|h^j|} \text{ for all } i, j = 1, 2. \quad (\text{A.8})$$

The covariant Laplacian can be explicitly expressed in components

$$\begin{aligned} (D^{\mathbf{h}})^* D^{\mathbf{h}\mathbf{v}} &= \sum_{j=1}^2 \sum_{i=1}^2 \left((\partial_{x^i}^{h^j})^* \partial_{x^i}^{h^j} v^j \right) \mathbf{e}_j, \\ &= \sum_{j=1}^2 \left(-\Delta v^j + \frac{\Delta h^j}{h^j} v^j \right) \mathbf{e}_j \end{aligned} \quad (\text{A.9})$$

where we recall our identifications (A.7). With respect to this covariant Laplacian we recall that

$$(\partial_{x^i})^{h^j} v^j = \partial_{x^i} v^j - \frac{\partial h^j}{\partial x^i} v^j \quad (\text{A.10})$$

so that its \mathbb{L}_2 -adjoint defined by

$$\left((\partial_{x^i})^{h^j} v^j, \phi \right)_{\mathbb{L}_2(\Omega)} = \left(\phi, \left((\partial_{x^i})^{h^j} \right)^* v^j \right)_{\mathbb{L}_2(\Omega)},$$

for all $\phi \in \mathbb{L}_2(\Omega)$ is given by

$$\left((\partial_{x^i})^{h^j} \right)^* v^j = -\partial_{x^i} v^j - \frac{\partial_{x^i} h^j}{h^j} v^j. \quad (\text{A.11})$$

If we compare the adjoint covariant derivative to the covariant derivative we see that the multiplier part is maintained whereas the derivative-part contains an extra minus sign. So that indeed one finds the fundamental formula:

$$\begin{aligned} \sum_{i=1}^2 \left(\partial_{x^i}^{h^j} \right)^* \partial_{x^i}^{h^j} v^j &= \\ \sum_{i=1}^2 -\frac{\partial}{\partial x^i} \left(\frac{\partial}{\partial x^i} \right)^{h^j} v^j - \frac{\frac{\partial h^j}{\partial x^i} \left(\frac{\partial}{\partial x^i} \right)^{h^j} v^j}{h^j} &= \\ \sum_{i=1}^2 -\frac{\partial}{\partial x^i} \left(\frac{\partial v^j}{\partial x^i} - \frac{\partial h^j}{\partial x^i} \frac{v^j}{h^j} \right) - \frac{\frac{\partial v^j}{\partial x^i} \left(\frac{\partial v^j}{\partial x^i} - \frac{\partial h^j}{\partial x^i} \frac{v^j}{h^j} \right)}{h^j} &= \\ -\Delta v^j + \frac{\Delta h^j}{h^j} v^j. & \end{aligned} \quad (\text{A.12})$$

Now, that we have introduced the covariant Laplacian we mention two preliminary issues that directly arise from (A.12) and which will be addressed in the remainder of this article.

Remark 1. *At first sight the covariant derivatives and their associated (inverse) Laplacian, seem to be numerically ill-posed as the gauge-field components should not vanish, likewise in the previous works [66, 83, 21]. However, the crucial scaling property of covariant derivatives, Eq. (3.33) allows us to*

scale away from 0 and numerical singular behavior is avoided by adding a tiny $0 < \delta \ll 1$ in the computation of

$$\frac{\Delta h^j(x, y)}{h^j(x, y)} \approx \frac{\Delta h^j(x, y) + \delta}{h^j(x, y) + \delta} = -\Delta(-\log |h^j(x, y) + \delta|) + \|\nabla \log |h^j(x, y) + \delta|\|^2.$$

In [47], we investigate the fundamental properties of the self-adjoint covariant laplacian, we show how the manifest stability of our algorithms, depends on the choice of gauge field, and we explain, how the Dirichlet kernel of the coercive covariant Laplacian behaves similar to the Dirichlet kernel of the regular Laplacian (with the advantage that it locally adapts to concave and convex behavior of the gauge function).

Remark 2. Covariant derivatives of sections (vectorvalued functions) in the vector bundle E given by (A.5) in general do not coincide with covariant derivatives of sections (vector fields) in $((\Omega, T(\Omega)), \tilde{\pi}, \Omega)$. The components in (A.10) are coordinate dependent and not compatible with respect to orthogonal coordinate transformations (such as rotations). This incompatibility is due to our restriction (A.4) is investigated in [47].

A.2 The Euler-Lagrange equations for Tikhonov regularized optic flow reconstruction in covariant derivatives

The Euler-Lagrange equations for the unique minimizer of (3.44) are derived by

$$\lim_{\epsilon \rightarrow 0} \frac{\mathcal{E}^{\lambda, \mathbf{h}^k, \mathbf{d}^k}(\mathbf{v}^k + \epsilon \boldsymbol{\delta}) - \mathcal{E}^{\lambda, \mathbf{h}^k, \mathbf{d}^k}(\mathbf{v}^k)}{\epsilon} = 0$$

which is supposed to hold for all infinitely smooth perturbations that are compactly within the interior of Ω , i.e. $\boldsymbol{\delta} \in \mathcal{D}(\Omega)$. Now computations in the general continuous Tikhonov regularization framework yield $\forall \boldsymbol{\delta} \in \mathcal{D}(\Omega)$

$$\boxed{\begin{aligned} 2((-\lambda (D\mathbf{h}^k)^* D\mathbf{h}^k) \mathbf{v}^k + \mathcal{S}_k^* \Lambda_k \mathcal{S}_k \mathbf{v}^k - \mathcal{S}_k^* \mathbf{d}^k, \boldsymbol{\delta}) &= 0 \\ \Leftrightarrow \\ (-\lambda (D\mathbf{h}^k)^* D\mathbf{h}^k + \mathcal{S}_k^* \Lambda_k \mathcal{S}_k) \mathbf{v}^k &= \mathcal{S}_k^* \Lambda_k \mathbf{d}^k \end{aligned}} \quad (\text{A.13})$$

where $\mathcal{S}_k : \mathbf{L}_2(\Omega) \rightarrow \mathbb{R}^{2 \times N_B}$ is given by

$$\begin{aligned} (\mathcal{S}_k \mathbf{v}^k)(q) &= (\phi_k^q, \mathbf{v}^k) := \\ &(\phi_k^q, v^{k,1})_{\mathbf{L}_2(\Omega)} \mathbf{e}_1 + (\phi_k^q, v^{k,2})_{\mathbf{L}_2(\Omega)} \mathbf{e}_2. \end{aligned}$$

and where $\Lambda_k \in \mathbb{R}^{N_B \times N_B}$ is the diagonal matrix consisting of the corresponding feature weights:

$$\Lambda_k = \text{diag}\{(w_q^k)_{q=1}^{N_B}\}.$$

Recall that N_B denotes the number of features (the number of extremal branches in our scale space representation, recall (3.4.1)). Note that the adjoint $\mathcal{S}_k^* : \mathbb{R}^{2 \times N_B} \rightarrow \mathbf{L}_2(\Omega)$ operator for each fixed discrete time $k \in \mathbb{N}$ is defined by

$$(\mathcal{S}_k^* \Phi, \mathbf{v}^k)_{\mathbf{L}_2(\Omega)} = (\Phi, \mathcal{S}_k \mathbf{v}^k)_{\mathbb{R}^{2 \times N_B}},$$

or more explicitly by

$$\begin{aligned} & \int_{\Omega} ((\mathcal{S}_k^* \Phi)(\mathbf{x}))^1 v^{k,1}(\mathbf{x}) + ((\mathcal{S}_k^* \Phi)(\mathbf{x}))^2 v^{k,2}(\mathbf{x}) \, d\mathbf{x} = \\ & \sum_{j=1}^2 \sum_{q=1}^{N_B} (\Phi(q))^j (\mathcal{S}_k \mathbf{v}^k(q))^j = \sum_{j=1}^2 \sum_{q=1}^{N_B} (\phi_k^q, v^{k,j}) (\Phi(q))^j = \\ & \int_{\Omega} \left(\sum_{j=1}^{N_B} \mathbf{e}_j \left(\sum_{q=1}^{N_B} (\Phi(q))^j \phi_k^q(\mathbf{x}) \right) \right) \cdot \mathbf{v}^k(\mathbf{x}) \, d\mathbf{x} \end{aligned}$$

so that the adjoint is simply given by

$$(\mathcal{S}_k^* \Phi)(\mathbf{x}) = \sum_{j=1}^2 \mathbf{e}_j \left(\sum_{q=1}^{N_B} (\Phi(q))^j \phi_k^q(\mathbf{x}) \right)$$

This allows to write down the Euler-Lagrange equations (A.13) in more explicit form:

$$\begin{aligned} & \sum_{q=1}^{N_B} w_q^k \left((\phi_k^q, v^{k,j})_{\mathbf{L}_2(\Omega)} - (d_q^k)^j \right) \phi_k^q(\mathbf{x}) \\ & + \lambda \left(-\Delta |v^{k,j}|(\mathbf{x}) + \eta \frac{\Delta |h^{k,j}|(\mathbf{x})}{|h^{k,j}|(\mathbf{x})} v^{k,j}(\mathbf{x}) \right) = 0 \end{aligned} \quad (\text{A.14})$$

for $j = 1, 2$, $\mathbf{x} \in \mathbb{R}^2$. Recall from section 3.6.1.3 that we can interpolate between regular and covariant derivatives with the parameter η . We will use (A.14) as a starting point for our implementations where all field components are expanded in a B-spline basis. Nevertheless, the more structured abstract form (A.13) clearly reveals the relevance of a negative (semi)-definite covariant derivative and the addition of a \mathbf{L}_2 -norm in the energy minimization. To this end we note that $\mathcal{S}_k^* \Lambda_k \mathcal{S}_k$ is bounded from below (see [47], subsection 7.3) so that

$$((-\lambda (D^{\mathbf{h}^k})^* D^{\mathbf{h}^k} + \mathcal{S}_k^* \Lambda_k \mathcal{S}_k) \mathbf{v}, \mathbf{v})_{\mathbf{L}_2(\Omega)} > \mathbf{c}(\Omega) \lambda (\mathbf{v}, \mathbf{v})_{\mathbf{L}_2(\Omega)}$$

and thereby the operator $-\lambda (D^{\mathbf{h}^k})^* D^{\mathbf{h}^k} + \alpha I + \mathcal{S}_k^* \Lambda_k \mathcal{S}_k$ is invertible and we can write the unique stable solution of (3.44) as

$$\mathbf{v}^k = (-\lambda (D^{\mathbf{h}^k})^* D^{\mathbf{h}^k} + \mathcal{S}_k^* \Lambda_k \mathcal{S}_k)^{-1} \mathcal{S}_k^* \Lambda_k \mathbf{d}^k. \quad (\text{A.15})$$

A.2.1 Algorithm: Solving the Euler-Lagrange Equations by Expansion in B-splines

Next we express the Euler-Lagrange equations entirely in B -spline coefficients. The computational advantages of using B -splines for variational approaches are well-known in signal in image processing, [160, 81, 62]. We will first provide a few basic properties on B -splines that we will need for our algorithm and the analysis of its stability later on.

The n -th order B -spline is given by $n - 1$ -fold convolution with B^0

$$B^n(x) = \left(B^0 *^{n-1} B^0 \right)(x) \text{ with } B^0(x) = 1_{[-\frac{1}{2}, \frac{1}{2}]}(x). \quad (\text{A.16})$$

where $f * g(x) = \int_{-\infty}^{\infty} f(y)g(x - y)dy$. Thereby the n -th order B -spline is compactly supported on $1_{[-\frac{n}{2}-\frac{1}{2}, \frac{n}{2}+\frac{1}{2}]}$. In the discrete setting we sample on a uniform integer grid, so for example if n is odd we find n non-zero-samples. Next we provide a list of Z -transforms of B -splines sampled on a uniform grid with stepsize 1:

$$\begin{aligned} ZB^2(z) &= \frac{1}{2!2^2}(z^{-1} + 3 + z) , \\ ZB^3(z) &= \frac{1}{3!}(z^{-1} + 4 + z) , \\ ZB^4(z) &= \frac{1}{3!2^3}(z^{-2} + 76z^{-1} + 230 + 76z + z^2) , \\ ZB^5(z) &= \frac{1}{5!}(z^{-2} + 26z^{-1} + 66 + 26z + z^2) , \\ ZB^6(z) &= \frac{1}{6!2^6}(z^{-3} + 722z^{-2} + 10543z^{-1} + \\ & 23548 + 10543z + 722z^2 + z^3). \end{aligned} \quad (\text{A.17})$$

The regular derivative of a B -spline of order n is expressed in B -splines of order $n - 1$

$$\frac{d}{dx}B^n(x) = B^{n-1}(x + 1/2) - B^{n-1}(x - 1/2)$$

and nicely matches the well-known a finite difference stencil. Consequently, for even order derivatives of B -splines we have

$$(B^n)^{(2k)}(x) = \sum_{l=-k}^k (-1)^l \binom{k}{|l|} B^{n-2k}(x - l) .$$

so for example for $2k = 2$ we see $(B^n)^{(2)}(x) = B^{n-2}(x + 1) - 2B^{n-2}(x) + B^{n-2}(x - 1)$, which nicely matches the finite difference $[1, -2, 1]$ -stencil for a second order derivative.

Next we express the unknown velocities $v^{k,j} : \Omega \rightarrow \mathbb{R}$, $j = 1, 2$, at time-frame $t = k\Delta t$, in periodic B -splines

$$\begin{aligned} v^{k,j}(x, y) = \\ \sum_{l=0}^{L-1} \sum_{m=0}^{M-1} c_{lm}^{kj} B^n \left(\frac{x}{a} - m \text{ Mod } \frac{M}{a} \right) B^n \left(\frac{y}{b} - l \text{ Mod } \frac{L}{b} \right) \end{aligned} \quad (\text{A.18})$$

for all $(x, y) \in \Omega = [0, M] \times [0, L]$. In our algorithms we set the resolution parameters $a = b = 1$. One can choose them differently, like in [81], as long as the n -th B-spline is properly sampled on $[0, M]$ and $[0, L]$, i.e.

$$\frac{M}{a} > n + 1 \text{ and } \frac{L}{b} > n + 1 . \quad (\text{A.19})$$

Recall that we always ensure our velocity fields to vanish at the boundaries, since we first extract the Harmonic infilling:

$$\mathbf{v}^k \mapsto \mathbf{v}^k - \left(\mathbf{v}^k \Big|_{\partial\Omega} \right)_{\mathcal{H}}$$

Recall (3.24), which allows us to use periodic B -splines. By property (A.16) and assuming (A.19) we have the following formula for the components of rank-2 tensor on \mathbb{R}^P :

$$\begin{aligned} T_{P,k}^{pp'} &:= \\ &\frac{1}{a} \int_0^P (B^n)^{(k)} \left(\frac{x}{a} - p \text{ Mod } \frac{P}{a} \right) B^n \left(\frac{x}{a} - p' \text{ Mod } \frac{P}{a} \right) dx = \\ &\frac{1}{a} \int_{-\frac{P}{2}}^{\frac{P}{2}} (B^n)^{(k)} \left(\frac{x}{a} - p \text{ Mod } \frac{P}{a} \right) B^n \left(\frac{x}{a} - p' \text{ Mod } \frac{P}{a} \right) dx = \\ &(B^{2n})^{(k)}(p - p' \text{ Mod } P) . \end{aligned}$$

with $P \in \{M, L\}$. Now after intense computations one can rewrite the energy (3.44) as

$$\begin{aligned} \mathcal{E}_{\lambda, \alpha, \mathbf{h}^k, \mathbf{d}^k}(\mathbf{v}^k, \mathbf{v}^{k-1}, \mathbf{d}^k) &= E_{\lambda, \mathbf{h}^k, \mathbf{d}^k}(\mathbf{c}^k, \mathbf{d}^k) := \\ &\sum_{j=1}^2 (\mathbf{c}^{kj}, R_{k,j}^\lambda \mathbf{c}^{kj})_{\ell_2(\{1, \dots, LM\})} + \\ &\|\Lambda_k^{1/2} (S\mathbf{c}^{k,j} - \mathbf{d}^{k,j})\|_{\ell_2(\{1, \dots, N_B\})}^2 \end{aligned} \quad (\text{A.20})$$

with

$$\begin{aligned} \mathbf{c}^k &= ((\mathbf{c}^{k,1})^T, (\mathbf{c}^{k,2})^T)^T = \\ &(c_{11}^{k,1}, c_{12}^{k,1}, \dots, c_{1M}^{k,1}, c_{21}^{k,1}, c_{22}^{k,1}, \dots, c_{2M}^{k,1}, \dots, \\ &c_{L1}^{k,1}, c_{L2}^{k,1}, \dots, c_{LM}^{k,1} ; c_{11}^{k,2}, c_{12}^{k,2}, \dots, c_{1M}^{k,2}, c_{21}^{k,2}, c_{22}^{k,2}, \dots, c_{2M}^{k,2}, \\ &\dots, \dots, c_{L1}^{k,2}, c_{L2}^{k,2}, \dots, c_{LM}^{k,2})^T \in \mathbb{R}^{2M*L} \end{aligned} \quad (\text{A.21})$$

and where the matrix representation of the covariant Laplacian expressed in the B -spline basis is given by

$$\begin{aligned} R_{k,j}^\lambda &= \lambda (-T_{L,0}(\frac{y}{b}) \otimes T_{M,2}(\frac{x}{a}) - T_{L,2}(\frac{y}{b}) \otimes T_{M,0}(\frac{x}{a})) + \\ &\lambda \sum_{x=0}^{M-1} \sum_{y=0}^{L-1} \gamma_k^j(x, y) (\tilde{T}_{L,0}(\frac{y}{b}) \otimes \tilde{T}_{M,0}(\frac{x}{a})) \end{aligned} \quad (\text{A.22})$$

where

$$(\mathbf{c}^{k,j}, R_{L,0} \otimes R_{M,0} \mathbf{c}^{k,j}) = \sum_{l,l'=0}^{L-1} \sum_{m,m'=0}^{M-1} c_{lm}^{k,j} c_{l'm'}^{k,j} (R_{L,0})_{ll'} (R_{M,0})_{mm'}$$

and $A \otimes B$ denotes the Kronecker product of matrices (related to the tensor product of the corresponding tensors) and where

$$\tilde{T}_{P,k}(u) = [(\tilde{T}_{P,k}(u))]_{pp'} = (B^n)^{(k)}(u-p)B^n(u-p')$$

with $p, p' \in \{1, \dots, P\}$ (note that we either set $P = M$ and $p = m, p = m'$ or $P = L$ and $p = l, p = l'$ in (A.22)) and where the

$$\gamma^{k,j}(x, y) = \frac{\Delta h^{k,j}(x, y)}{h^{k,j}(x, y)} = -\Delta(-\log|h^{k,j} + \delta|)(x, y) + \|\nabla \log|h^{k,j} + \delta|(x, y)\|^2,$$

is dimensionless and where $1 \gg \delta > 0$ is added to the gauge field to avoid singularities.

The mapping \mathcal{S} in (A.13) expressed in B -spline coefficients \mathbf{c}^k is given by

$$\mathcal{S}\mathbf{c}^k(q) = \sum_{j=1}^2 \mathbf{e}_j \left(\sum_{l=0}^{L-1} \sum_{m=0}^{M-1} c_{lm}^{k,j} (\phi_k^q, B^n(\frac{\cdot}{a} - m + \text{Mod}(M))) B^n(\frac{\cdot}{b} - l + \text{Mod}(L)) \right)$$

If we expand the feature vectors $\{\phi_k^q\}_{q=1}^{N_B}$ as well

$$\phi_k^q = \sum_{m'=1}^{M-1} \sum_{l'=0}^{L-1} \tilde{c}_{l'm'}^{k,q} B^n(\frac{\cdot}{a} - m' + \text{Mod}(M)) B^n(\frac{\cdot}{b} - l' + \text{Mod}(L)),$$

then we may rewrite the mapping $\mathcal{S} : \mathbb{R}^{2LM} \rightarrow \mathbb{R}^q$ as

$$\mathcal{S}\mathbf{c}^k(q) = \sum_{l,l'=0}^{L-1} \sum_{m,m'=0}^{M-1} \tilde{c}_{l'm'}^{k,q} T_{M,0}^{mm'} T_{L,0}^{ll'} c_{lm}^{kj} = (\tilde{\mathbf{c}}^{kq})^T (T_{L,0} \otimes T_{M,0}) \mathbf{c}^{kj}$$

In order to derive the minimizer of the discrete functional (A.20) which coincides with the minimizer of the continuous functional (A.13), (A.15) if we restrict ourselves to velocities \mathbf{v}^k which are within the (closed) subspace

$$\text{span}_{m=0, \dots, M-1, l=0, \dots, L-1} \left\{ B^n\left(\frac{\cdot}{a} - m + \text{Mod}(M)\right) B^n\left(\frac{\cdot}{b} - l + \text{Mod}(L)\right) \right\},$$

we simply set

$$\nabla_{\mathbf{c}^k} E_{\lambda, h^k, d^k}(\mathbf{c}^k) = \mathbf{0} ,$$

which yields (expressed in the natural matrix-representation $S \in \mathbb{R}^{N_B \times LM}$ of the isomorphic mappings $\mathbf{c}^{k1} \mapsto \mathcal{S}(\mathbf{c}^{k1}, \mathbf{0})$ and $\mathbf{c}^{k2} \mapsto \mathcal{S}(\mathbf{0}, \mathbf{c}^{k2})$)

$$(R_k^\lambda + S^T \Lambda_k S) \mathbf{c}^{k,j} = S^T \Lambda_k \mathbf{d}^{k,j} \text{ for } j = 1, 2,$$

with $\mathbf{d}^{k,j}$ given by

$$\begin{aligned} \mathbf{d}^k &:= (\mathbf{d}^{k,1}, \mathbf{d}^{k,2})^T \\ \mathbf{d}^{k,j} &:= (d_1^{k,j}, d_2^{k,j}, \dots, d_{N_B}^{k,j})^T \in \mathbb{R}^{N_B}. \end{aligned} \tag{A.23}$$

Now for $n \leq 3$ we find (akin to (A.15)) the unique solution by inversion

$$\mathbf{c}^{k,j} = (R_{k,j}^\lambda + S^T \Lambda_k S)^{-1} S^T \Lambda_k \mathbf{d}^{k,j} , \tag{A.24}$$

which we solved by a BiCSTAB algorithm (Conjugate gradient is not suitable since the matrix R_k^λ is not symmetric due to the fact that the adjoint of a covariant derivative is not equal to minus the covariant derivative, recall (A.11)). Here we have exploited the direct product structure of the terms in the matrix R_k^λ (A.22): For numerical efficiency one only needs to store the product $M \times M$ or $L \times L$ matrices such as $T_{M,0}$ and $T_{L,0}$ using the computation scheme explained in [73] in the BiCSTAB algorithm whenever a matrix product occurs.

Remark 3. *The new defined algorithm is always stable, as the real part of the smallest eigenvalues of matrix $R_{k,j}^\lambda$ is strictly positive [47, p.26]. Moreover, the algorithm commutes with translations and rotations of $n\pi/2$. In the other cases rotation invariance depends on the fluctuations of the ratio of slope and height of the graph. However, effects of not commutativity with rotation are hardly visible in practice, as shown in [47, p.28]*

Bibliography

- [1] Advanced Fertility Center of Chicago. Antral follicle counts, resting follicles, ovarian volume and ovarian reserve testing of egg supply and predicting response to ovarian stimulation drugs. URL: www.advancedfertility.com/antralfollicles.htm.
- [2] A.H. Aletras, R.S. Balaban, and H. Wen. High-resolution strain analysis of the human heart with fast-dense. *Journal of Magnetic Resonance*, 140.
- [3] H.D. Allen, D.J. Driscoll, R.E. Shaddy, and T.F. Feltes. *Heart Disease in Infants, Children, and Adolescents*. Wolters Kluwer, Lippincot, Williams and Wilkins, 2007.
- [4] S. Allender, P. Scarborough, V. Peto, and M. Rayner. European cardiovascular disease statistics 2008. Technical report, 2008.
- [5] L. Alvarez, J. Weickert, and J. Sánchez. A PDE model for computing the optical flow. In *Proc. XVI Congreso de Ecuaciones Diferenciales y Aplicaciones*, pages 1349–1356, 1999.
- [6] American Heart Association Statistics Committee and Stroke Statistics Subcommittee. Heart disease and stroke statistics 2009 update. *Circulation*, 119:480–486, 2009.
- [7] American Heart Association Statistics Committee and Stroke Statistics Subcommittee. Heart disease and stroke statistics 2010 update. Technical report, 2010.
- [8] A.A. Amini, Y. Chen, R.W. Curwen, V. Manu, and J. Sun. Coupled b-snake grides abd cibstrained thin plate splines for analysis of 2d tissue deformations from tagged MRI. *IEEE TMI*, 17:344–356, 1998.
- [9] E.D. Angelini and O. Gerard. Review of myocardial motion estimation methods from optical flow tracking on ultrasound data. *Conf Proc IEEE Eng Med Biol Soc.*, 1:1537–1540, 2006.
- [10] G.B. Arfken and H.J. Weber. *Mathematical Methods for Physicists*. Academic Press, San Diego, 1995.
- [11] T. Arts, F.W. Prinzen, T. Delhaas, J.R. Milles, A.C. Rossi, and P. Clarysse. Mapping displacement and deformation of the heart with local sine-wave modeling. *IEEE Transactions on Medical Imaging*, 29:1114–1123, 2010.

- [12] H.C. van Assen. *3D Active Shape Modeling for Cardiac MR and CT Image Segmentation*. PhD thesis, University of Leiden, Leiden, The Netherlands, 2006.
- [13] L. Axel. Physics and technology of cardiovascular MR imaging. *Cardiology Clinics*, 16(2):125–133, 1998.
- [14] L. Axel and L. Dougherty. MR imaging of motion with spatial modulation of magnetization. *Radiology*, 171(3):841–845, 1989.
- [15] L. Axel, A. Montillo, and D. Kim. Tagged magnetic resonance imaging of the heart: a survey. *Medical Image Analysis*, 9:376–393, 2005.
- [16] J. E. Axelrad, E. D. Louis, L. S. Honig, I. Flores, G. W. Ross, R. Pahwa, K. E. Lyons, P. L. Faust, and J. P. Vonsattel. Reduced purkinje cell number in essential tremor: A postmortem study. *Arch. Neurol.*
- [17] E.G. Balmashnova, L.M.J. Florack, B. Platel, F.M.W. Kanters, and B.M. ter Haar Romeny. Stability of top-points in scale space.
- [18] P. Baraldi, A. Sarti, C. Lamberti, A. Prandini, and F. Sgallari. Evaluation of differential optical flow techniques on synthesized echo images. *IEEE Transactions on Biomedical Engineering*, 43:259–272, 1996.
- [19] J. Barron. Experience with 3D optical flow on gated mri cardiac datasets. In *IEEE Computer Society. Volume Proceedings of the 1st Canadian Conference on Computer and Robot Vision*, pages 370–377, 2004.
- [20] J.L. Barron, D.J. Fleet, and S. Beauchemin. Performance of optical flow techniques. *IJCV*, 12(1):43–77, 1994.
- [21] A. Becciu, B. J. Janssen, H. C. van Assen, L. M. J Florack, V. J. Roode, and B. M. ter Haar Romeny. Extraction of cardiac motion using scale-space features points and gauged reconstruction. In *CAIP '09: Proceedings of the 13th International Conference on Computer Analysis of Images and Patterns*, Lecture Notes in Computer Science, pages 598–605, Berlin, Heidelberg, 2009. Springer-Verlag.
- [22] A. Becciu, H. C. van Assen, L. M. J Florack, S. Kozerke, V. J. Roode, and B. M. ter Haar Romeny. A multi-scale feature based optic flow method for 3d cardiac motion estimation. In *SSVM '09: Proceedings of the Second International Conference on Scale Space and Variational Methods in Computer Vision*, Lecture Notes in Computer Science, pages 588–599, Berlin, Heidelberg, 2009. Springer-Verlag.
- [23] J. Blom. *Topological and Geometrical Aspects of Image Structure*. PhD thesis, University of Utrecht, Department of Medical and Physiological Physics, 1992.

- [24] L.N. Bohs, B. Geiman, M. Anderson, S. Gebhart, and G.E. Trahey. Speckle tracking for multidimensional flow estimation. *Ultrasonics*, 38:269–375, 2000.
- [25] C. Breymann, D. Schmidt, and S.P. Hoerstrup. Umbilical cord cells as a source of cardiovascular tissue engineering. *Stem Cell Reviews and Reports*, 2:87–92, 2006.
- [26] K. Brockow, C. Christiansen, G. Kanny, O. Clement, A. Barbaud, A. Bircher, P. DeWachter, J.L. Gueant, R.M. Rodriguez Gueant, C. Mouton Faivre, J. Ring, A. Romano, J. Sainte Laudy, P. Demoly, and W.J. Pichler. Management of hypersensitivity reactions to iodinated contrast media. *Allergy*, 60:150–158, 2005.
- [27] B. Brox, A. Bruhn, N. Papenberg, and J. Weickert. High accuracy optical flow estimation based on a theory for warping. In *Proceedings of the 8th European Conference on Computer Vision*, volume 3024 of *Lecture Notes in Computer Science*, pages 25–36, 2004.
- [28] A. Bruhn, J. Weickert, T. Kohlber, and C. Schnoerr. A multigrid platform for real-time motion computation with discontinuity-preserving variational methods. *IJCV*, 70(3):257–277, 2006.
- [29] Cardiac Imaging Services. <http://www.bocaradiology.com/>.
- [30] Cardiac Specialist. <http://www.cardiacspecialists.com/>.
- [31] CardiologyRounds.com. <http://www.cardiologyrounds.com>.
- [32] N. Carranza, G. Cristóbal, P. Bayerl, and H. Neumann. Motion estimation of magnetic resonance cardiac images using the wigner-ville and hough transforms. *Optics and Spectroscopy*, 103:877–885, 2007.
- [33] Central Bureau of Statistics. <http://www.cbs.nl/en-GB/menu/themas/gezondheid-welzijn/publicaties/artikelen/archief/2009/2009-2687-wm.htm>.
- [34] M.D. Cerqueira, N.J. Weissman, V. Dilsizian, A.K. Jacobs, S. Kaul, W.K. Laskey, D.J. Pennell, J.A. Rumberger, T. Ryan, and M.S. Verani. Standardized myocardial segmentation and nomenclature for tomographic imaging of the heart: a statement for healthcare professionals from the cardiac imaging committee of the council on clinical cardiology of the american heart association. *Circulation*, 105(4):539–542, 2002.
- [35] M.Y. Chang, C.H. Chiang, T.H. Chiu, T.T. Hsieh, and Y.K. Soong. The antral follicle count predicts the outcome of pregnancy in a controlled ovarian hyperstimulation/intrauterine insemination program. *J. Assisted Reprod. Genet.*, 15:12–17, 1998.

- [36] C.C. Cheng and H.T. Li. Feature-based optical flow computation. *IJIT*, 12(7):82–90, 2006.
- [37] R. Chung, M. Zidan, and M.Y. Henein. One stop cardiac investigation "CT or echocardiography": beyond ejection fraction. *Int J Cardiovasc Imaging*, 24:327–329, 2008.
- [38] T. Constable, K. Rath, A. Sinusas, and J. Gore. Development and evaluation of tracking algorithms for cardiac wall motion analysis using phase velocity mr imaging. *Magn. Reson. Med.*, 32:33–42, 1994.
- [39] T. Corpetti, E. Memin, and P. Perez. Dense estimation of fluid flows. *PAMI*, 24(3):365–380, March 2002.
- [40] M.G. Danilouchkine, R.J. van der Geest, J.J. Westenberg, B.P. Lelieveldt, and J.H. Reiber. Influence of positional and angular variation of automatically planned short-axis stacks on quantification of left ventricular dimensions and function with cardiovascular magnetic resonance. *J Magn Reson Imaging*, 22:754–764, 2005.
- [41] G. Dassios and I.V. Lindell. Uniqueness and reconstruction for the anisotropic Helmholtz decomposition. *Journal of physics A: mathematical and general*, 35:5139–5146, 2002.
- [42] M. de Sá Rebelo, A.K.H. Aarre, K.L. Clemmesen, S.C.S. Brand, M.C. Giorgi, J.C. Meneghetti, and M.A. Gutierrez. Determination of three-dimensional left ventricle motion to analyze ventricular dyssynchrony in spect images. *EURASIP J. Adv. Signal Process*, 2010:1–9, 2010.
- [43] T.R. DeGrado, T. Turkington, J.J. Williams, C. Stearns, J.M. Hoffman, and R.E Coleman. Performance characteristics of a whole-body pet scanner. *Journal of Nuclear Medicine*, 35(1398-1406.), 1994.
- [44] S. Dhein, J. Garbade, D. Rouabah, G. Abraham, F.R. Ungemach, K. Schneider, C. Ullmann, H. Aupperle, J.F. Gummert, and F.W. Mohr. Effects of autologous bone marrow stem cell transplantation on beta-adrenoceptor density and electrical activation pattern in a rabbit model of non-ischemic heart failure. *Journal of Cardiothoracic Surgery*, 1:1–11, 2006.
- [45] J. D'hooge, B. Bijnens, J. Thoen, F. Van de Werf, G.R. Sutherland, and P. Suetens. Echocardiographic strain and strain-rate imaging: a new tool to study regional myocardial function. *IEEE Trans Med Imaging.*, 21:1022–1030, 2002.
- [46] L. Dougherty, J. Asmuth, A. Blom, L. Axel, and R. Kumar. Validation of an optical flow method for tag displacement estimation. *IEEE Transactions on Medical Imaging*, 18(4):359–363, 1999.

- [47] R. Duits, A. Becciu, B.J. Janssen, L.M.J. Florack, H.C. van Assen, and B.M. ter Haar Romeny. Cardiac motion estimation using covariant derivatives and helmholtz decomposition. Technical report, 2010.
- [48] Edwards Lifesciences. <http://www.edwards.com>.
- [49] L.E. Elsgolc. *Calculus of Variations*. Pergamon, 1961.
- [50] Expatica. <http://www.expatica.com/nl/news/dutch-news/Cancer-number-one-cause-of-death-in-Netherlands49206.html>.
- [51] F. Sheehan and D. Stewart and H. Dodge and S. Mitten and E. Bolson and and G. Brown. Variability in the measurement of regional left ventricular wall motion. *Circulation*, 68:550–559, 1983.
- [52] M.J. Faddy, R.G. Gosden, A. Gougeon, S.J. Richardsen, and J.F. Nelson. Accelerated Disappearance of Ovarian Follicles in Mid-Life: Implications for Forecasting Menopause. *Human Reproduction*, 7:1342–1346, 1992.
- [53] S.E. Fischer, G. McKinnon, S. Maier, and P. Boesiger. Improved myocardial tagging contrast. *Magnetic Resonance in Medicine*, 30(2):191–200, 1993.
- [54] L.M.J. Florack. *Image Structure*. Computational Imaging and Vision. Kluwer Academic Publishers, Dordrecht, The Netherlands, 1997.
- [55] L.M.J. Florack, B.J. Janssen, F.M.W. Kanters, and R. Duits. Towards a new paradigm for motion extraction. *Lecture Notes in Computer Science*, 4141:743–754, 2006.
- [56] L.M.J. Florack and A. Kuijper. The topological structure of scale-space images. *Journal of Mathematical Imaging and Vision*, 12(1):65–79, February 2000.
- [57] L.M.J. Florack, W. Niessen, and M. Nielsen. The intrinsic structure of optic flow incorporating measurements of duality. *IJCV*, 27(3):263–286, 1998.
- [58] L.M.J. Florack, B.M. ter Haar Romeny, J.J. Koenderink, and M.A. Viergever. Linear scale-space. *Journal of Mathematical Imaging and Vision*, 4:325–351, 1994.
- [59] L.M.J. Florack and H.C. van Assen. Dense multiscale motion extraction from cardiac cine MR tagging using HARP technology. In *ICCV workshop on MMBIA*, 2007.

- [60] L.M.J. Florack and H.C. van Assen. A new methodology for multiscale myocardial deformation and strain analysis based on tagging mri. *International Journal of Biomedical Imaging*, 2010, 2010.
- [61] Health United States (2008) National Center for Health Statistics. <http://www.ncbi.nlm.nih.gov/bookshelf/br.fcgi?book=healthus08>.
- [62] P.E. Forssen. *Low and Medium Level Vision using Channel Representations*. PhD thesis, Linkoping University, Dept. EE, Linkoping, Sweden, March 2004.
- [63] G. Fu, S.A. Hojjat, and A.C.F. Colchester. Detection of objects by integrating watersheds and critical point analysis. In *MICCAI (2)*, pages 109–116, 2003.
- [64] D. Gabor. Theory of communication. *J. IEE*, 93(26):429–457, 1946.
- [65] T.H. Gabor. *Fundamentals of Computerized Tomography*. Springer, 2010.
- [66] T. Georgiev. Relighting, retinex theory, and perceived gradients. In *Proceedings of Mirage 2005, INRIA Rocquencourt*, 2005.
- [67] M.A. Goodale and A.D. Milner. Separate visual pathways for perception and action. *Trends in neurosciences*, 15(1):20–25, 1992.
- [68] S. Gupta, E.N. Gupta, and J.L. Prince. On variable brightness optical flow for tagged MRI. In *Information Processing in Medical Imaging*, pages 323–334, 1995.
- [69] S. Gupta, E.N. Gupta, and J.L. Prince. Stochastic models for div-curl optical flow methods. *IEEE Signal Processing Letters*, 3:32–35, 1996.
- [70] M.A. Gutierrez, M.S. Rebelo, S.S. Furuie, and J.C. Meneghetti. Automatic quantification of three-dimensional kinetic energy in gated myocardial perfusion single-photon-emission computerized tomography improved by a multiresolution technique. *J. Electronic Imaging*, 12(1):118–124, 2003.
- [71] E. Haber, D.N. Metaxas, and L. Axel. Motion analysis of the right ventricle from mri images. In *Lecture Notes in Computer Science*, 1998.
- [72] K. Habuka and Y. Shinagawa. Image interpolation using enhanced multiresolution critical-point filters. *Int. J. Comput. Vision*, 58(1):19–35, 2004.
- [73] P.C. Hansen, J.G. Nagy, and D.P. O’Leary. *Deblurring Images: Matrices, Spectra, and Filtering*. SIAM, 1 edition, 2006.

- [74] C. Harris and M. Stephens. A combined corner and edge detector. In *Proc. Fourth Alvey Vision Conference*, pages 147–151, 1988.
- [75] D.J. Heeger. Optic flow using spatiotemporal filters. *IJCV*, 1(4):279–302, 1988.
- [76] B. K. P. Horn and B. G. Shunck. Determining optical flow. *AI*, 17:185–203, 1981.
- [77] <http://www.diagnosticimaging.com>.
<http://www.diagnosticimaging.com/imaging-trends-advances/cardiovascular-imaging/content/article/113619/1623411>.
- [78] Z. Hua, D. Metaxas, and L. Axel. In vivo strain and stress estimation of the heart left and right ventricles from MRI images. *Medical Image Analysis*, 7:435–444, 2003.
- [79] T. Iijima. Basic theory on normalization of a pattern (in case of typical one-dimensional pattern). *Bulletin of Electrical Laboratory*, 26:368–388, 1962. (in Japanese).
- [80] [impactscan.org](http://www.impactscan.org). <http://www.impactscan.org>.
- [81] B.J. Janssen. *Representation and Manipulation of Images Based on Linear Functionals*. PhD thesis, Eindhoven University of Technology, Eindhoven, The Netherlands, 2009. URL: <http://alexandria.tue.nl/extra2/200911295.pdf>.
- [82] B.J. Janssen and R. Duits. Linear image reconstruction by sobolev norms on the bounded domain. *Int. J. Comput. Vision*, 84(2):205–219, 2009.
- [83] B.J. Janssen, R. Duits, and L.M.J. Florack. Coarse-to-fine image reconstruction based on weighted differential features and background gauge fields. *Lecture Notes in Computer Science*, 5567:377–388, 2009.
- [84] B.J. Janssen, L.M.J. Florack, R. Duits, and B.M. ter Haar Romeny. Optic flow from multiscale dynamic anchor points attributes. *Lecture Notes in Computer Science*, 4141:767–779, 2006.
- [85] B.J. Janssen, F.M.W. Kanters, R. Duits, L.M.J. Florack, and B.M. ter Haar Romeny. A linear image reconstruction framework based on sobolev type inner products. *IJCV*, 70(3):231–240, 2006.
- [86] T.S. Denney Jr. and J.L. Prince. Reconstruction of 3-d left ventricular motion from planar tagged cardiac mr images: An estimation theoretic approach. *IEEE TMI*, 14:625–635, 1995.
- [87] J. Juergen. *Riemannian Geometry and Geometric Analysis*. Springer Verlag, 1995.

- [88] S.N. Kalitzin, J.J. Staal, B.M. ter Haar Romeny, and M.A. Viergever. A computational method for segmenting topological point sets and application to image analysis. *IEEE Transactions on Pattern Analysis and Machine Intelligence*, 23(5):447–459, 2001.
- [89] S.N. Kalitzin, B.M. ter Haar Romeny, A.H. Salden, P.F.M. Nacken, and M.A. Viergever. Topological numbers and singularities in scalar images: Scale-space evolution properties. *Journal of Mathematical Imaging and Vision*, 9:253–269, 1998.
- [90] S.N. Kalitzin, B.M. ter Haar Romeny, and M.A. Viergever. On topological deep-structure segmentation. In S.K. Mitra, editor, *Proc. 1997 IEEE Int. Conf. on Image Processing*, pages 863–866. IEEE Computer Society Press, Los Alamitos, 1997. Proceedings.
- [91] E.R. Kandel, J.H. Schwartz, and T.M. Jessell. *Principles of Neural Science*. McGraw-Hill Medical, 2000.
- [92] F. Kanters, L.M.J. Florack, R. Duits, B. Platel, and B.M. ter Haar Romeny. Scalespaceviz: α -scale spaces in practice. *Pattern Recognition and Image Analysis*, 17(1), 2007.
- [93] M. Kass, A. Witkin, and D. Terzopoulos. Snakes: Active contour models. *IJCV*, 1(4):321–331, 1988.
- [94] J.J. Koenderink. The structure of images. *Biol. Cybern.*, 50:363–370, 1984.
- [95] T. Kohlberger, E. Memin, and C. Schnoerr. Variational dense motion estimation using the helmholtz decomposition.
- [96] E.E. Konofagou, W. Manning, K. Kissinger, and S.D. Solomon. Myocardial elastography \ddot{U} comparison to results using MR cardiac tagging. *IEEE Symposium on Ultrasonics*, 1:130–133, 2003.
- [97] L. Korbo and B.B. Andersen. The distributions of purkinje cell perikaryon and nuclear volume in human and rat cerebellum with the nucleator method. *Neuroscience*, 69(1):151–158, 1995.
- [98] L. Korbo, B.B. Andersen, O. Ladefoged, and A. Moiler. Total numbers of various cell types in rat cerebellar cortex estimated using an unbiased stereological method. *Brain Research*, 609:262–268, 1993.
- [99] A. Kuijper. *The deep structure of Gaussian scale space images*. PhD thesis, University of Utrecht, 2002.
- [100] C. Lamberti, A. Sarti, and F. Bertucci. Topology of optical flow in 3d echocardiography. In *Computers in Cardiology, Lund, Sweden*, pages 227–230, 1997.

- [101] R.S. Laramee, H. Hauser, L. Zhao, and F.H. Post. Topology-based flow visualization, the state of the art. *Topology-based methods in visualization*. Berlin: Springer, pages 1–19, 2007.
- [102] P.C. Lauterbur. Image formation by induced local interactions: Examples of employing nuclear magnetic resonance. *Nature*, 242:190–191, 1973.
- [103] R.N. Lee. Two-dimensional critical point configuration graphs. *IEEE Trans. Pattern Anal. Mach. Intell.*, 6(4):442–450, 1984.
- [104] W.N. Lee, C.M. Ingrassia, S.D. Fung-Kee-Fung, K.D. Costa, J.W. Holmes, and E.E. Konofagou. Theoretical quality assessment of myocardial elastography with in vivo validation. *IEEE Trans Ultrason Ferroelectr Freq Control.*, 54:2233–2245, 2007.
- [105] M. Leitman, P. Lysyansky, S.S.V. Shir, E. Peleg, M. Binenbaum, E. Kaluski, R. Krakover, and Z. Vered. Two-dimensional strain: a novel software for real-time quantitative echocardiographic assessment of myocardial function. *Journal of the American Society of Echocardiography*, 17:1021–1030, 2004.
- [106] M. Lillholm, M. Nielsen, and L.D. Griffin. Feature-based image analysis. *IJCV*, 52(2/3):73–95, 2003.
- [107] T. Lindeberg. Scale-space for discrete signals. *PAMI*, 12(3):234–245, 1990.
- [108] T. Lindeberg. *Scale-Space Theory in Computer Vision*. The Kluwer International Series in Engineering and Computer Science. Dordrecht, The Netherlands, 1994.
- [109] J. Lotz, C. Meier, A. Leppert, and M. Galanski. Cardiovascular flow measurement with phase-contrast mr imaging: Basic facts and implementation. *RadioGraphics*, 22:651–671, 2002.
- [110] D. Lowe. Object recognition from local scale-invariant features. pages 1150–1157, 1999.
- [111] B. Lucas and T. Kanade. An iterative image registration technique with application to stereo vision. In *DARPA, Image Process*, volume 21, pages 85–117, 1981.
- [112] S. Mann and A.P. Rockwood. Computing singularities of 3d vector fields with geometric algebra. In *IEEE Visualization*, 2002.
- [113] Y. Matsumoto. *Introduction to Morse Theory*. American Mathematical Society, 2001.

- [114] E.A. McGee and A.J.W. Hsueh. Initial and Cyclic Recruitment of Ovarian Follicles. *Endocrine Reviews*, 2:200–214, 2000.
- [115] H.C. McGill, C.A. McMahan, A.W. Zieske, G.D. Sloop, J.V. Walcott, D.A. Troxclair, G.T. Malcom, R.E. Tracy, M.C. Oalman, and J.P. Strong. Associations of coronary heart disease risk factors with the intermediate lesion of atherosclerosis in youth. *Arteriosclerosis, Thrombosis, and Vascular Biology*, 20, 2000.
- [116] E. McVeigh. Regional myocardial function. *Cardiology Clinics*, 16(2):189–206, 1998.
- [117] F.G. Meyer, R.T. Constable, A.J. Sinusas, and J.S. Duncan. Tracking myocardial deformation using phase contrast mr velocity fields: A stochastic approach. *IEEE Transactions on Medical Imaging*, 15:453–465, 1996.
- [118] Motion Perception.
www.psy.ritsumei.ac.jp/~akitaoka/hvrotsnakesstrong6.jpg.
- [119] H.H. Nagel and W. Enkelmann. An investigation of smoothness constraints for the estimation of displacement vector fields from image sequences. *IEEE Trans. Pattern Anal. Mach. Intell.*, 8(5):565–593, 1986.
- [120] M. Nakahara. *Geometry, Topology and Physics, Second Edition (Graduate Student Series in Physics)*. Taylor & Francis, June 2003.
- [121] G. Nayler, N. Firmin, and D. Longmore. Blood flow imaging by cine magnetic resonance. *J. Comp. Assist. Tomog*, 10:715–722, 1986.
- [122] W. Niessen, J. Duncan, M.L.F. Nielsen, B.M. ter Haar Romeny, and M. Viergever. A multiscale approach to image sequence analysis. *Computer Vision and Image Understanding*, 65(2):259–268, 1997.
- [123] W. Niessen, J. Duncan, B.M. ter Haar Romeny, and M. Viergever. Spatiotemporal analysis of left ventricular motion. In *Medical Imaging 95, San Diego, SPIE*, pages 192–203, 1995.
- [124] T. Nir, A.M. Bruckstein, and R. Kimmel. Over-Parameterized variational optical flow. *International Journal of Computer Vision*, 76(2):205–216, February 2008.
- [125] Numerical Methods for the STEM Undergraduate. Course Notes.
- [126] N.F. Osman, W.S. McVeigh, and J.L. Prince. Cardiac motion tracking using cine harmonic phase (harp) magnetic resonance imaging. *Magnetic Resonance in Medicine*, 42(6):1048–1060, 1999.

- [127] L. Pan, J. Prince, J. Lima, and N.O. Arts. Fast tracking of cardiac motion using 3D-HARP. *IEEE transactions on Biomedical Engineering*, 52(8):1425–1435, 2005.
- [128] N. Pelc, R. Herfkens, A. Shimakawa, and D. Enzmann. Phase contrast cine magnetic resonance imaging. *Magn. Res. Quart.*, 7:229–254, 1991.
- [129] M. Pingault and D. Pellerin. Motion estimation of transparent objects in the frequency domain. *Signal Process.*, 84(4):709–719, 2004.
- [130] B. Platel. *Exploring the deep structure of images*. PhD thesis, Eindhoven University of Technology, 2007.
- [131] B. Platel, E. Balmachnova, L.M.J. Florack, and B.M. ter Haar Romeny. Top-points as interest points for image matching. In *ECCV (1)*, volume 3951 of *Lecture Notes in Computer Science*, pages 418–429. Springer, 2006.
- [132] G.M. Pohost, R.W. Biederman, and M. Doyle. Cardiovascular magnetic resonance imaging and spectroscopy in the new millennium. *Curr Probl Cardiol.*, 25:525–620, 2000.
- [133] L. Quam and D. Heeger. <http://www.cs.brown.edu/black/images.html>.
- [134] W. Reichardt and M. Egelhaaf. Properties of individual movement detectors as derived from behavioural experiments on the visual system of the fly. *Biological Cybernetics*, 58(5):287–294, 1988.
- [135] S.J. Richardsen, V. Senikas, and J.F. Nelson. Follicular Depletion during the Menopausal Transition: Evidence for Accelerated Loss and Ultimate Exhaustion. *J. Clin. Endocrinol. Metab.*, 65:1231–1237, 1987.
- [136] W. Rosamond, K. Flegal, K. Furie, A. Go, K. Greenlund, N. Haase, S.M. Hailpern, M. Ho, V. Howard, B. Kissela, S. Kittner, D. Lloyd-Jones, M. McDermott, J. Meigs, C. Moy, G. Nichol, C. O'Donnell, V. Roger, P. Sorlie, J. Steinberger, T. Thom, M. Wilson, and Y. Hong. American heart association statistics committee and stroke statistics subcommittee: heart disease and stroke statistics 2008 update. a report from the american heart association statistics committee and stroke statistics subcommittee. *Circulation*, 117:2–122, 2008.
- [137] A.K. Rutz, S. Ryf, S. Plein, P. Boesiger, and S. Kozerke. Accelerated whole-heart 3D CSPAMM for myocardial motion quantification. *Magnetic Resonance in Medicine*, 59(4):755–763, 2008.
- [138] F. Sadlo and R. Peikert. Visualizing lagrangian coherent structured and comparison to vector field topology. In *In Topology-Based Methods in Visualization, Proceedings of the 2007 Workshop*, 2007.

- [139] S. Sampath, J. Derbyshire, E. Atalar, N. Osman, and J. Prince. Realtime imaging of two dimensional cardiac strain using a harmonic phase magnetic resonance imaging (HARP MRI) pulse sequence. *Magnetic Resonance in Medicine*, 50(1):154–163, 2003.
- [140] S. Sampath and J. Prince. Automatic 3D tracking of cardiac material markers using slice-following and harmonic-phase MRI. *Magnetic Resonance Imaging*, 25:197–2008, 2007.
- [141] Y. Shinagawa and L.T. Kunii. Unconstrained automatic image matching using multiresolutional critical-point filters. *IEEE Trans. Pattern Anal. Mach. Intell.*, 20(9):994–1010, 1998.
- [142] A. Singh. An estimation for theoretic framework for image flow computation. In *IEEE ICCV*, pages 168–177, 1990.
- [143] A. Singh. Optic flow computation: A unified perspective. In *IEEE Computer Society*, 1992.
- [144] V. Sinitsyn. Magnetic resonance imaging in coronary heart disease. *European Journal of Radiology*, 38:191–199, 2001.
- [145] O. F. Sonmez, E. Odaci, O. Bas, and S. Kaplan. Purkinje cell number decreases in the adult female rat cerebellum following exposure to 900 mhz electromagnetic field. *Brain Research*, August 2010.
- [146] J. Staal, S. Kalitzin, B.M. ter Haar Romeny, and M. Viergever. Detection of critical structures in scale space. In *Lecture Notes in Computer Science*, volume 1682, pages 105–116, 1999.
- [147] A. Suinesiaputra, L.M.J. Florack, J. Westenberg, B.M. ter Haar Romeny, J. Reiber, and B. Lelieveldt. Optic flow computation from cardiac MR tagging using a multiscale differential method a comparative study with velocity encoded MRI. In *Proceedings of MICCAI 2003, LNCS, Berlin, Springer-Verlag*, pages 483–490, 2003.
- [148] L. Surchev, T. Nazwar, G. Weisheit, and K. Schilling. Developmental increase of total cell numbers in the murine cerebellum. *The Cerebellum*, 6:315–320, 2007. 10.1080/14734220601169699.
- [149] T. Tao. Differential forms and integration. Technical report, Department of Mathematics, UCLA.
- [150] B. M. Ter Haar Romeny, B. Titulaer, S. N. Kalitzin, G. Scheffer, F. Broekmans, J. J. Staal, and E. te Velde. Computer assisted human follicle ana-lysis for fertility prospects with 3D ultrasound. In A. Kuba, M. Sámal, and A. Todd-Pokropek, editors, *Information Processing in Medical Imaging (IPMI)*, volume 1613 of *Lecture Notes in Computer Science*, pages 56 – 69, Heidelberg, 1999. Springer-Verlag.

- [151] B.M. ter Haar Romeny. *Front-End Vision and Multi- Scale Image Analysis: Multiscale Computer Vision Theory and Applications, written in Mathematica*. Computational Imaging and Vision. Kluwer Academic Publishers, Dordrecht, The Netherlands, 2003.
- [152] M.A. Termeer. *Comprehensive Visualization of Cardiac MRI Data*. PhD thesis, University of Vienna, Wien, Austria, 2009.
- [153] H. Theisel, T. Weinkauff, H.C. Hege, and H.P. Seidel. Saddle connectors – an approach to visualizing the topological skeleton of complex 3d vector fields. In *IN PROC. IEEE VISUALIZATION*, pages 225–232, 2003.
- [154] J.P. Thirion. Image matching as a diffusion process: an analogy with Maxwell’s demons. *Medical Image Analysis*, 2(3):243–260, 1998.
- [155] F. Triposkiadis, C. Harbas, G. Sitafidis, J. Skoularigis, V. Demopoulos, and G. Kelepeshis. Echocardiographic assessment of left atrial ejection force and kinetic energy in chronic heart failure. *Int J Cardiovasc Imaging*, 24:15–22, 2008.
- [156] S. Ubbink, P. Bovendeerd, T. Delhaas, T. Arts, and F. van de Vosse. Towards model-based analysis of cardiac MR tagging data: relation between left ventricular shear strain and myofiber orientation. *Medical Image Analysis*, 10:632–641, 2006.
- [157] L.G. Ungerleider and M. Mishkin. Analysis of visual behavior. *MIT Press*, pages 549–586, 1982.
- [158] Y. Unlu and S. Karapolat. Myocardial tissue tracking with two-dimensional cine displacement-encoded mr imaging: Development and initial evaluation. *Radiology*, 3:872–871, 2004.
- [159] Y. Unlu and S. Karapolat. Effects of implantation of bone marrow cells on cytokine levels in the ischemic heart tissue. an experimental study. *Journal of Cardiothoracic Surgery*, 3:1–8, 2008.
- [160] M. Unser. Splines: A perfect fit for signal and image processing. *IEEE Signal Processing Magazine*, 16(6):22–38, November 1999.
- [161] H.C. van Assen, L.M.J. Florack, F.F.J. Simonis, J.J.M. Westenberg, G.J. Strijkers, and B.M. ter Haar Romenij. Cardiac strain and rotation analysis using multi-scale optical flow. In *MICCAI workshop on Comp. Biomechanics for Medicine 5*, 2010.
- [162] H.C. van Assen, L.M.J. Florack, F.F.J. Simonis, J.J.M. Westenberg, G.J. Strijkers, and B.M. ter Haar Romenij. Towards non-invasive automatic detection of cardiac pathology by strain and rotation analysis. In *ISMRM*, 2010.

- [163] H.C. van Assen, L.M.J. Florack, A. Suinesiaputra, J.J.M. Westenberg, and B.M. ter Haar Romeny. Purely evidence based multi-scale cardiac tracking using optic flow. In *MICCAI 2007 workshop on CBM II*, pages 84–93, 2007.
- [164] P. van Dijk. Direct cardiac nmr imaging of heart wall and blood flow velocity. *Comp. Assist. Tomog.*, 8:429–436, 1984.
- [165] P.A.G. van Dorst, B.J. Janssen, L.M.J. Florack, and B.M. ter Haar Romeny. Optic flow using multi-scale anchor points. In *CAIP '09: Proceedings of the 13th International Conference on Computer Analysis of Images and Patterns*, pages 1104–1112, Berlin, Heidelberg, 2009. Springer-Verlag.
- [166] A. Vilenkin and E. P. S. Shellard. *Cosmic strings and other topological defects*. Cambridge monographs on mathematical physics. Cambridge Univ. Press, Cambridge, 2000.
- [167] H. von Helmholtz. Ueber integrale der hydrodynamischen gleichungen, welche den wirbelbewegungen entsprechen. *Crelles J.*, 55(25), 1858.
- [168] J. Weickert and C. Schnörr. A theoretical framework for convex regularizers in pde-based computation of image motion. *Int. J. Comput. Vision*, 45(3):245–264, 2001.
- [169] J. Weickert and C. Schnörr. Variational optic flow computation with a spatio-temporal smoothness constraint. *J. Math. Imaging Vis.*, 14(3):245–255, 2001.
- [170] J.A. Weickert, S. Ishikawa, and A. Imiya. On the history of Gaussian scale-space axiomatics. In *Gaussian Scale-Space Theory*, Computational Imaging and Vision Series, chapter 4, pages 45–59. Kluwer Academic Publisher, 1997.
- [171] G.L. Wenk. Neuropathologic changes in alzheimer’s disease. *J. Clin. Psychiatry*, 64(9):7–10, 2003.
- [172] E. Whitney, T. Kemper, M. Bauman, D. Rosene, and G. Blatt. Cerebellar purkinje cells are reduced in a subpopulation of autistic brains: A stereological experiment using calbindin-d28k. *The Cerebellum*, 7:406–416, 2008. 10.1007/s12311-008-0043-y.
- [173] Wolfram Research. <http://www.wolfram.com>.
- [174] G. Wollny, M. Tittgemeyer, and F. Kruggel. Segmentation of vector fields by critical point analysis: Application to brain deformation, 2002.
- [175] www.vision.middlebury.edu. <http://vision.middlebury.edu/flow/eval/>.

-
- [176] A.A. Young, L. Axel, L. Dougherty, D.K. Bogen, and C.S. Parenteau. Validation of tagging with mr imaging to estimate material deformation. *Radiology*, 188:101–108, 1993.
- [177] A.A. Young, D.L. Kraitchman, L. Dougherty, and L. Axel. Tracking and finite element analysis of stripe deformation in magnetic resonance tagging. *IEEE TMI*, 14:413–421, 1995.
- [178] J. Yuan, C. Schnoer, and G. Steidl. Simultaneous higher-order optic flow estimation and decomposition.
- [179] E.A. Zerhouni, D.M. Parish, W.J. Rogers, A. Yang, and E.P. Sapiro. Human heart: Tagging with MR imaging a method for noninvasive assessment of myocardial motion. *Radiology*, 169(1):59–63, 1988.
- [180] Y. Zhu, M. Drangove, and N.J. Pelc. Estimation of deformation gradient and strain from cine-pc velocity data. *IEEE Transactions on Medical Imaging*, 16, 1997.
- [181] H. Zimmer, A. Bruhn, J. Weickert, L. Valgaerts, A. Salgado, B. Rosenhahn, and H.P. Seidel. Complementary optic flow. In *Proceedings of Energy Minimization Methods in Computer Vision and Pattern Recognition (EMMCVPR)*, LNCS, Berlin, Springer-Verlag, volume 5681, pages 207–220, 2009.

Acknowledgements

Dank je wel. I wanted to start with the words of the country that hosted me for more than 4 years and also to prove that, besides research, I have learned some Dutch ;) .

I would like to thank the many people who helped and supported me and without whom this work would not have been possible.

I am especially grateful to my promotor Prof. Bart ter Haar Romenij for the kind welcome to his interdisciplinary group, for providing me with this very challenging and interesting research project, for his openness and his endless enthusiasm for new ideas.

I would like to thank my copromotor Dr. Hans van Assen for the freedom I had in working on this research topic, for the support I got whenever I needed and for the discussions on topics inside and outside the research world.

I am thankful to Prof. Luc Florack for having been my daily supervisor during my first year as PhD student and for the support he provided after that period.

My gratitude goes also to Dr. Remco Duits for our cooperation on the extremely challenging research topics discussed in several chapters of this thesis. I would like to thank him for the patience he showed, trying to teach me the hardcore (for me) math behind each subject. I would also like to thank him for accepting to be part of my defense committee.

I am also very grateful to Dr. Andrea Fuster for the strong cooperation we had on the project about the three dimensional winding number. I would like to thank her for the fruitful discussions about this research topic, but also for the marvelous discussions about food and recipes.

I would like to thank Dr. Bart Janssen for the nice cooperation throughout several projects... well... I should probably just say Jooooow ;)

I am also grateful to Dr. Markus van Almsick for his tips and tricks with Mathematica.

I want to express my deep gratitude to Prof. Wiro Niessen, Prof. Lucas van Vliet, Prof. Frans van de Vosse and Prof. Tammo Delhaas for accepting to be part of my defense committee.

I want to thank Roy for accepting to be my paranymph... or my bodyguard,

according to the original tradition :)

Marieke deserves also a special thanks for the funny chats we had during the last part of our PhD. This certainly helped to go through this very intense period.

I want also to mention the name and to thank the other members and former colleagues of my group: Angela, Anna, Arjen, Bart J.P., Bram, Ellen, Erik, Evguenia, Fernando, Fitsum, Frans, Justus, Laurens, Laura, Marcel, Mehrdad, Neda, Paulo, Petr, Pieter, Ralph, Sander, Thorsten, Tim, Vesna and Vivian for the beautiful time at the BMT department.

I would like to thank my friends outside Sardinia that made (and make) me feel at home wherever I have gone. Allo stesso tempo sono profondamente grato verso i miei amici in Sardegna, che mi fanno sentire come se non fossi mai partito.

Vorrei ringraziare mia madre Rosa Maria per essere stata la mia prima insegnante. Il suo ricordo rimarra' sempre con me.

Un grandissimo ringraziamento va alla mia famiglia, a mio padre Francesco, a Efisia e a mia sorella Caterina, per aver sempre creduto in me e aver supportato tutte le mie scelte e decisioni molto spesso difficili da accettare.

Melanie, leider lässt sich meine wahrhaftige Dankbarkeit mit Worten schwer ausdrücken. Trotzdem will ich es versuchen. Ich danke dir, dass du für mich immer da bist. Ich danke dir, dass du mir in den harten Perioden immer neuen Mut gibst. Ich danke dir wirklich. Ich danke dir für alles.

Curriculum Vitae

Alessandro Becciu was born on April 19th, 1976 in Cagliari, Italy.

In 2004 he received a BSc in electronic engineering from the University of Cagliari in Cagliari (Italy). The graduation thesis was entitled "Analysis of neuronal data recorded with micro-electrode arrays" and was carried out from 2003 to 2004 within the group of "Bioelectronic Signal Processing" of the Max Planck Institute for Polymer Research in Mainz (Germany) under the supervision of Prof. Christiane Thielemann and direction of Prof. Wolfgang Knoll.

From 2001 to 2002 Alessandro was an Erasmus student at the department of Electrical Engineering of the Fachhochschule "University of Applied Sciences", Frankfurt am Main (Germany). Besides the courses taken at the university, he pursued an internship at "Daenet Gesellschaft für Informationstechnologie GmbH" in Frankfurt am Main, where he designed webpages.

In 2004 he started a Master of Science (MSc) program in "Physics and Computing in Medicine and Biology" within the Imaging Sciences group of the University of Manchester in Manchester (UK). He graduated in 2005 with a thesis entitled "Analysis of hand images for biometric verification" under the supervision of Prof. Tim Cootes.

After completing his MSc, Alessandro moved to the Max Planck Institute for Biological Cybernetics in Tübingen (Germany) for an internship on brain computer interfaces.

In 2006 he moved to Eindhoven (the Netherlands) and started a PhD project in the Biomedical Image Analysis group of Eindhoven University of Technology (TU/e) under the supervision of Dr. Hans van Assen and direction of Prof. Bart ter Haar Romeny. The results of this project are described in this PhD thesis "Feature based estimation of myocardial motion from tagged MR images".

Publications

A. Becciu, R. Duits, B.J. Janssen, L.M.J. Florack, B.M. ter Haar Romenij and H.C. van Assen. Feature based optic flow estimation using covariant derivatives and Helmholtz decomposition: Application to cardiac tagged MRI sequences. To be submitted to the international journal *IEEE Transactions on Medical Imaging*.

R. Duits, B.J. Janssen, A. Becciu. A variational approach to cardiac motion estimation based on covariant derivatives and multi-scale Helmholtz decomposition. Submitted to the international journal *Quarterly of applied mathematics*.

A. Becciu, R. Duits, B.J. Janssen, L.M.J. Florack, B.M. ter Haar Romenij and H.C. van Assen. Feature based cardiac motion estimation using covariant derivatives and Helmholtz decomposition Abstract submitted to the *Third Dutch Conference on Bio-Medical Engineering*, Egmond aan Zee, The Netherlands, 2011.

R. Duits, A. Becciu, B.J. Janssen, L.M.J. Florack, H.C. Assen, B.M. van Haar Romenij. Cardiac motion estimation using covariant derivatives and Helmholtz decomposition. *CASA Report* No. 10-31, Eindhoven: Technische Universiteit Eindhoven, pp. 40 (2010).

A. Becciu, A. Fuster, M. Pottek, B.J.P. van den Heuvel, B.M. ter Haar Romenij and H.C. van Assen. 3D Winding Number: Theory and Application to Medical Imaging. Accepted for publication in the special issue *Modern Mathematics in Biomedical Imaging* of the *International Journal of Biomedical Imaging* (2010).

A. Becciu, B.J. Janssen, H.C. van Assen, L.M.J. Florack, V.J. Roode, B.M. ter Haar Romenij. Extraction of cardiac motion using scale-space features points and gauged reconstruction. *In Proceedings of the 13th International Conference, (CAIP09), Münster, Germany, September 2-4, 2009*. Lecture Notes in Computer Science, Vol. 5702, pp. 598-605. Springer Verlag.

A. Becciu, H.C. van Assen, S. Kozerke, L.M.J. Florack, V.J. Roode, B.M. ter Haar Romenij. A multi-scale feature based optic flow method for 3D cardiac motion estimation. *In Proceedings of the Second International Conference*

on Scale Space and Variational Methods in Computer Vision, (SSVM09), Voss, Norway, June 1-5, 2009. Lecture Notes in Computer Science, Vol. 5567, pp. 588-599. Springer Verlag.

A Becciu, H.C. van Assen, L.M.J. Florack, B.J. Janssen, B.M. ter Haar Romenij. Cardiac motion estimation using multi-scale feature points. *Computational Biomechanics for Medicine III : Proceedings of the (MICCAI) Workshop, New York, USA, September 10, 2008. Midas Journal, Vol. 13(229), pp. 5-14.*

A. Becciu, H.C. van Assen, L.M.J. Florack, B.J. Janssen, B.M. ter Haar Romenij. Cardiac motion estimation using multi-scale feature points. *Abstract in the Nederlandse Vereniging voor Patroonherkenning en Beeldverwerking, (Dutch Society for Pattern Recognition and Image Processing), (NVPHBV), Eindhoven, Netherlands, November 12, 2008.*

A. Becciu, H.C. van Assen, L.M.J. Florack, B.J. Janssen, B.M. ter Haar Romenij. Cardiac motion estimation using multi-scale maxima. *In Proceedings of the fourteenth annual conference of the Advanced School for Computing and Imaging (ASCI08), Netherlands, Heijen, the Netherlands June 11-13, 2008, pp. 243-249.*

A. Becciu, P.A.G. van Dorst, H.C. van Assen, L.M.J. Florack, B.M. ter Haar Romenij. Study of the multi-scale optic flow constraint equation using different orders of Taylor expansion. *Proceedings 9th International Mathematica Symposium (IMS08), Maastricht, The Netherlands, June 20-24, 2008, pp. 1-15.*